Universitá di Udine
Dipartimento Politecnico di Ingegneria e Architettura

Investigation of non ideality effects on an inductive position sensor based on eddy currents using numerical methods

Doctoral Thesis

Candidate
Aldi Hoxha

Supervisor
Prof. Ruben Specogna

Reviewers
Prof. Christophe Geuzaine
Prof. Hubert Zangl

The Coordinator of the PhD Program
Prof. David Esseni

Udine, October 2023

Cycle XXXVI

To my family....

Acknowledgements

I would like to thank all the people who contributed in the development of this work. I would like to start from my supervisor, professor Ruben Specogna, for his availability, his useful insight and the openness in discussing ideas that at a first glance seemed useless but then turned out to be useful for our project.

I extend my gratitude to professor Paweł Dłotko. During my research period abroad he gave me the possibility to join his research group. In Warsaw I found a very stimulating environment where I study the misalignments acting on the sensor. I had the opportunity to work systematically on machine learning tools, which we later integrated in our research project. Although his crazy schedule he had always a moment to dedicate to me and constructively discuss what I was doing. His suggestions and rigor greatly contributed to the development of the anomaly detection tool.

I would like to thank Mauro Passarotto, former PhD student of Ruben, for his support when I decided to start this new experience. The results on the simulation and optimization tool were already developed from Ruben and Mauro during his PhD period here in Udine. I am happy I continued to help them as far as I could and contributed in what they believed and build.

Finally, I will never thank enough all my friends and my family for their strong support during these tough years where I started to doubt about many choices I did. The good news is that I understood which were the right choices and which was the wrong one.

Summary

This research describes methods in investigating non-idealities on Inductive Position Sensors (IPSs) using numerical method casted in the Discrete Geometric Approach (DGA). These sensors are able to provide position information by means of eddy currents generated on a metallic moving object called target. The positions are retrieved by computing the induced voltages picked from two receivers placed at an operative air gap from the moving object. The usual shape of the receivers is sinusoidal so that the position can be retrieved as the inverse tangent function of the picked voltages.

Being the working principle of the sensor based on the eddy currents firstly a Magneto Quasi-Static (MQS) problem has to be solved. We provide a simulation tool based on the Boundary Integral Method (BIM) to predict the performance of the sensor in terms of linearity error. The advantage with respect to the Finite Element Method (FEM) is that the number of Degrees of Freedom (DoFs) concerns only the conductor. Indeed, the meshing of the complementary domains is avoided. Furthermore, the stiffness matrix is computed only once whereas the right hand side takes into account for the movements of the conductor body. The solution time with a FEM would be prohibitive because it has to remesh the complementary domain each time a movement of the conductor takes place. After the simulation the induced voltages on the receivers are used to compute the performance of the sensor such as *linearity error*. The results validate the methodology, showing that measured linearity errors match simulated values.

Secondly, the fact that the stiffness matrix is fully populated put a limit in the size of the problem to treat. To overcome this limit, we de-

scribe a method to compute the the mutual coupling part of the system with two conductors on the fly, thus giving the possibility to solve problems with a higher number of unknowns. Finally, to speed up the solution of the system, the Gauss-Seidel (GS) iterative techniques and the Fast Multipole Method (FMM) are applied to take into account the mutual effects between the conductors. The dissipated power computed when the FMM is applied is in agreement with the one computed analytically.

Thirdly, a novel methodology to optimize the design of a ratiometric rotary IPS fabricated in Printed Circuit Board (PCB) technology. The optimization aims at reducing the linearity error of the sensor and amplitude mismatch between the voltages on the two receiving (RX) coils. Distinct from other optimization techniques proposed in the literature, the sensor footprint and the target geometry are considered as a non-modifiable input. This is motivated by the fact that, for sensor replacement purposes, the target has to fit a predefined space. For this reason, the original optimization technique proposed in this work modifies the shape of the RX coils to reproduce theoretical coil voltages as much as possible. The optimized RX shape was obtained by means of a non-linear least-square solver. Comparisons between simulations and measurements performed on different prototypes of an absolute rotary sensor show the effectiveness of the optimization tool. The optimized sensors exhibit a linearity error below 0.1% of the Full Scale (FS) without any signal calibration or post-processing manipulation.

Then, we show that each target–receiver pair needs the adoption of a different reconstruction formula for the identification of the target position, whereas in the literature the usual inverse tangent function is applied for every possible pair. We seek the target–receiver pair that maximizes the amplitude of the induced voltages on the receivers. The results show that to achieve the maximum value of the induced voltages, the best choice is to have a rectangular target and rectangular receivers. To verify these facts, a simulation and optimization method has been applied to the rectangular receiver coils on two rotary IPS realized with PCB technology. Measurements performed on the prototypes have shown an increment of the induced voltage of more than 57% with respect to the commonly used sinusoidal receivers. However, a linearity error of 1.5%FS is obtained by using the inverse tangent reconstruction formula. When using the proper formula for the rectangular receivers, the linearity error becomes 0.6%FS for the nonoptimized prototype and below 0.15%FS for the optimized one.

Moreover, a surrogate model for a rotary IPS is developed that mimics simulator behaviour and serves as a decision support tool. This model takes geometric parameters as input and outputs the maximum linearity error of the sensor, providing valuable insights to users in the phase of deciding which sensor to adopt for their purposes.

Finally, we develop a digital twin of the rotating shaft of a motor using as a key component a rotary IPS. Till now this type of sensor has always been used as a position sensor. In this work we show for the first time that it has the potential to provide information about not only the position but also deviations from the normal operating region. We use supervised learning techniques such as Random Forest (RF) regressor to predict rotor shaft misalignments based on induced voltages on receivers. The model determines both the directions and magnitudes of these anomalies, offering valuable insights into the shaft's condition without the necessity for physical inspection. To show the effectiveness of the integration between the physical and digital system, experiments performed on a rotating motor in different operating conditions are provided. The measurements confirm the effectiveness of this methods showing the detected misalignments and the accuracy of the model.

List of publications

Journals

1. Hoxha, A., Passarotto, M., Qama, G., & Specogna, R. (2022). Design optimization of PCB-Based rotary-inductive position sensors. *Sensors*, 22(13), 4683.
2. Hoxha, A., & Specogna, R. (2022). Study and Design of Ratiometric Inductive Position Sensors Using Area-of-Overlap Functions. *IEEE Sensors Journal*, 22(23), 22487-22494.
3. Hoxha, A., Passarotto, M., & Specogna, R. (2022). Fast computation of eddy currents for multiple conductors. *IEEE Transactions on Magnetics*, 58(9), 1-4.

International Conferences

1. Hoxha, A., Passarotto, M., & Specogna, R. (2022, October). Simulation and measurements of a rotary inductive position sensor. In *2022 IEEE 20th Biennial Conference on Electromagnetic Field Computation (CEFC)* (pp. 1-2). IEEE.

List of Abbreviations

A	
AI	Artificial Intelligence. 3
B	
BIM	Boundary Integral Method. 14, III
C	
CPS	Cyber-Physical Systems. 1
D	
DGA	Discrete Geometric Approach. 17, 26, 34, 36–38, III
DoFs	Degrees of Freedom. 33–36, 38, 42–44, III, XV
DSS	Decision Support System. 5, 6, 15, 79
F	
FEM	Finite Element Method. 13, 34–36, 50, 55, 70, III
FFT	Fast Fourier Transform. 95, 97
FIT	Finite Integration Technique. 26
FMM	Fast Multipole Method. 39, 41, 43–45, IV, XIX
FS	Full Scale. 50–52, 55, 56, 59, 60, 62, 64, 69, 74, 75, IV

G	
GDP	Gross domestic product. 2
GP	Gaussian Process. 82
	. 81, 82
GS	Gauss-Seidel. 41, IV
I	
Industry 4.0	Forth Industrial Revolution. 1–3, 6, 13, XV
IoE	Internet of Everything. 1
IoT	Internet of Things. 2–4
IPS	Inductive Position Sensor. 3, 7–9, 11, 13–15, 17, 21, 45, 47, 50–52, 55, 59, 63, 64, 66, 68, 69, 71, 76, 78, IV, V, XIV–XVII, XIX
	. 7–9, 11, 12, 53, 70, 79, 85, III, XV
L	
LVDT	Linear Variable Displacement Transformers. 7
M	
MQS	Magneto Quasi-Static. 17–19, 29, 40, 41, 47, III, XIII, XIV
N	
NLLS	Non-Linear Least-Square. 50, 52, 56, 71, 72, XVII
P	
PCB	Printed Circuit Board. 8, IV
R	
RBF	Radial Basis Function. 82, 83
RF	Random Forest. 85, 89, 91, 93, 95–97, 101, XVIII, XIX
RMSE	Root Mean Square Error. 83
RVDT	Rotary Variable Displacement Transformers. 7

Contents

List of Figures

List of Tables

CHAPTER 1

Introduction

Each Industrial Revolution brings new technology, and here we will focus on the Fourth Industrial Revolution, examining the role of sensors and how they can help the industry to progress and become smarter.

1.1 Fourth Industrial Revolution

The Forth Industrial Revolution (Industry 4.0) is the response to face with the consumerism, to provide high quality products for different applications in extremely short time and low cost [115], to change the way a factory is managed requiring to the employees to adapt their skills to new ones [65]. In the context of Industry 4.0, several emerging technologies are driving this behavior. These technologies include Cyber-Physical Systems (CPS), the Internet of Everything (IoE), cloud computing decentralization [121], Augmented Reality, and Big Data Analysis, among others. They are expected to enable factories to self-organize and self-control in a distributed and real-time manner [9].

Today, the implementation of these technologies is advancing the vision of the next generation of Industry 4.0. This vision revolves around the concept of smart reconfigurable manufacturing machines, with the primary goal being distributed and decentralized machine control and machine intelligence [70].

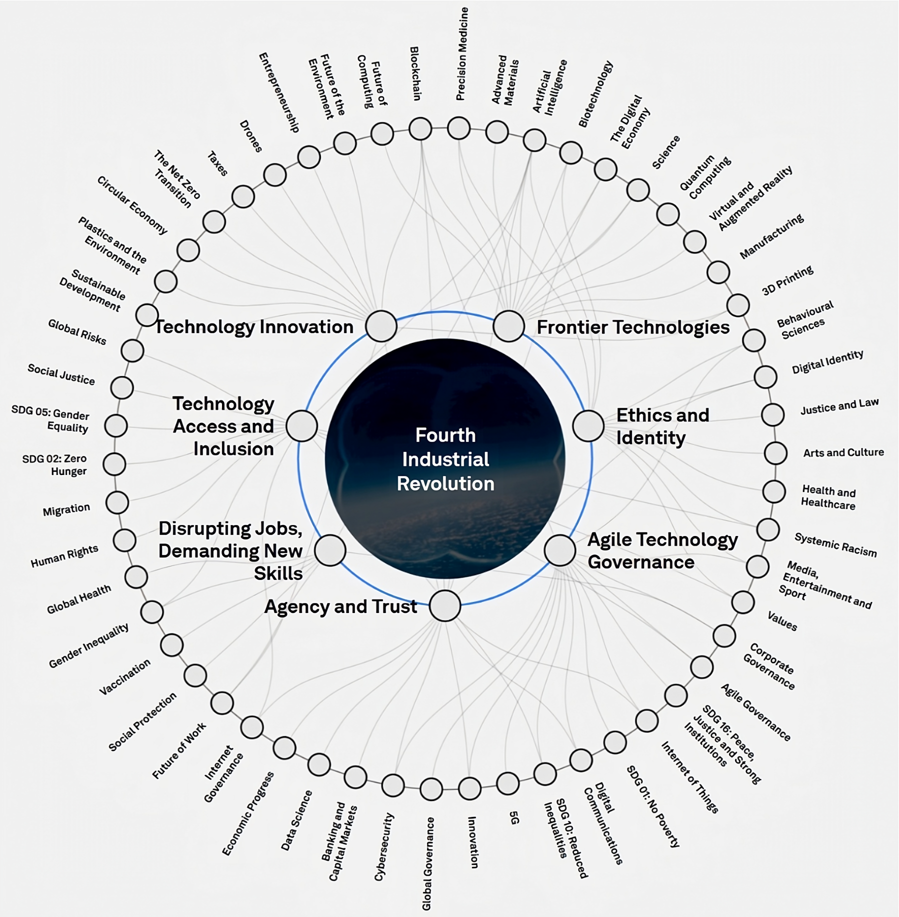

Figure 1.1: *Areas associated with the Industry 4.0 paradigm. (Source: World Economic Forum site)*

In manufacturing the adoption of this paradigm is a top priority in both private and public sectors. It is causing significant disruptions in value chains, industries, and business models. Factories are at the heart of this ongoing revolution, as one-third of the total economic value of the Internet of Things (IoT) is attributed to production. While manufacturing represents 16% of global Gross domestic product (GDP), manufacturing industries account for 64% of global Research and Development (R&D) spending [63].

Fig. 1.1 shows all the areas where the Industry 4.0 is already linked with. It can be seen that interestingly the impact is relevant also in social areas where the connection with the technology is indirectly related, i.e. Ethics and Identity, Disrupting Jobs, Demanding New Skills. The emphasis here is not only to implement a technology but, perhaps more importantly, how to exploit it in order to increase productivity, simplify the decisional steps and increase the efficiency of a company [92].

An HFS report of 2022 Excerpt for Accenture touches different aspects of the Industry 4.0 but the most salient and interesting part to the author are the *Key takeaways*. In particular:

1 AI rise: Applications of Artificial Intelligence (AI) are on the rise in use cases like *condition monitoring* and *predictive maintenance*. Industry 4.0 uses realtime data analysis, AI, and machine learning in the manufacturing process, helping reduce errors. With the convergence of AI and emerging technologies, firms can solve complex problems and smooth *decision making* by reducing human bias.

2 Digital twin, simulation, threads: *Digital twins* and *simulations* bridge the gap between physical and digital assets. Simulation can help us to execute different scenarios to test performance. By leveraging digital twins, companies can have improved operations and improve the time-to-market.

Five words were emphasized in the previous items since they are the pillars of these manuscript. Now we are going to revisit these words when applied to a key building block and crucial part of the new industrial paradigm, namely the sensors. We will start discussing the role of the sensors in this paradigm, the importance of the *simulations* and *optimization* tools, passing through *decision making systems* in support to the employees for rational choices and, at the end, discussing the word *digital twin*. Finally, the rest of the introduction will be dedicated to the core of this thesis which are the IPS. Their working principle, the advantages and disadvantages and their flexibility.

1.1.1 Industry 4.0 and the role of sensors

Sensors play a crucial role in driving Industry 4.0 and the IoT in factories and workplaces. When deployed at scale, the synergy between advanced sensors and increased computational power empowers new data analysis techniques and provides actionable insights to enhance various operational areas.

In Industry 4.0, sensors serve as critical and strategic nodes through which a wealth of information flows. Consequently, all the data generated must be interpreted to derive insights about the components where the sensors are deployed. This data interpretation requires statistical skills and machine learning tools, which can uncover hidden patterns and relationships. This trend is made possible by the overall increase in computing capabilities and the availability of statistical tools like R and Python, along with their machine learning and deep learning libraries.

Cutting-edge communications, cost-effective sensors, and powerful computing resources are creating new opportunities for collecting, evaluating, and integrating an ever-expanding range of data from industrial plants. This, in turn, leads to improved efficiency, optimized maintenance, and reduced energy costs. These factors have given rise to the concept of *smart sensors*, which not only produce signals but also provide insights into the environmental conditions in which they are deployed. This simplifies predictive maintenance, supports building automation, enables asset monitoring, and enhances overall process automation.

The trend indicates that the global smart sensors market is poised for substantial growth. This growth is driven by several key factors, such as the increasing demand for smart sensors in IoT-based devices and consumer electronics, the high demand from automobile manufacturers seeking to enhance safety and comfort, and the accelerated adoption of wireless technology for monitoring and controlling security devices within manufacturing processes, all of which incorporate smart sensors [96].

1.1.2 The role of the simulation and optimization tools

Simulation plays an important role in the manufacturing industry by significantly enhancing productivity, reducing time-to-market, improving cost-efficiency, and enhancing product appeal, while also ensuring better control and streamlining of processes. There are different type of simulators, at a system level and at physical level.

SImulations at a system level are essential component of Industry 4.0, as comprehensively detailed in [37]. Prominent companies like General Electric (GE) and Siemens have already integrated simulation strategies into their operations, exemplified by initiatives like the *brilliant factory* and *digital factory*, respectively. Siemens employs simulation tools for system planning, operation, and maintenance, while GE utilizes simulation for asset management and optimization. Additionally, simulation are employed for monitoring and optimizing production processes.

Leading providers of simulation software, such as AnyLogic, MathWorks, Siemens, Arena, Dassault Systèmes, Autodesk, Flexin, Simul8, Aspen Technology, AVEVA, and Simio, are actively investing in the development of commercial solutions.

Conversely, at a physical level, simulation tools can provide insights into the performance of individual components, which are fundamental building blocks of the bigger system. Examples of commercial solvers used for fluid dynamics, electromagnetism, and mechanics problems are COMSOL, Ansys, CST Studio.

Simulation at a physical level enables engineers to predict how the design of an Radio Frequency system or of a mechanical part will behave in millions of real-world scenarios, while reducing or even eliminating the need for costly physical testing. It's the ultimate superpower that empowers companies to innovate and drive human advancement. A comprehensive understanding of of the behaviour of the components by means of simulations offers the advantage of facilitating effective design, reducing time-to-market, and minimizing the risk of unwanted failures.

Last but not least, when the number of parameters increase, for instance geometrical parameters, the relations between those parameters and the performances are not obvious any more. The choice of the device which has the better performance starts to be very hard. There is plenty of examples of why the *optimization* is mandatory in today's life but i would rather cite an example picked from [12]. Therein one can find an instructive description of the optimization performed by [30,31] in order to improve the directivity of the Yagi-Uda antenna. Indeed, by perturbing the distances between the 6 passive elements or their length the parameter directivity is improved even of 77% with respect to the half-wave dipole. Local techniques, similar to the already cited, are related to the gradient descend and they have the advantage of being very fast but reaching local minima. On the other hand, global evolutionary techniques are usually slower than the gradient descend based techniques but can find global minima of very complex functions.

1.1.3 Decision Support

In the engineering practice, it frequently occurs that designers, final or intermediate users have to roughly estimate some basic performance or specification data on the basis of input data available at the moment, which can be time-consuming. Decisions must be made, but there are many ways to make them. These alternatives require trade-offs to satisfy the limits and achieve the best value of the targets. Decisions must be precisely specified, such as how much of a particular product to produce on a specific day at a plant [27].

There is the need for tools which can facilitate decision making and provide to the operators the possibility to perform decisions based not only on the proper experience, which is somehow subjective and not always might be the best choice, also to have objective resources which can drive the customer or the client step by step in identifying a better solution to a certain problem. Design Support System (DesSS) [66, 89], originated from the Decision Support System (DSS), are adopted for the prediction and estimation of machine specification data such as machine geometry and machine design on the basis of heterogeneous input parameters. These algorithms are able to predict the features of the new possible versions of the product or a service. With the rise of the machine learning tools also the DSS has changed the way they are implemented becoming more sophisticated.

Time plays a substantial role no matter which industry you operate in and what level you work at. Since inception, all categories of DSS are intended towards simplifying things and saving time. A DSS helps a business in quickly making an effective decision by analyzing its pros and cons. The time taken in studying data and comparing the possible courses of actions is significantly reduced. The decision time cycle gets shorter, allowing businesses to act speedily in a given situation, ultimately reducing the time-to-market.

1.1.4 Digital twins

This paradigm, introduced for *product lifecycle management* in [52], has acquired more and more relevance in industrial processes [98].

The failure of a single component may affect a massive part of the production pipeline. In the Industry 4.0 context great effort has been put in the development of automatic mechanism for fault prediction [2, 123]. Indeed, having this knowledge a priori provides benefits in terms of maintenance scheduling and cost saving [82].

A speed-up to this trend has been given from the possibility to collect and process the huge amount of data generated from the sensors [83, 111]. To have a prediction about where and when the malfunction might occur a *model* of the machines subjected to faults such as engine or shaft can be generated and processed in real-time [11]. This is the idea of the digital twin paradigm; a virtual representation of the physical entities which work in synergy with other components in order to have a full control on the entire production line [98]. This concept is scalable; a digital twin can have the dimension of the Earth [13] or the dimensions of tiny objects.

The concept is easily adaptable to many areas due to its vagueness in the definition. However, research articles express some criticism [104, 109] to the definitions adopted in the past, recalling more and more the need to give the right role to the words digital and twin. To this end we will refer to [104] where the high fidelity representation of the physical is abandoned and the level of abstraction is preferred. In the author opinion only the twin of the *measurable features* give life to the digital twin. We consider a digital twin a model who provide the expected results we are looking for. It doesn't have to be a high fidelity model.

1.2 Inductive position sensors

IPSs exploit the variation of self or mutual inductance in order to determine the displacement of the object to be detected. The variable magnetic field generated by a transmitting (TX) coil is perturbed by a moving object called *target*. A set of receiving (RX) coils placed in the neighbourhood of the transmitter will experience induced voltages that depend on the target position. A signal conditioning circuit acquires these signals in order to determine the position of the target. An example of IPS based on the eddy currents is depicted in Fig. 1.3.

The induced voltages in the RX coils depend mainly on the physical property of the target. Different types of targets can be used: target made by ferromagnetic materials, by LC resonators or by conductive but not magnetic materials (i.e. ironless) [49, 88]. Having a high magnetic permeability, ferromagnetic targets increase the mutual coupling with the RX coils, providing higher output signals. Unfortunately, they are also sensitive to static or slowly varying external magnetic fields [35, 68]. Similarly, LC resonators can provide greater output signal values compared to ironless targets thanks to the higher Q factor. As a drawback, their sensitivity to temperature can lead to continuous shifts of the resonant operating frequency, thus yielding a noisy measurement. Last but not least, sensors based on ironless targets exploit eddy currents induced on a conductive target by the variable magnetic field produced by a transmitting coil. Typically, they provide weaker output signals when compared to the other sensor types mentioned above, but they are immune to stray external fields. This feature makes them very attractive for automotive and industrial applications [36].

Examples of IPSs are Linear Variable Displacement Transformers (LVDT), Rotary Variable Displacement Transformers (RVDT) and eddy current based IPS.

Among different IPS types there are some characterizing features that are worth to be mentioned. Firstly, depending on the post-processing algorithm, the measurement may be *ratiometric* or *differential*. Secondly, depending on the geometry of the RX coils, in absence of a target, the induced voltage may be zero or different from zero [49]. Typically, the LVDT or RVDT sensors perform a differential measurement, although ratiometric ones are preferred in order to solve problems related to thermal variations [10].

1.2.1 Eddy currents based IPS

Eddy currents IPS offer some advantages that makes them appealing for a wide number of applications. They are contactless position sensors, offering significant reductions in material costs and immunity to magnetic stray fields—a crucial requirement for many applications. These IPSs can be easily integrated with cost-effective PCB-based coils and simple metallic targets, providing single-chip design flexibility for rotary on-axis (end-of-shaft) and off-axis (side-shaft or through-shaft) sensors, as well as linear and arc position sensors, covering small angles up to full 360° absolute angle sensing. The design of multi-sector rotary sensors significantly improves sensor accuracy for small angular measurements or sensors with a large number of pole pairs. These devices find wide-ranging applications in various context such as:

- Automotive
- Robotics and unmanned aerial vehicles (UAVs)
- Home Appliances
- Industrial Equipment
- Medical Devices
- Small E-vehicles

Contactless position sensors offer several advantages over traditional resolvers, Hall effect sensors, and xMR sensors. Some of the most notable benefits include:

- Elimination of the need for magnets, resulting in reduced system costs.
- Support for through-shaft capabilities.
- Flexibility for motor designs.
- Immunity to stray magnetic fields.
- Full resolution available for every angle range.

On the other hand, these sensors are bulky, the design of the transmitting and receiving coils is very delicate since geometrical non-ideality negatively affects the performance of the sensor, i.e. the ability to provide the expected displacements. Ensuring consistent sensor behavior across both linear and angular variants presents a greater challenge compared to certain alternative technologies, such as distributed impedance or magnetostrictive methods. The difficulty arises from the inherent limitations in achieving precise control when winding a coil wire. Similar to capacitive position sensing elements, inductive sensors do not yield a directly usable output. To obtain the desired output, an electronic circuit is necessary to supply the sensor with an Alternate Current (AC) drive, followed by the demodulation and conditioning of the signal.

1.2.2 Types of inductive position sensors

The shape geometry of the IPS defines also the position measurements. For instance they can measure angular positions, rotary and arc IPS, or linear displacement, linear IPS.

Rotary or angular variants of IPSs offer distinct advantages over potentiometric types, primarily owing to their robustness and extended operational lifespan. In contrast, linear sensing models are generally considered less practical for measurements spanning more than approximately 500 mm. This limitation arises from the challenges associated with maintaining uniformity along the coil's length during winding, resulting in higher costs for longer measurement ranges compared to alternative sensing methods.

Comprehensive sensor designs are illustrated in Figures 1.2 and 1.2. These designs incorporate signal conditioning electronics within the sensor housing, serving the purpose of driving the transmitting coil, demodulating, amplifying, filtering, and scaling the signal. All of these functions are integrated into the Renesas/IDT chip.

These sensing elements can be designed to operate at elevated temperatures, exceeding 150°C. However, it is essential to consider that the electronics module may require separate mounting in a lower-temperature area unless it is specifically engineered for high-temperature use. When contemplating the development of high-temperature electronics, designers may explore high-temperature semiconductors like silicon carbide (SiC), gallium arsenide (GaAs), silicon on insulator (SOS), and various dielectrically isolated CMOS processes.

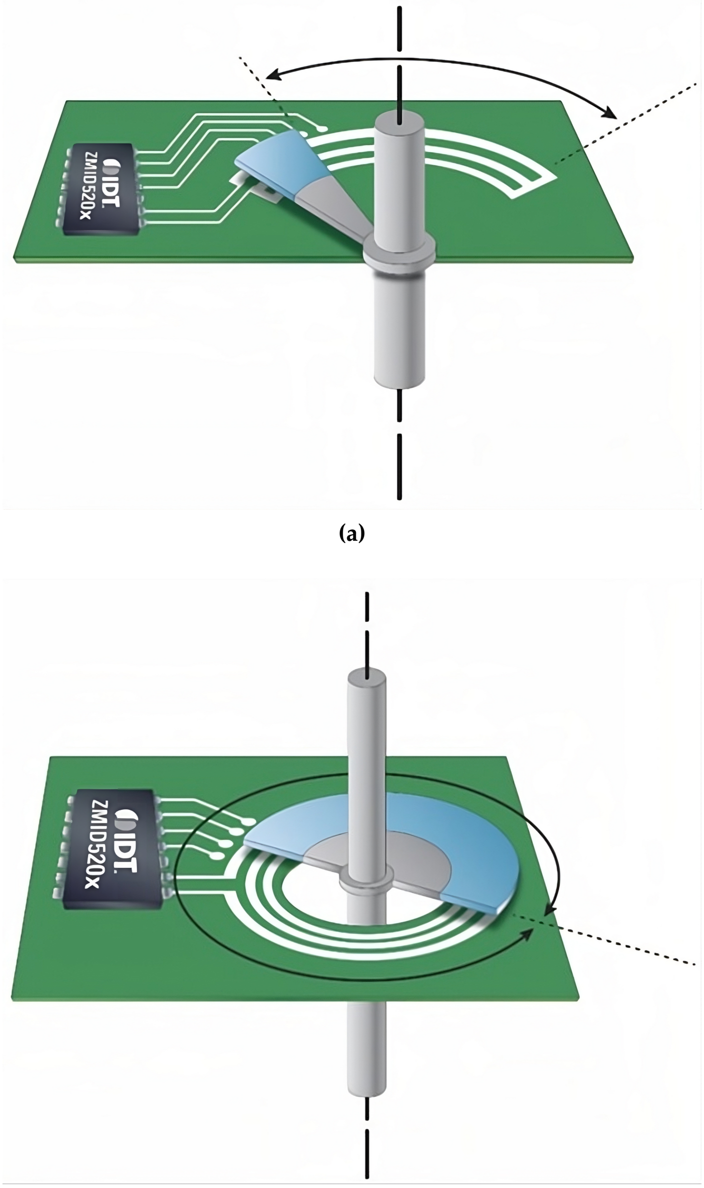

(a)

(b)

Figure 1.2

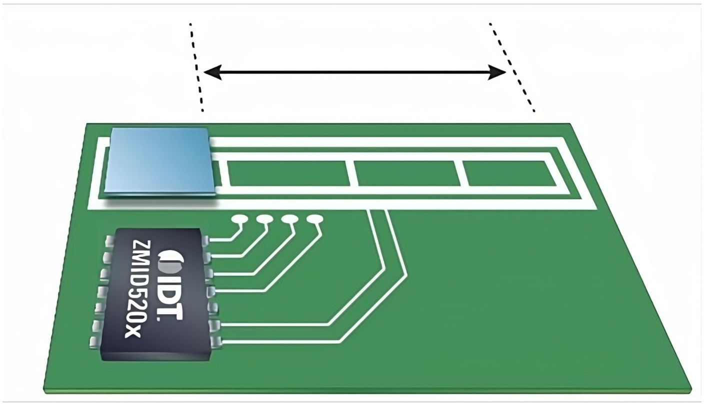

(c)

Figure 1.2: *Types of IPSs with the front-end integrated circuit which provide the induced voltages produced from the receivers. 1.2a Arc IPS; 1.2b Rotary IPS; 1.2c Linear IPS. (Pictures courtesy of IDT/Renesas)*

1.2.3 Working principle of inductive IPS

Let us consider the rotary sensor in absence of a metallic target as depicted in Figure 1.3a. It consists of a transmitter (TX) and two receivers (RX). The TX coil is driven by a known alternate current I_s, thus generating a variable magnetic field. As the Faraday–Neumann law predicts, RX coils exhibit induced voltages when operating in open circuit. Being twisted in sine and cosine shapes, the induced voltage on each receiver is zero. Indeed, by considering only one receiver, RX_{sin} for instance, the magnetic field generated by the transmitter acts on two identical areas of the coil that, however, have opposite orientations. Figure 1.3a illustrates also the numerical sequence of the current path if the RX_{sin} was short circuited.

If, instead, a conductive target is positioned above the sensor, eddy currents are generated inside it. These eddy currents create a magnetic field which opposes to the magnetic field produced by the TX coil. As a result, a shielding effect affects the portion of the domain of the sensor covered by the target. Thus, voltages induced on the RX coils depend on the target position. For instance, for the target position depicted in Figure 1.3b, the induced voltage on the receiver RX_{sin} reaches the maximum value, whereas by rotating the target by 90 degrees the induced voltage in that receiver becomes zero. This results in a cosine response that depends on the target position θ. The same working principle characterizes the receiver RX_{cos}, but being rotated in quadrature with respect to RX_{sin}, the induced voltage of RX_{cos} provides a sine spatial variation.

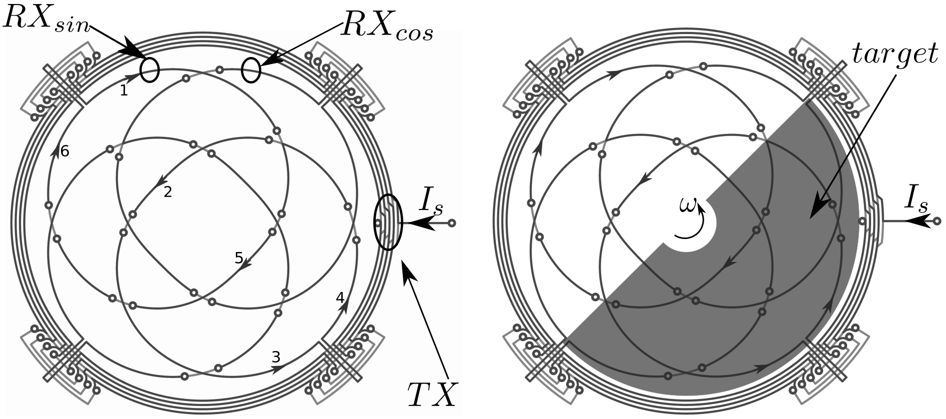

(a) *Transmitter and receiver coils geometry. The transmitter (TX) is driven by a known alternating current, whereas receivers RX_{sin} and RX_{cos} pick up the induced voltages.*

(b) *Conductive target covering a portion of the sensor; eddy currents flowing in the target perturb the system by means of their reaction magnetic field that superpose to the source field generated by TX coil.*

Figure 1.3: *The geometry of the sensor without (Figure 1.3a) and with (Figure 1.3b) the conductive target rotating with angular speed ω.*

The position of the target can be determined thanks the following formula

$$\theta^{meas} = atan\left(\frac{U_{rxsin}\left(\theta\right)}{U_{rxcos}\left(\theta\right)}\right), \tag{1.1}$$

in which θ^{meas} is the reconstructed angle, $U_{rxsin}\left(\theta\right)$ and $U_{rxcos}\left(\theta\right)$ are the sine and cosine responses of the induced voltages on the first and the second receiver, respectively.

1.2.4 Performance parameter: linearity error

In an ideal scenario, a linear position sensor should yield a set of output data that forms a straight line when exercised across its specified operating range and plotted against the input stroke. This line should seamlessly connect the zero reading to the full-scale reading. However, in real-world sensors, the data may deviate from a perfectly straight line, and the endpoints may not align precisely with the specified zero and full-scale points.

The linearity error of IPSs can be expressed as follows:

$$\epsilon_{\%} = 100 \cdot \frac{\|\boldsymbol{\theta}^{\boldsymbol{meas}} - \boldsymbol{\theta}^{\boldsymbol{id}}\|_{\infty}}{\theta_{FS}}, \tag{1.2}$$

Here, θ^{meas} and θ^{id} denote the measured and ideal angles for each target position. One should note that the definition of the straight line is arbitrary. Given the data one can obtain it as linear square fitting, best straight line, End-Point.

IPSs typically exhibit linearity errors within the range of approximately 0.2–1.0%, depending on the measuring range. This level of error is generally acceptable for many applications, particularly those where the primary concern is achieving a monotonic response with high resolution, such as in numerous position-control loops. Some sensor models may incorporate a microcontroller and nonlinearity correction, making it possible to achieve nonlinearity levels of less than 0.2% in such cases.

Although variable inductance sensors are relatively easy to fabricate, achieving high accuracy with them is a challenging endeavor. Consequently, they have found their primary use in measurement systems where simplicity takes precedence over performance. Their suitability for non-contact measurement configurations makes them particularly valuable in high-reliability applications and other scenarios where the elimination of wearing components stands as a critical sensor feature.

1.3 Inductive Position Sensors in the industry 4.0 paradigm

What we will show in this thesis is that the IPS can in fact be considered a component which fits into the Industry 4.0 paradigm. To sustain this thesis they should satisfy the conditions discussed previously.

1.3.1 Fast simulation of the IPS

The working principle of the eddy currents IPS showed that the eddy currents generated on the target shield a portion of the area where the receivers lies. During the rotation or the displacement of the target the induced voltages picked from the receivers give are used to reconstruct the position of the target. But the design of the transmitting and receiving coils is very delicate since geometrical non-ideality negatively affects the performance of the sensor, i.e. the linearity error. Is there a way to predict in advance this parameter Indeed, there is.

One approach involves using commercial solvers based on the FEM, and the following steps:

1. **Design PCB and Coils:** Start by designing the Printed Circuit Board (PCB) that includes both the receiving and transmitting coils.

2. **Design the Target:** Design a metallic target that is placed at a specific distance (air gap) from the PCB.

3. **Mesh Creation:** Create a mesh of the conductors and air in the simulation.
4. **Excitation:** Apply excitation to the transmitting coil at the frequency at which the sensor is intended to operate.
5. **Voltage Calculation:** Calculate the induced voltages on the receivers and adjust the position of the target until enough samples are obtained to accurately represent the induced voltages.

While this approach is effective, it has one drawback: it can be slow because for each movement of the target, you have to re-mesh, rebuild the sparse stiffness matrix, and solve the problem again.

An alternative approach, as we employ and discuss in chapter 2, is based on the BIM, as detailed in [18]. This method offers the advantage of not meshing the air, although it necessitates the use of a full stiffness matrix, which imposes a limit on the problem's dimension. Nevertheless, by avoiding the need to re-mesh the air, this approach significantly speeds up the simulation.

1.3.2 Optimization of the linearity error and of the received signal

Adopting a fast simulation tool, which is orders of magnitude faster than commercial software based on finite elements, provides an high level of control over the geometry of the eddy currents IPS. This enables us to adjust the dimensions of the receivers in order to enhance linearity error. This insight leads to the idea of optimizing the sensors. However, the existing literature in this area is relatively sparse. Some previous works, such as [112] and [114], have proposed sensor optimization using surrogate models to expedite simulations and global optimization techniques like Particle Swarm Optimization (PSO). Notably, both of these works involved modifying the target dimensions to optimize linearity errors.

In this manuscript, we consider the sensor's footprint and the target geometry as non-modifiable inputs. This constraint is motivated by the need for sensor replacement, where the target must fit within a predefined space. Consequently, the optimization technique we propose focuses on modifying the shape of the RX coils to align with the theoretical coil voltages as closely as possible. The optimized RX shapes are determined using a non-linear least-square solver. Through comparisons between simulations and measurements conducted on various prototypes of an absolute rotary sensor, our optimization tool demonstrates its effectiveness. The optimized sensors exhibit a linearity error below 0.1% of the full scale (FS) without requiring signal calibration or post-processing manipulation.

Additionally, it's worth noting that each target-receiver pair may require a different reconstruction formula to identify the target's position. This contrasts with the common practice in the literature, where the inverse tangent function is typically applied for all possible pairs [64, 86, 113, 116, 118, 119]. In our approach, we seek the target-receiver pair that maximizes the amplitude of the induced voltages on the receivers. This choice has two implications: increasing the area of the receiver shape should also increase the induced voltages, or equivalently, the same induced voltage can be achieved by reducing the area of the sensor. Our results demonstrate that, to attain the maximum induced voltages, the optimal choice is to have a rectangular target and rectangular receivers. These will be discussed in chapter 3.

1.3.3 Decision support

Often, users wish to determine if, within a predefined space, there exist sensor configurations with varying characteristics in terms of linearity errors. It can be very useful to have a tool that provides insights into which sensor type to consider even before conducting a full simulation. To address this need, we have developed a straightforward surrogate model for a rotary IPS that mimics the behaviour of the simulator.

The input parameters for this model are geometric variables, such as TX radius (min and max), RX radius (min and max), Target radius (min and max), while the output parameter is the maximum linearity error. By defining the level set of the linearity error as

$$S_\epsilon = \{\mathbf{x} \in \mathbb{R}^n | f(\mathbf{x}) \leq \epsilon\},$$

we can determine the bounding box of these parameters. This information are important for the operator in the decisional state and this is brick for building more sophisticated DSS.

1.3.4 Towards digital twins of the shaft

Until now, this particular sensor has predominantly served as a positional sensor. However, this manuscript introduces for the first time its capability to detect deviations from the standard operational range. Notably, the signals acquired from the IPS receivers exhibit sensitivity to shaft misalignment issues, including off-axis and tilt.

In Chapter 4, we present a machine learning tool based on the random forest algorithm to detect these misalignment. This tool takes receiver voltage data as input and delivers an output indicative of the degree of misalignment. Furthermore, it excels at predicting the specific types of deviations that manifest during the rotation of the shaft.

A fundamental question arises: Can the sensor be considered a digital twin of the shaft? To address this, we recall the definition of a digital twin provided previously. In our context, a digital twin is regarded as a reproduction of measurable quantities of interest.

Within this idea, if the sensor produces induced voltages that align with the theoretical values, it means that the shaft is perfectly centered. Any displacement from this optimal state leads to the generation of new induced voltages, which correspond to shaft anomalies. The model determines both the directions and magnitudes of these anomalies, offering valuable insights into the shaft's condition without the necessity for physical inspection. We will demonstrate the model's capability to predict both displacement directions and magnitudes, establishing the feasibility of considering the sensor as a digital twin of the shaft. Finally, we will evaluate the model's accuracy based on simulations and its real-world performance through a series of measurements.

CHAPTER 2

Solution of magneto-quasistatic problem on the target

The eddy currents generated on the target of the IPS can be effectively solved through the application of numerical methods. Specifically, the problem is casted within the MQS approximation of Maxwell's equations. This chapter will not only provide the formulation employed for the solution of the problem but also touch upon the key elements of algebraic topology behind the formulation. The latter plays a crucial role in the DGA, the numerical technique used within our research group.

2.1 The MQS problem

Figure 2.1 provides a visual representation of the problem we intend to address. We are given a time variable current loop Ω_s , a conductor Ω_c and finally the two receivers embedded in $\Omega \in \mathbb{R}^3$. The aim is to find the induced voltages on the receivers but, to achieve this, we first have to solve the eddy currents problem on the target. Once we find the distribution of the current $\boldsymbol{j}$ in Ω_c then we are ready to find the overall magnetic field acting on the receivers and finally compute the induced voltages on the receivers.

The problem we want to solve is the following: ""Find the distribu-

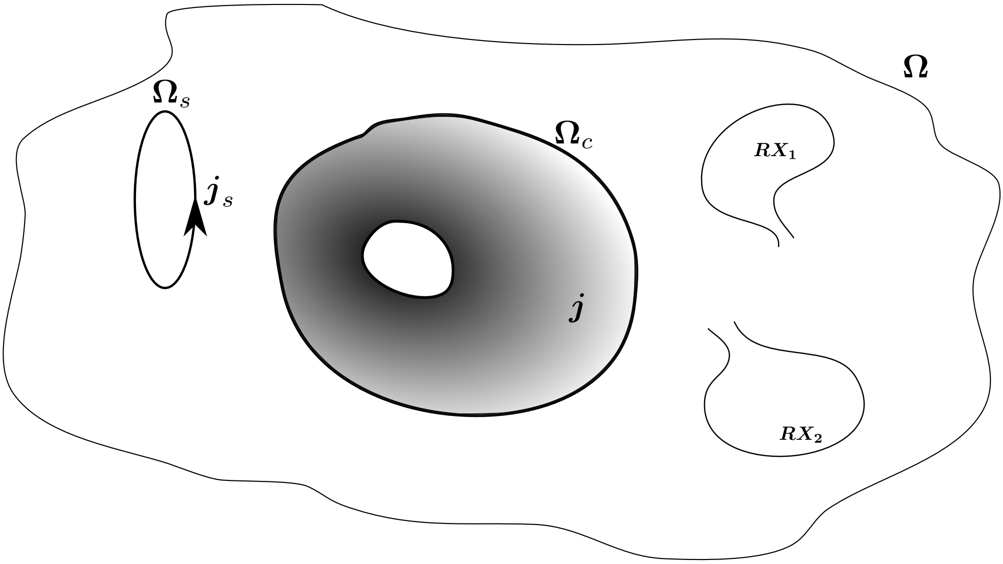

Figure 2.1: *Eddy currents problem and the related domains where* $\Omega \in \mathbb{R}^3$.

tion of the current $\boldsymbol{j}$ inside the region Ω_c given the source $\boldsymbol{j}_s$ in Ω_s". The Maxwell's equations in the aforementioned hypothesis writes either in differential or integral form as follows

$$\nabla \times \boldsymbol{e} = -\frac{\partial}{\partial t}\left(\boldsymbol{b} + \boldsymbol{b}_s\right), \quad (2.1)$$

$$\nabla \times \boldsymbol{h} = \boldsymbol{j} + \boldsymbol{j}_s, \quad (2.2)$$

$$\nabla \cdot \boldsymbol{b} = 0, \quad (2.3)$$

$$\nabla \cdot \boldsymbol{j} = 0, \quad (2.4)$$

$$\int_{\partial_f} \boldsymbol{e} \cdot d\boldsymbol{l} = -\int_f \frac{\partial}{\partial t}\left(\boldsymbol{b} + \boldsymbol{b}_s\right) \cdot d\boldsymbol{s}, \quad (2.5)$$

$$\int_{\partial_f} \boldsymbol{h} \cdot d\boldsymbol{l} = \int_f \boldsymbol{j} + \boldsymbol{j}_s \cdot d\boldsymbol{s}, \quad (2.6)$$

$$0 = \oint_f \boldsymbol{b} \cdot d\boldsymbol{s}, \quad (2.7)$$

$$0 = \oint_f \boldsymbol{j} \cdot d\boldsymbol{s}, \quad (2.8)$$

where it is possible to note the Faraday-Neumann law (2.1,2.5), the Ampere law (2.2,2.6), the Gauss law (2.3,2.7) and finally the continuity equation (2.4,2.8). Being in MQS hypothesis accumulations of charges within the considered domains are neglected so that the temporal derivative of the displacement current $\boldsymbol{d}$ doesn't take place in these equations [97].

These equations are called topological equations since they hold without the notion of distance. Whenever there is a variation of induced magnetic field there will be also an electric field and whenever there is a current there will be also a magnetic field. That's how the field are linked together but these equations alone doesn't tell us how strong the field are linked. What we need are other constraints called constitutive laws which writes

$$\boldsymbol{b} = \boldsymbol{\mu}\boldsymbol{h}, \tag{2.9}$$

$$\boldsymbol{e} = \boldsymbol{\rho}\boldsymbol{j}, \tag{2.10}$$

$$\boldsymbol{h} = \boldsymbol{\nu}\boldsymbol{b}, \tag{2.11}$$

$$\boldsymbol{j} = \boldsymbol{\sigma}\boldsymbol{e}. \tag{2.12}$$

The constitutive parameters include a wide range of low scale interactions with a single value thus simplifying the relations with global constants. The material parameters conductivity $\boldsymbol{\sigma}$, resistivity $\boldsymbol{\rho}$, reluctivity $\boldsymbol{\nu}$, permeability $\boldsymbol{\mu}$ are 3x3 tensors which constraint the value of $\boldsymbol{e}$, $\boldsymbol{j}$, $\boldsymbol{h}$ and $\boldsymbol{b}$ in the 3 dimensions of the space. The materials we consider in this thesis are isotropic and diamagnetic. The tensors can be substituted with a real positive numbers.

In the rest of this thesis we will assume $\boldsymbol{j}_s$ *harmonic* of the form

$$\boldsymbol{j}_s = Re\left\{\boldsymbol{J}_s \exp\left(j\omega t\right)\right\}. \tag{2.13}$$

so that the Maxwell's equations in the frequency domain can be written as

$$\nabla \times \boldsymbol{E} = -j\omega\left(\boldsymbol{B} + \boldsymbol{B}_s\right), \tag{2.14}$$

$$\nabla \times \boldsymbol{H} = \boldsymbol{J} + \boldsymbol{J}_s, \tag{2.15}$$

$$\nabla \cdot \boldsymbol{B} = 0. \tag{2.16}$$

In addition, the current density vector

$$\boldsymbol{J}_s \cdot \boldsymbol{n} = 0 \qquad in \qquad \partial\Omega_s \tag{2.17}$$

$$\boldsymbol{J} \cdot \boldsymbol{n} = 0 \qquad in \qquad \partial\Omega_c. \tag{2.18}$$

where $\boldsymbol{n}$ is the normal vector on boundary surface.

In real-world scenarios, apart from cases with simple geometries that allow for analytical solutions, numerical methods are employed to address complex problems. The initial step involves representing the computational domain using a set of simpler data structures called cells which are the building block of the mesh. Instead of seeking a continuous solution to the MQS problem, an approximated solution is obtained for each element of the mesh.

Various mesh element can be used, such as squares, triangles, cubes, tetrahedra, or more general polyhedra. Open-source software examples that can generate the required data structures include GMSH [48] or NETGEN [93]. The output file from such software, often referred to as a *mesh file*, provides a list of entities like nodes, volumes, and boundary faces, thus defining a partition of the computational domain into cells. These cells serve as the fundamental building blocks of the cell-complex that we will denoted as $\mathcal{K}$.

The choice of meshing strategy in computational electromagnetism is very important since the formulation adopted has to keep into account about the properties of the mesh. In the following a list of different types of meshes are listed. Each type has distinct characteristics which can be more suited for a particular application or solution of a problem.

Structured Mesh Structured meshes are characterized by a regular grid-like arrangement of elements. The most important example of structured mesh is the cubic one. One of their primary advantages lies in their computational efficiency, particularly evident in scenarios involving well-defined, uniform geometries. These meshes are comparatively straightforward to generate due to their structured nature. However, their regularity can impose limitations when adapting to complex geometries or regions with curved boundaries leading to solutions which are affected by the staircase error.

Unstructured Mesh Unstructured meshes, on the other hand, are more versatile and adaptable. This flexibility enables unstructured meshes to approximate very well also curved geometries. However, this adaptability often comes at the cost of increased computational complexity, especially in algorithms that require extensive neighbour connectivity information. Moreover, generating unstructured meshes can be a more intricate task, as the elements' shapes and sizes can vary significantly across the mesh.

Hybrid Mesh In some situations, a compromise between structured and unstructured meshes can be achieved through hybrid meshes. These meshes combine structured elements with unstructured one.

Additionally, meshes can be categorized as conformal or non-conformal, depending on how the elements of the mesh are attached together.

Conformal vs. Non-Conformal Mesh In a conformal mesh, the intersection between any two elements in the mesh is either a subelement of both, or empty. This means that the mesh is continuous and does not have any gaps or overlaps between its elements Conversely, a non-conformal mesh does not enforce this strict alignment, potentially introducing inconsistencies at interfaces.

For the purpose of simulating the target of the IPS which might contain curved shapes, for instance for arc or rotary IPS, this thesis will focus on utilizing *unstructured* and *conformal* meshes generated with GMSH.

2.2 Elements of Topology

The differential laws lack the inclusion of *global topological* insights that are deducible from the integral laws. Remedying this issue involves the utilization of (co)homology theory. The following sections are an attempt to concentrate as much as possible topics related to differential geometry and algebraic topology. The reference hereby are [41, 53, 55, 122].

Cells

Lets consider for instance a tetrahedron $T_i \in \Omega_c$ obtained from the triangulation of a manifold with boundary such as Ω_c. It is composed of 1 volume, 4 faces, 6 edges and 4 nodes. These geometrical entities in the field of algebraic topology are represented with abstract *oriented* structures called cells building the cell complex $\mathcal{K}$. For instance a volume is a 3-cell, a face is a 2-cell and more in general we will refer to p-cells where p is the spatial dimension of the cell.

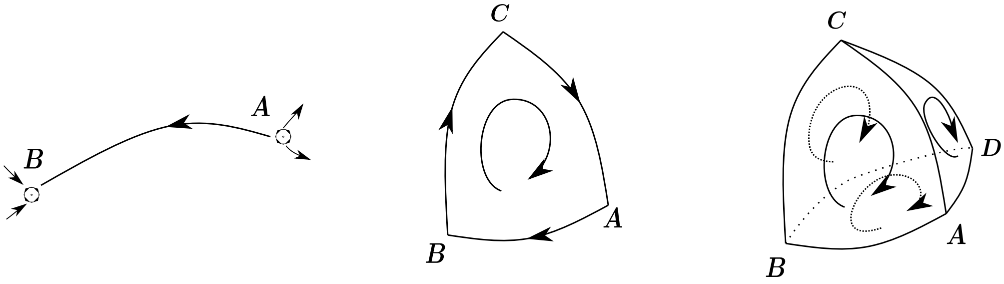

Figure 2.2: *Inner orientation of the nodes, edges, faces and volumes of a tetrahedron.*

The orientations can be easily defined. Given two nodes A and B one is called sink (B) if the field lines go inward the point otherwise are called sources (A). The line connecting the source with the sink defines the orientation of the edge. The orientation of a surface is deduced from the orientation of the edges. Finally, the orientation of the volume is deduced from the orientation of the surfaces.

What the outer orientation of a p-cell is will be clarified in the next sections, after introducing the inner oriented dual cell complex $\tilde{\mathcal{K}}$. Indeed, the outer orientation of the p-cell will be the inner orientation of the $n-p$-cell of the dual cell complex, where n is the maximum dimension of the space. In our case $n=3$ since we will be working in $\mathbb{R}^3$.

Chains

We can formally sum the p-cells (q_p) to obtain p-chains (c_p) as

$$c_p = \sum_i^{N_p} \lambda_i q_p^i \tag{2.19}$$

where N_p is the number of the p-cell with dimension p and $\lambda_i \in \mathbb{Z}$ are the coefficient depending on the orientation of the p-cell. The space of all p-chains, denoted as $C_p(\mathcal{K})$ defines an abelian group over $\mathbb{Z}$, i.e. the following properties holds

- associativity: given three chains $a, b, c \in C_p(\mathcal{K})$ and the operation $\odot$ then, $(a \odot b) \odot c = a \odot (b \odot c)$
- zero element: given $a, \theta \in C_p(\mathcal{K})$ and the operation $\odot$ then, θ is zero element if $a \odot \theta = a$. θ in this context is called null p-chain.
- inverse element: given $a, b \in C_p(\mathcal{K})$ and the operation $\odot$ then, b is the inverse element of a if their sum gives the zero element.
- commutativity: given $a, b \in C_p(\mathcal{K})$ then $a \odot b = b \odot a$,

where the operation $\odot$ is simply the $+$ operator.

Boundary Operator

An important element in algebraic topology is the boundary operator ∂_p. For instance, the boundary of a curve are the two end nodes, the boundary of surface is the closed curve, the boundary of a volume is the closed surface. In general, the boundary operator ∂_p maps chains in $C_p(\mathcal{K})$ to chains in $C_{p-1}(\mathcal{K})$.

$$\begin{tikzcd}\cdots \arrow[r] & C_{p+1}(\mathcal{K}) \arrow[r, "\partial_{p+1}"] & C_p(\mathcal{K}) \arrow[r, "\partial_p"] & C_{p-1}(\mathcal{K}) \arrow[r] & \cdots\end{tikzcd}$$

The chain complex is the sequence of chain groups connected by boundary homomorphisms.

Cycles

Definition 2.2.1. A p-cycle is a p-chain without boundary. $Z_p\left(\mathcal{K}\right)$, the set of p-cycles, is a subset of $C_p\left(\mathcal{K}\right)$ and is an abelian group.

Definition 2.2.2. A p-boundary is a p-chain boundary of a $p+1$-chain. $B_p\left(\mathcal{K}\right)$, the set of p-boundaries, is a subset of $C_p\left(\mathcal{K}\right)$ and is an abelian group.

Lemma 2.2.1 (Fundamental Lemma of Homology). The operator $\partial_p \partial_{p+1}$ maps $p+1$-chains in $C_{p+1}\left(\mathcal{K}\right)$ onto θ_p of $C_{p-1}\left(\mathcal{K}\right)$.

From the fundamental lemma of homology it follows that p-boundaries are also p-cycles but the inverse isn't true. This means that $B_p\left(\mathcal{K}\right) \subset Z_p\left(\mathcal{K}\right)$. Since the p-boundary is a p-cycle why do we have to consider them differently? The p-boundaries are boundary of an object living in a higher dimension whereas the p-cycles aren't. Finding these p-cycles allows for topological classification of our cell-complex.

Homology

Definition 2.2.3 (Homology)**.** The set of all p-cycles which are not boundary of a $p+1$-chain forms a group over the integers called homology group.

$$H_p\left(\mathcal{K}\right) = Z_p\left(\mathcal{K}\right) / B_p\left(\mathcal{K}\right)$$

Homology group is invariant under continuous transformations of the space. If two spaces are homeomorphic, meaning that there is a continuous transformation that maps one space onto the other one, then they have the same homology groups. Hence, at the end of the day, by investigating the homology group of a manifold we retrieve those global information that are lost during the differentiation process.

Finally, other useful topological invariants are the Euler-Poincaré characteristics and the Betti number. The first invariants is valid for n-dimensional polytopes and writes

$$nodes - edges + faces = 2 - 2g$$

where g is called genus of an orientable surface. This value is 0 for object homologous to a sphere, 1 if the object has one hole, 2 for a torus with empty interior.

The second topological invariant is defined as:

The p-th Betti number, denoted β_p, is equal to the dimension of $H_p\left(\mathcal{K}\right)$.

Hence β_0 tells us the number of connected components, β_1 the number of 1-cycles, β_2 the number of 2 cycles. For instance, a torus has one connected component, two 1-cycles and one 2-cycle (the hollow enclosed from the torus surface).

Cochains and de Rham map

The cochains are in duality with the chains in this sense: they are bilinear pairing of fields evaluated on chain [51]. The cochains are closely related to the notion of forms in differential geometry. While the p-forms are not restricted to be integrated over a p-chains of the mesh their discrete counterpart (cochains) are. The example presented in Tab. 2.1 shows the deep connection between cochains and chains whereas a more formal definition is possible by adopting the *de Rham map*.

Table 2.1: *Examples of Cochains*

Example	Interpretation
$\phi(\boldsymbol{r})$	Potential associated to the node elements
$\int_l \boldsymbol{e} \cdot d\boldsymbol{l}$	Voltage associated to the edges. The boundary are the two 0-cochains (potentials)
$\int_f \boldsymbol{b} \cdot d\boldsymbol{s}$	Fluxes associated to the surfaces. The boundary are the 1-cochains (voltages)
$\int_v \rho_v \, dv$	Charge associate to the volume. The boundary is the 2-cochain

The mathematical tool to produce the cochains from a field is is the *de Rham map* also mnemonically called *restriction operator* [84]. Given a p-form $\omega \in \mathcal{F}^p(\mathcal{K})$ the de Rham map $\mathcal{R}$ associate the p-cochain through the following map $\mathcal{R} : \mathcal{F}^p(\mathcal{K}) \to C^p(\mathcal{K})$

Now, a link between chains and cochains can be represented as bilinear operation which, similar to the inner product of two vector spaces, maps elements of $C_p(\mathcal{K})$ and $C^p(\mathcal{K})$ to real numbers.

$$\int : C^p(\mathcal{K}) \times C_p(\mathcal{K}) \to \mathbb{R}$$

The notation is similar to the inner product $\langle c^p, c_p \rangle$. In electromagnetism the interpretation of this bilinear pairing is that of voltages, currents, charges, or fluxes.

Remark. The operator which takes p-cochains and provide p-forms is the Whitney map defined as $\mathcal{W} : C^p(\mathcal{K}) \to \mathcal{F}^p(\mathcal{K})$ [84]. The combination of the de Rham map with the Whitney map give rise to the approximation theorem [40].

Coboundary operator

With the same formalism of the boundary operator ∂_p which acts on compact manifolds, the coboundary operator δ^p is introduced as actions on cochains.

The coboundary operator δ^p maps cochains in $C^p(\mathcal{K})$ to cochains in $C^{p+1}(\mathcal{K})$:

$$\cdots \longrightarrow C^{p-1}(\mathcal{K}) \xrightarrow{\delta^{p-1}} C^p(\mathcal{K}) \xrightarrow{\delta^p} C^p(\mathcal{K}) \longrightarrow \cdots$$

Cocycles and Coboundaries

The definitions of the cocycles and coboundaries follows again as in the case of the cycles and boundaries.

Definition 2.2.4. A p-cocycle is a p-cochain without a coboundary. The set of p-cocycles, denoted by $Z^p(\mathcal{K})$, forms a subgroup of $C^p(\mathcal{K})$ and is itself an abelian group.

Definition 2.2.5. A p-coboundary is a p-cochain, coboundary of a $(p-1)$-cochain. The set of p-coboundaries, denoted by $B^p(\mathcal{K})$, constitutes a subgroup of $C^p(\mathcal{K})$ and is also an abelian group.

As in the case of the boundary operator, the identity $\delta^p\delta^{p-1} = \theta_p$.

Cohomology

Definition 2.2.6 (Cohomology)**.** The group of p-cocycles that are not p-coboundaries forms a group over the integers, known as the cohomology group:

$$H^p(\mathcal{K}) = Z^p(\mathcal{K}) / B^p(\mathcal{K})$$

Finally we recall the Poincaré-Lefschetz duality which states that the p-th homology group is isomorphic to the $n-p$ cohomology group and viceversa, where n is the maximum dimension of the space.

$$H_p(\partial\mathcal{K}) \approx H^{n-p}(\mathcal{K}, \partial\mathcal{K})$$

To see that, lets suppose n = 3 and a manifold with a hole (for instance a torus). Firstly, a mesh is build, then the homology group turns out to have dimension 1 which means that there is a 1-cycle boundary of nothing. Equivalently, if we label each 2-cocycle, after having computed the de Rham map on those cells, the 2-cocycle bounds the 1-cycle and theorem tells us that these quantities can be put in one to one correspondence [38].

Stokes Theorem

Let $c_p \in C_p(\mathcal{K})$ be a p-chain and $\omega \in C^{p-1}(\mathcal{K})$ a p-cochain. The Stokes' theorem can be written as

$$\int_{c_p} \delta^{p-1}\omega = \int_{\partial_p c_p} \omega,$$

which can be with the new formalism assumes the form

$$\langle \delta^{p-1}c^p, c_p \rangle = \langle c^p, \partial_p c_p \rangle.$$

Stokes' theorem highlights the interplay of δ^{p-1} and ∂_p as adjoint operators.

2.2.1 More on the cells: the dual cell

The de Rham map has provided us with the opportunity to establish connections between fields and geometry, enabling the construction of cochains. However, in certain numerical schemes, some fields are not explicitly associated with any geometric element but are implicitly derived from the p-forms defined on the primal cell complex $\mathcal{K}$ by means of the constitutive relations, for instance in FEM. This raises the question of whether these fields can be explicitly attached to geometrical elements and treat them independently. This concept is at the bases of numerical scheme such as the Cell Method (CM), Finite Integration Technique (FIT) [33], and DGA [101]. Indeed, this is achievable by constructing the oriented dual cell complex $\tilde{\mathcal{K}}$.

The dual complex has the same importance of the primal cell complex. All the notion of the cells we already discussed in the previous section are preserved. We can define the chains, the cochains a homology and a cohomology on the dual complex.

The outer orientation of the p-cells of the complex $\mathcal{K}$ becomes the inner orientation for $\tilde{\mathcal{K}}$ and viceversa.

The Poincaré-Lefschetz duality for the dual cell complex writes

$$H_p\left(\partial\tilde{\mathcal{K}}\right) \approx H^{n-p}\left(\tilde{\mathcal{K}}, \partial\tilde{\mathcal{K}}\right)$$

Turns out that the homology group and the cohomology group of $\mathcal{K}$ and $\tilde{\mathcal{K}}$ are isomorphic. Indeed, the relations

$$H_p(\mathcal{K}) = H_p\left(\tilde{\mathcal{K}}\right)$$

and

$$H^p(\mathcal{K}) = H^p\left(\tilde{\mathcal{K}}\right)$$

are valid.

Hence there is a one-to-one correspondence between homology and cohomology between the of $\mathcal{K}$ and $\tilde{\mathcal{K}}$ and viceversa,

$$H^p\left(\partial\mathcal{K}\right) \approx H_{n-p}\left(\tilde{\mathcal{K}}, \partial\tilde{\mathcal{K}}\right).$$

How to build the dual complex

The concept of duality in this context is somewhat abstract because it doesn't specify the exact locations of the dual vertices beforehand. A widely used dual complex for triangulations involves utilizing the circumcenters of each simplex as dual vertices. When the initial triangulation adheres to the Delaunay criteria (meaning it satisfies the empty circumsphere property), this particular dual complex corresponds directly to the Voronoi diagram of the original vertices. It exhibits desirable properties like absence of self-intersections, convexity, and orthogonal relationships between the primal and dual components.

The barycentric dual, which employs barycenters instead of circumcenters is also frequently employed, especially in FEM. However, it doesn't consistently meet both the orthogonality and convexity conditions when applied to general triangulations [72,100].

Remark. Firstly, using the barycentric dual does not generally give dual meshes orthogonal to the primal mesh feature that is provided from the Voronoy dual. On the other hand, Voronoi dual requires an appropriate choice of the primal mesh, in order to avoid that some simplex has a circumcenter, or a spherocenter, that lie outside the simplex itself whereas the barycentric dual mesh does not involve any restriction on the primal mesh [43]

Classification of Variables

Physical variables can be classified into three distinct categories: *configuration*, *source*, and *energy* variables [102]. Every physical system, has its own "configuration", and the variables describing this configuration are called configuration variables. Each field has its sources; for example, electric charges are the source of electric fields, forces are the source of motion and deformation. Variables describing sources are called source variables. The third category, that of energy variables, is created by multiplying a configuration variable by a source variable.

Turning back at the Maxwell's equations (2.1)–(2.8) we already mentioned that they are also called topological equations. It's interesting the duality between the Faraday-Neumann law and the Ampere Law.

Indeed, the last one is constituted from the source variables whereas the former from the configuration variable. Usually, the source variables are attached to the primal cell complex whereas the configuration variable to the dual cell complex. In this way it is possible to define a consistent map from one variable of a complex to another of its dual.

Hodge Operator

The Hodge operator establishes connections between the p-cochains in $C^p(\mathcal{K})$ and the $n-p$-cochains in $C^{n-p}(\tilde{\mathcal{K}})$, incorporating material properties specific to the medium. These connections depend on the metric and involve concepts such as lengths and angles.

In the continuum, Hodge operators are linear mappings from the space of p-forms to the space of $(n-p)$-forms, where n represents the dimensionality of the space. In the context of electromagnetic theory, constitutive relations are expressed in terms of these operators: $\boldsymbol{D} = *_\epsilon \boldsymbol{E}$ and $\boldsymbol{B} = *_\mu \boldsymbol{H}$, connecting the 2-forms $\boldsymbol{D}$ and $\boldsymbol{B}$ on the primal complex with the 1-forms $\boldsymbol{E}$ and $\boldsymbol{H}$ on the dual complex.

As linear mappings, discrete versions of the Hodge operators in the lattice can be represented as a general linear mapping connecting the discrete variables as follows:

$$[*] : C^p(\mathcal{K}) \to C^{(n-p)}(\tilde{\mathcal{K}})$$

The discrete Hodge operators, denoted in what follows as $[*]$, are approximations of their continuum counterparts.

Incidence Matrices

At a discrete level, the boundary operator is described using incidence matrices. If j spans all the $p-1$-chains and i represents the p-chains, the matrix representing the boundary operator is constructed according to the rule:

$$\mathcal{M}(i,j) = \begin{cases} +1 & \text{if } c_{p-1}|_j \in \partial c_p|_i \text{ and } \operatorname{sgn}(c_{p-1}|_j) = \operatorname{sgn}(c_p|_i), \\ -1 & \text{if } c_{p-1}|_j \in \partial c_p|_i \text{ and } \operatorname{sgn}(c_{p-1}|_j) \neq \operatorname{sgn}(c_p|_i), \\ 0 & \text{if } c_{p-1}|_j \notin \partial c_p|_i. \end{cases} \tag{2.20}$$

Given the cell complex $\mathcal{K}$ in $\mathbb{R}^3$, starting from a global numbering typically assigned to its 0-cells (i.e., the grid nodes) and following the previous definition, it is possible to construct the edges-nodes, face-edges, and volume-face matrices, denoted as $\boldsymbol{G}$, $\boldsymbol{C}$, and $\boldsymbol{D}$, respectively.

These three incidence matrices completely describe the topological relations between the oriented p-cells of the cell complex.

Similarly, we define the incidence matrices of the coboundary operator, where now the index is defined as follows:

$$\mathcal{M}^{(i,j)} = \begin{cases} +1 & \text{if } \delta c^{p-1}|_j \in c^p|_i \text{ and } \mathrm{sign}(c^{p-1}|_j) = \mathrm{sign}(c^p|_i), \\ -1 & \text{if } \delta c^{p-1}|_j \in c^p|_i \text{ and } \mathrm{sign}(c^{p-1}|_j) = -\mathrm{sign}(c^p|_i), \\ 0 & \text{if } \delta c^{p-1}|_j \notin \partial c^p|_i. \end{cases} \tag{2.21}$$

These are essentially the same incidence matrices defined previously, with the particularity that the edge-node matrix has a minus sign.

2.2.2 Tonti diagram

Fig 2.3 is a general representation of all the maps involved until now, starting from $\mathcal{K}$ and $\tilde{\mathcal{K}}$ for a manifold of dimension $n = 3$. Generally we refer to this diagram as Tonti's diagram and is a pictorial but very powerful tool that describe all the concept we introduced previously. And the next paragraph's aim is to derive the MQS problem we want to solve by looking at the Tonti's diagram. The presented diagram do not take into account time element although the general version considers it.

Cochains for the MQS problem

In the eddy current problem the cochains involved in the solution of the problem are listed below.

- 2-cochain $\mathbf{I} \in C^2(\mathcal{K})$ defined as the integral of the current density vector in the primal complex:

$$\mathbf{I} = \int_f \boldsymbol{j} \cdot d\boldsymbol{s},$$

- 1-cochain $\mathbf{F} \in C^1(\mathcal{K})$ defined as the integral of the magnetic field in the primal complex:

$$\mathbf{F} = \int_l \boldsymbol{h} \cdot d\boldsymbol{l},$$

- 1-cochain $\mathbf{T} \in B^1(\mathcal{K})$ defined as the integral of the electric vector potential in the primal complex:

$$\mathbf{T} = \int_l \boldsymbol{t} \cdot d\boldsymbol{l},$$

$$\begin{tikzcd}
\mathcal{K} & c_3 \arrow[r, bend left, "\mathbf{D}^{\mathbf{T}}"] \arrow[d, bend right, "\mathcal{R}"'] & c_2 \arrow[r, bend left, "\mathbf{C}^{\mathbf{T}}"] \arrow[d, bend right, "\mathcal{R}"'] & c_1 \arrow[r, bend left, "\mathbf{G}^{\mathbf{T}}"] \arrow[d, bend right, "\mathcal{R}"'] & c_0 \arrow[d, bend right, "\mathcal{R}"'] \\
C(\mathcal{K}) & c^3 & c^2 \arrow[l, bend right, "\mathbf{D}"'] \arrow[d, bend right, "{[*]}"'] & c^1 \arrow[l, bend right, "\mathbf{C}"'] \arrow[d, bend right, "{[*]}"'] & c^0 \arrow[l, bend right, "\mathbf{G}"'] \\
C(\tilde{\mathcal{K}}) & c^0 \arrow[r, bend left, "\tilde{\mathbf{G}}"] & c^1 \arrow[r, bend left, "\tilde{\mathbf{C}}"] \arrow[u, bend right, "{[*]}^{-1}"'] & c^2 \arrow[r, bend left, "\tilde{\mathbf{D}}"] \arrow[u, bend right, "{[*]}^{-1}"'] & c^3 \\
\tilde{\mathcal{K}} & c_0 \arrow[u, bend left, "\mathcal{R}"] & c_1 \arrow[l, bend right, "\tilde{\mathbf{G}}^{\mathbf{T}}"'] \arrow[u, bend left, "\mathcal{R}"] & c_2 \arrow[l, bend right, "\tilde{\mathbf{C}}^{\mathbf{T}}"'] \arrow[u, bend left, "\mathcal{R}"] & c_3 \arrow[l, bend right, "\tilde{\mathbf{D}}^{\mathbf{T}}"'] \arrow[u, bend left, "\mathcal{R}"]
\end{tikzcd}$$

Figure 2.3: *Tonti diagram*

- 2-cochain $\tilde{\mathbf{\Phi}} \in C^2\left(\tilde{\mathcal{K}}\right)$ defined as integral of the magnetic induction field in the dual complex:

$$\tilde{\mathbf{\Phi}} = \int_{\tilde{f}} \boldsymbol{b} \cdot d\boldsymbol{s},$$

- 1-cochain $\tilde{\mathbf{U}} \in C^1\left(\tilde{\mathcal{K}}\right)$ defined as the integral of the electric vector potential in the primal complex:

$$\tilde{\mathbf{U}} = \int_{\tilde{l}} \boldsymbol{e} \cdot d\boldsymbol{l},$$

- 1-cochain $\tilde{\mathbf{A}} \in B^1\left(\tilde{\mathcal{K}}\right)$ defined as the integral of the magnetic vector potential on the dual complex:

$$\tilde{\mathbf{A}} = \int_{\tilde{l}} \boldsymbol{a} \cdot d\boldsymbol{l},$$

2.3 Discrete approach of the eddy current problem

The eddy current problem or Faraday-Neumann equations can be solved in terms of 1-cochains **T** which are also called Degrees of Freedom (DoF). To do this, we look at the Tonti's Diagram, and we see that

$$\mathbf{DI} = \boldsymbol{\theta} \quad \text{and} \quad \tilde{\mathbf{D}}\tilde{\mathbf{\Phi}} = \boldsymbol{\theta} \tag{2.22}$$

hold. That means that those quantities can be written as boundaries of 1-cochains **T** and $\tilde{\mathbf{A}}$, i.e.,

$$\mathbf{I} = \mathbf{CT} \tag{2.23}$$

and

$$\tilde{\mathbf{\Phi}} = \tilde{\mathbf{C}}\tilde{\mathbf{A}} \tag{2.24}$$

The first Faraday-Neumann law writes

$$\tilde{\mathbf{C}}\tilde{\mathbf{U}} = -j\omega(\tilde{\mathbf{\Phi}}_c + \tilde{\mathbf{\Phi}}_s) \tag{2.25}$$

Thus, we have

$$\tilde{\mathbf{C}}\tilde{\mathbf{U}} = -j\omega\tilde{\mathbf{C}}\tilde{\mathbf{A}} - j\omega\tilde{\mathbf{\Phi}}_s \tag{2.26}$$

By renaming the discrete Hodge operators $[*_\rho]$ and $[*_\mu]$ as **R** and **M**, respectively, the constitutive equations are written as

$$\tilde{\mathbf{U}} = \mathbf{RI}, \tag{2.27}$$

$$\tilde{\mathbf{A}} = \mathbf{M}\mathbf{I} \tag{2.28}$$

It's important to emphasize that the relationship between the 1-cochain magnetic vector potential $\tilde{\mathbf{A}}$ and the 2-cochain current density vector $\mathbf{I}$ is derived using the Biot-Savart law. The step-by-step procedure to determine this relationship in the k-th element of the mesh is:

1. Application of the Whitney map $\mathcal{W}$ to the 2-cochain $\mathbf{I} \in C^2(\mathcal{K})$, resulting in the recovery of the 2-form $\boldsymbol{j} \in \mathcal{F}^2(\mathcal{K})$.
2. computation fo the magnetic vector potential:

$$\boldsymbol{a}(\boldsymbol{r}) = \frac{\mu_0}{4\pi} \int_{v_k} \frac{\boldsymbol{j}(\boldsymbol{r}')}{|\boldsymbol{r} - \boldsymbol{r}'|} dv(\boldsymbol{r}'), \tag{2.29}$$

   with $\boldsymbol{r}$ the evaluation point, $v_k \subset \mathcal{K}$ the k-th volume of the discretized domain, $\boldsymbol{r}' \in v_k$ and $\boldsymbol{j}(\boldsymbol{r}')$ the current density field in $\boldsymbol{r}'$.

3. Application of the de Rham map $\mathcal{R}$ for $\boldsymbol{a}$ over the 1-chains of the dual complex, resulting in the 1-cochain $\tilde{\mathbf{A}} \in B^1(\tilde{\mathcal{K}})$.

Putting all together, we end up with the discrete version of the Faraday-Neumann law.

$$\tilde{\mathbf{C}}(\mathbf{R} + j\omega\mathbf{M})\mathbf{C}\mathbf{T} = -j\omega\tilde{\boldsymbol{\Phi}}_s \tag{2.30}$$

The only unknown is the 1-cochain $\mathbf{T}$ and the right hand side is known but further details must be added in order to make the system work.

2.3.1 Non trivial domain

The system described in (2.30) can be expressed more concisely as:

$$\mathbf{K}\mathbf{T} = \mathbf{b}_s, \tag{2.31}$$

Here, $\mathbf{K}$ represents the matrix containing $\mathbf{C}^T(\mathbf{R} + j\omega\mathbf{M})\mathbf{C}$, and $\mathbf{b}_s$ corresponds to the right-hand side term $-j\omega\mathbf{C}^T\tilde{\mathbf{A}}_s$.

However, if Ω_c is not simply connected the system (2.31) isn't sufficient to solve the problem. This system only captures local relations where a p-cochain is always a coboundary of $p-1$-cochain, i.e. it the solution lies within the set of cocycles $B^p(\mathcal{K})$, and $B^p(\mathcal{K}) = Z^p(\mathcal{K})$. But what about the p-cochains that are not coboundaries of $p-1$-cochains? In such cases, $B^p(\mathcal{K})$ is a proper subset of $Z^p(\mathcal{K})$. So, if one restricts the search for solutions to $B^p(\mathcal{K})$, it implies that the space of cocycles is not fully spanned.

Consequently, **I** has an additional component known as $\mathbf{i} \in H^2(\mathcal{K})$, representing independent currents:

$$\mathbf{I} = \mathbf{CT} + \mathbf{Hi}.$$

The current **I** still satisfies the divergence-free condition, but now there exists 2-cocycles (**i**) that are not the coboundary of any 1-cochain. Now the problem is how to efficiently find the matrix **H** which represent a basis for the 2-cocycle. A way to address this issue is to use *lazy generators* [39]. They are cocycles that span the first cohomology group $H^1\left(\tilde{\mathcal{K}}, \partial\tilde{\mathcal{K}}\right)$. They have the advantage of being much faster to compute than the standard cohomology generators, and they can be directly employed in ungauged eddy-current formulations. When applied to problems in the frequency domain, as in our case, it doesn't result in any degradation of performance during the system's solution or the computation of current density distribution. The latter remains consistent up to the linear solver's tolerance, regardless of whether we utilize the approach that leverages the lazy generators or just the independent ones.

Furthermore, opting for this choice has the advantage of very quick pre-processing, has a linear worst-case complexity, even when there are numerous generators.

$$\begin{bmatrix} \mathbf{K} & \mathbf{KH} \\ \mathbf{H}^T\mathbf{K} & \mathbf{H}^T\mathbf{KH} \end{bmatrix} \begin{bmatrix} \mathbf{T} \\ \mathbf{i} \end{bmatrix} = \begin{bmatrix} \mathbf{b}_s \\ \mathbf{H}^T\mathbf{b}_s \end{bmatrix}, \tag{2.32}$$

where **H** is a matrix storing a proper cohomology basis Ω_c, $\mathbf{b}_s$ represents the effect of the already mentioned source of magnetic field generated by Ω_s. The problem DoFs are stored in **T** and **i** that stems, respectively, from the array of the integral of the electric vector potential along the mesh edges and the additional nonlocal currents flowing in a non trivial Ω_c.

2.3.2 Basis functions

What remains unclear is the process of constructing the mass matrices **R** and **M**. To address this, it's essential to delve into the Galerkin method, commonly employed in FEM, and understand its relationship with the DGA. The crucial components in this discussion are the basis functions.

Reconstruction Operators and Their Significance

In our previous discussion, we introduced the Whitney operator:

$$\mathcal{W} : C^p(\mathcal{K}) \to \mathcal{F}^p(\mathcal{K})$$

This operator maps p-cochains to p-forms, a fundamental concept in our context. However, there exists a broader category of operators known as *reconstruction operators* that play a crucial role in finite-dimensional spaces.

In finite-dimensional spaces $\mathcal{V}$, it's common to seek special vectors $\{v_1, \cdots, v_n\}$ called *basis vectors* and represent each element of $\mathcal{V}$ as linear combination of the basis vectors. In our current context, the spaces are infinite-dimensional because we deal with functions instead of traditional vectors. Nevertheless, if we can always try to represent the solution as a linear combination of *basis functions* that generate the function space, similarly to the finite dimensional spaces. The key difference is that the functional space spanned from the basis function have to satisfy the requirements of $\mathbf{1)}$ square-integrability (possess finite energy) and $\mathbf{2)}$ possess an inner product. Such a class of functions is referred to as a pre Hilbert space, and it becomes a Hilbert space when it is complete[1].

Reconstruction operators perform the crucial task of mapping DoFs to functions residing in a finite-dimensional space. Typically, DoFs are associated with various geometric elements within an underlying three-dimensional mesh, such as vertices, edges, faces, and cells. Reconstruction operators essentially act as the right inverse of the de Rham (or reduction) operators. De Rham operators traditionally map fields (known as potentials, circulations, fluxes, and densities, or p-forms in the language of differential geometry) to DoFs attached to vertices, edges, faces, and cells, respectively. Combining a reconstruction operator with the corresponding de Rham operator results in an interpolation operator. A reconstruction operator is considered low-order when this interpolation operator leaves cell-wise constant fields unchanged.

In the FEM literature, various reconstruction operators have been developed for the tetrahedral cells. Notable examples include Whitney reconstruction functions for potentials, the lowest-order Nédélec shape functions for circulations, and the lowest-order Raviar-Thomas-Nédélec shape functions for fluxes.

The Nédélec basis functions (Eq. 2.33), which discretize the $\mathcal{H}(\text{curl})$ space, ensure tangential continuity of their approximations across element interfaces. This property makes them particularly well-suited for fields like $\boldsymbol{E}$ and $\boldsymbol{H}$, which share this constraint at material interfaces.

The Raviart-Thomas basis functions (Eq. 2.34), which discretize the $\mathcal{H}(\text{div})$ space, guarantee continuity of the normal component of their approximations across element interfaces. This characteristic makes

---

[1] Completeness implies that each Cauchy sequence is convergent

them suitable for fields such as $\boldsymbol{B}$, $\boldsymbol{J}$, and $\boldsymbol{D}$, where the normal component continuity is essential.

For example, when dealing with a tetrahedron with 4 nodes (n_a, n_b, n_c, n_d), the basis function associated with the face formed by nodes n_a, n_b, and n_c plays a significant role [100].

$$w_{e_j} = w_a^n \nabla w_b^n - w_b^n \nabla w_a^n \tag{2.33}$$

$$w_{f_j} = 2\left(w_{n_a} \nabla w_{n_b} \times \nabla w_{n_c} + w_{n_b} \nabla w_{n_c} \times \nabla w_{n_a} + w_{n_c} \nabla w_{n_a} \times \nabla w_{n_b}\right) \tag{2.34}$$

2.3.3 Mass matrices: link with the finite element method

Now we are ready to reconstruct our fields within in the volume v_k of a tetrahedron as

$$\boldsymbol{j}_k = \underline{\boldsymbol{w}_k}^T \mathbf{I}_k, \tag{2.35}$$

where $\underline{\boldsymbol{w}_k}^T$ is the vector of the basis function attached to the faces or edges of the k-th tetrahedron and $\mathbf{I}_k$ is the respective DoFs vector. The basis function $\underline{\boldsymbol{w}_k}^T$ has 3 rows and as many columns as the DoFs of the considered cell. The procedure used to solve the problem (2.30) relies on the Galerkin method.

The Galerkin method is a technique used to transform continuous operator problems, such as differential equations, into discrete problems. This transformation involves enforcing linear constraints determined by a finite set of basis functions represented as $\underline{\boldsymbol{w}}^T$. The Galerkin method is often associated with specific assumptions and approximation methods. For instance, the Ritz-Galerkin method typically assumes a symmetric positive definite bilinear form in the weak formulation. This approach often leads to the minimization of a quadratic function representing the system's energy.

This concept aligns closely with the traditional approach of the FEM. In FEM, the solution we seek is projected onto a set of basis functions, and these projections are weighted by the DoFs. In essence, we are seeking to represent the solution as a linear combination of these basis functions.

However, the DGA method introduces a different philosophy. Instead of minimizing energy, it aims to solve an algebraic equation directly. The Galerkin method still plays a role when constructing the mass matrices, where an *energetic approach* is followed.

Lets explore how we build the mass matrices for the equation (2.30). In the following the dependence from the position will be implicit for a better reading. The dissipated power is expressed as:

$$\int_{v_k} \boldsymbol{j}_k^T \boldsymbol{e}_k \, dv, \tag{2.36}$$

where v_k represents the volume of the k-th cell, and $\boldsymbol{j}_k$ and $\boldsymbol{e}_k$ are the electric and current density vectors, respectively. These quantities are combinations of the aforementioned basis functions. Two more straightforward computations follow:

$$\int_{v_k} \mathbf{I}_k^T \underline{\boldsymbol{w}_k} \sigma_k \underline{\boldsymbol{w}_k}^T \mathbf{I}_k \, dv, \tag{2.37}$$

since the DoFs are constant and independent of position:

$$\mathbf{I}_k^T \left(\int_{v_k} \underline{\boldsymbol{w}_k} \sigma_k \underline{\boldsymbol{w}_k}^T \, dv \right) \mathbf{I}_k. \tag{2.38}$$

Here, we encounter the $\mathbf{R}_k$ mass matrix inside the brackets.

A similar approach can be applied to obtain the $\mathbf{M}_k$ mass matrix. Starting from the energy accumulated in the inductive part:

$$\int_{v_k} \boldsymbol{j}_k^T \boldsymbol{a}_k \, dv, \tag{2.39}$$

we notice its equivalence with the electrostatic energy definition:

$$\int_{v_k} \boldsymbol{\phi}_k^T \boldsymbol{\rho}_k \, dv. \tag{2.40}$$

By exploiting the Biot-Savart law, we arrive at:

$$\frac{\mu_0}{4\pi} \int_{v_k} \mathbf{I}_k^T \underline{\boldsymbol{w}_k} \, dv_k \int_{v_h} \frac{\underline{\underline{\boldsymbol{w}_h}}^T \mathbf{I}_h}{r_{kh}} \, dv_h. \tag{2.41}$$

Further simplification yields:

$$\frac{\mu_0}{4\pi} \mathbf{I}_k^T \left(\int_{v_k} \int_{v_h} \underline{\boldsymbol{w}_k} \frac{\underline{\underline{\boldsymbol{w}_h}}^T}{r_{kh}} \, dv_k \, dv_h \right) \mathbf{I}_h. \tag{2.42}$$

For isotropic and linear materials, we have:

$$\frac{\mu_0}{4\pi} \mathbf{I}_k^T \left(\int_{v_k} \int_{v_h} \frac{\underline{\boldsymbol{w}_h} \cdot \underline{\boldsymbol{w}_k}^T}{r_{kh}} \, dv_k \, dv_h \right) \mathbf{I}_h. \tag{2.43}$$

The block matrices associated with the k-th cell are defined as follows:

$$\mathbf{R}_k = \int_{v_k} \underline{\boldsymbol{w}_k} \cdot \sigma_k \boldsymbol{i}_d \cdot \underline{\boldsymbol{w}_k}^T \, dv \tag{2.44}$$

$$\mathbf{M}_{kh} = \frac{\mu_0}{4\pi} \int_{v_k} \int_{v_h} \frac{\underline{\underline{\boldsymbol{w}_k}} \cdot \boldsymbol{i}_d \cdot \underline{\underline{\boldsymbol{w}_h}}^T}{r_{kh}} \, dv_k \, dv_h \tag{2.45}$$

Both of these matrices satisfy the requirements for consistency (correct map from circulations to fluxes) and stability (positive definiteness) for tetrahedral mesh with barycentric subdivision, as is essential in the Ritz-Galerkin method and in DGA. This implies that the circuit equation interpretation is applicable to the Galerkin method. Furthermore, it's noteworthy that both the mass matrix **M** and **R** serve as discrete representations of the Hodge operator. Consequently, the Galerkin method can be seen as a realization of a discrete Hodge operator.

2.3.4 Uniform basis functions

Previously we showed how to obtain the mass matrices for a tetrahedral mesh. Besides,the mass matrices constructed by means of edge and face elements introduced by Whitney and generalized by Nedelec, satisfy both the stability and consistency properties required by DGA, for pairs of grids in which the primal is composed of tetrahedra and the dual grid is obtained according to the barycentric subdivision of the primal. This result unfortunately does not hold in general for edge and face elements relative to different geometries. For instance, Whitney's elements for generic hexahedral primal grids do not satisfy the consistency property required by DGA, for any choice of the dual grid.

In [34] were able to derive novel constitutive matrices satisfying both the consistency and stability properties required by DGA. This was made possible by the introduction of a novel set of edge and face vector functions authors. Unlike the Whitney's elements these set of basis functions was adopted in general for polyhedral elements. They have this form

$$\boldsymbol{f}^p = \frac{1}{|v|} \underline{\boldsymbol{c}}_{n-p}^T \boldsymbol{c}^p, \tag{2.46}$$

where $\boldsymbol{f}^p \in \mathcal{F}^p(\mathcal{K})$ is the uniform reconstructed field, $\boldsymbol{c}^p \in C^p(\mathcal{K})$ is the vector of p-cochains (DoFs). One also recognize the basis function $\underline{\boldsymbol{w}} \in \mathcal{F}^p(\mathcal{K})$ as $\underline{\boldsymbol{c}}_{n-p} / |v| \in C_{n-p}(\tilde{\mathcal{K}})$. Interesting to note that now the basis functions are defined as the dual chains.

It is important to note here that if uniform basis function are adopted the equations for the resistance mass matrix computations become

$$\mathbf{I}_k^T \underline{\boldsymbol{w}_k} \left(\int_{v_k} \sigma_k dv \right) \underline{\boldsymbol{w}_k}^T \mathbf{I}_k, \tag{2.47}$$

whereas the inductance matrix take the form

$$\mathbf{I}_k^T \underline{\boldsymbol{w}_k} \left(\int_{v_k} \int_{v_h} \frac{\boldsymbol{i_d}}{r_{kh}} dv_k dv_h \right) \underline{\boldsymbol{w}_h}^T \mathbf{I}_h, \tag{2.48}$$

where $\boldsymbol{i_d}$ is the 3×3 identity matrix. This class of functions, unlike Whitney's and Nedelec's basis functions, do not satisfy any curl-conforming or div-conforming properties. Thus in DGA, by using a pair of dual grids instead of a single grid, convergence can be guaranteed by using basis functions which do not satisfy all the regularity conditions of Whitney's and Nedelec's basis functions.

The use of uniform basis functions enables the factorization of the inductance matrix, introducing an new family of low-rank inductance matrix compression techniques. These techniques demonstrate a significant improvement in terms of memory occupancy and computational efficiency compared to current state-of-the-art alternatives. This enhancement facilitates the solution of problems with a higher number of DoFs [81].

Indeed, from equation 2.48 is observed that the inductance matrix can be represented as:

$$\boldsymbol{\mathcal{W}} \boldsymbol{M_{1/r}} \boldsymbol{\mathcal{W}^T}, \tag{2.49}$$

where the matrix $\boldsymbol{M_{1/r}} \in \mathbb{R}^{F \cdot V \times F \cdot V}$, with F denoting the number of faces and V representing the number of volumes.

In [81], the matrix in equation 2.49 is manipulated observing that the results of the double integrals for each pair of volumes v_h and v_k in the mesh can be computed and stored in a dense matrix $\mathbb{N}$ with dimensions $V \times V$. The stiffness matrix can then be reconstructed using factorized expressions that involve sparse matrices, with memory occupancy scaling linearly with the number of unknowns in the problem.

This factorization induces a ground-braking speedup of various orders of magnitude with respect to the state-of-the-art solutions (in particular, a popular Adaptive Cross Approximation (ACA) library) thanks to the use of fast summation techniques, like the FMM, to perform the matrix–vector product. Subsequent sections will provide an example of FMM utilization.

2.3.5 Stabilization

In general the Gram matrices $\mathbf{M}$ and $\mathbf{R}$ are positive semi-definite. For a 3D or a 2D problem the basis functions $\boldsymbol{w}$ are a vector in $\mathbb{R}^2$ or $\mathbb{R}^3$, respectively. Whereas the Gram matrix has as much rows and columns as the number of vectors attached to the edges, faces or nodes of the computational cell. It's easy to see that this matrix has not full rank. Indeed the determinant of this matrix is null. This leads to instability on the solution since for instance in a direct solver one has to invert the stiffness matrix.

There are basically two method in literature that are adopted for the solution to this problem [22]. The method of the first type consist in building basis functions which embed a particular part that makes the vector linearly independent where an example can be found in [34]. The second type is to change the properties of the mass matrix and split the mass matrix in consistent part and stabilization part and feed them with appropriate null vectors that belong to the $ker(\mathbf{R})$ ($ker(\mathbf{M})$). Obviously, these vectors are orthogonal to the rows of $\mathbf{R}(\mathbf{M})$. This won't alter the problem, except to replace the rank deficiency of the matrices.

Hence, generally there are build novel resistance ($\boldsymbol{R_s}$) and inductance ($\boldsymbol{M_s}$) matrices as follows

$$\boldsymbol{R_s} = \mathbf{R} + \boldsymbol{S_R}; \quad \boldsymbol{M_s} = \mathbf{M} + \boldsymbol{S_M}, \tag{2.50}$$

where the $\boldsymbol{S_R}$ and $\boldsymbol{S_M}$ are the stabilization part of the resistance and inductance matrix, respectively. They are chosen so that $\boldsymbol{R_s}$ and $\boldsymbol{M_s}$ maintain the properties of symmetric positive definite, and that the stabilization part maps to the null vector. One can also adopt regularizations techniques see [6] and construct $\boldsymbol{S_R}$ and $\boldsymbol{S_M}$ as $\tilde{\mathbf{D}}\mathbf{D}$, also called grad-div regularization technique [56]. This choice assure both the conditions we are requiring such as the symmetry and the positive definiteness of $\boldsymbol{R_s}$ ($\boldsymbol{M_s}$), being sum of symmetric positive definite matrices.

$$\tilde{\mathbf{C}} \left(\mathbf{R} + j\omega \mathbf{M} + \tilde{\mathbf{D}}\mathbf{D} \right) \mathbf{C}$$

2.4 Multiple conductors

Integral formulations based on the solution of the weak form of the so-called Magneto Quasi-Static Electric Field Integral Equation (MQS-EFIE) for eddy current computation [4], [23], [17] are very appealing for a wide range of practical problems in which the electromagnetic interactions are noticeable just for a reduced part of the computational space wherein it is possible to identify a closed conducting region Ω_c immersed in a uniform insulator [77], [103]. In this context we can mention the inductive position sensors based on eddy currents where the eddy currents generated on the target may be affected by the presence of conductors in the neighbourhood of the operating region [50]. Under these circumstances, to have the opportunity of meshing the conductor only can make the difference in terms of computational performance and ease when building the mesh with respect to other more standard approaches as that ones offered by Finite Element Methods (FEM) [20]. Also, this advantage becomes more and more appreciable whenever movements have to be taken into account because, for instance, the conductor is changing its position with respect to a fixed source of magnetic field Ω_s (a coil, for instance).

In fact, the advantage arising from the use of EFIE in presence of multiple conductors is twofold: from the one hand, in every case in which this formulation is applied the geometry has to be meshed just once since with this approach there is no need to build the mesh of the insulator in which the conductors are moving. To the other hand, when the displacement law is unique for all the conductors under analysis, and so their mutual position is fixed, there is no need to reassemble the problem mass-and-stiffness matrix $\mathbf{K}$ at each step of the motion, thus making it possible to assemble and store it just once to then obtain a quick simulation of the space sweep.

Yet, this last benefit tends to be somehow deeply reduced in case of conductors Ω_F whose position undergoes to a different law with respect to the moving objects Ω_M. By recalling that the construction of MQS-EFIE system of equation is affected by the drawbacks of dealing with a fully populated matrix whose computation of the inductive part can often be cumbersome, it is thus clear that whenever Ω_M changes its position with respect to Ω_F the former of the previously mentioned advantages is overcome by the necessity of successively reassembling at least a part of $\mathbf{K}$ in order to take into account the new relative position of Ω_M with respect to Ω_F that will be characterised by a new set of mutual coupling relations.

Here we show how, for MQS-EFIE formulations, this gap can be totally mended by applying domain decomposition techniques, as proposed for instance in [80], in addition to a fast computation of Laplace-kernel-based expressions by means of the Fast Multipole Method (FMM) [62] that in [91] was shown to be effective in reducing the computational time for an hybrid Finite-Boundary Elements (FE-BE) method in presence of motion. The proposed recipe leads to an approximated system of equations whose solution can be found iteratively by means of either GS scheme or GMRES [90].

In the continuation, our novel approach is illustrated by recasting the MQS-EFIE system in an approximated form suitable for slowly moving conductors, neglecting thus the electromotive force induced from the movement. Equations are going to be written in the frequency domain only but we here remark that the same formalism can be extend and thus used even when the electromagnetic problem requires a solution in the time domain [5].

In regards to the method validation we propose a test case where two conductors are in relative motion between each other. Having placed the conductors one above the other the test aims to investigate the effect of the approximated solution of the magnetic vector potential obtained with the FMM at different heights and an accurate one based on the method proposed in [42]. Another aspect taken into account is the computational time where the results have shown an important improvement when applying the FMM making essentially possible the investigation in reasonable time of the effects of conductors in the neighbourhood of eddy current sensors.

2.4.1 MQS-EFIE system for two moving conductors

Let Ω_F and Ω_M be the fixed and the moving conductor in direction d respectively and Ω_S the source feeded with a known current $\boldsymbol{j_s}\left(t\right)$ as depicted in Fig. 2.5. Each conductor has been discretized partitioning thus Ω_F in N_F elements and Ω_M in N_M elements hence obtaining the primal cell complexes $\mathcal{K}_F$, $\mathcal{K}_M$. Let $\mathbf{T}^F$ and $\mathbf{T}^M$ be the unknowns for the fixed and moving domains and finally $\mathbf{b}_s^F$ and $\mathbf{b}_s^M$ the source acting on the fixed and moving domain. The integral formulation (2.54) is modified as follows

$$\begin{bmatrix} \mathbf{K}^F & j\omega\mathbf{K}_M^{FM} \\ j\omega\mathbf{K}_M^{MF} & \mathbf{K}^M \end{bmatrix} \begin{bmatrix} \mathbf{T}^F \\ \mathbf{T}^M \end{bmatrix} = \begin{bmatrix} \mathbf{b}_s^F \\ \mathbf{b}_s^M \end{bmatrix}, \tag{2.51}$$

where the matrices $\mathbf{K}_M^{FM}$ and $\mathbf{K}_M^{MF}$ take into account only the magnetic mutual coupling between the Ω_F and Ω_M due to the eddy current generated on them. From this description, it follows that the off-diagonal blocks $\mathbf{K}_M^{FM}$ and $\mathbf{K}_M^{MF}$ are responsible of the mutual induction effects between the moving and fixed domains. This representation is easily extendable to N different disjoint conductors if $\Omega_c = \Omega_1 \cup \Omega_2 \cup \cdots \cup \Omega_N$ as shown in [80].

Under the hypothesis that $\boldsymbol{j}\left(\boldsymbol{r}\right)$ is uniform in each volume of $\mathcal{K}_F$ and $\mathcal{K}_M$, it has been already shown that the linear application $\mathbf{K}$ maps DoFs into the fluxes of the magnetic induction field across the dual grid faces and that this result can also be directly obtained, via the faces-edges incidence matrix $\mathbf{C}$, by calculating the curl of the integral of $\boldsymbol{a}\left(\boldsymbol{r}\right)$ along the dual grid edges $\tilde{e}$ as showcased in Fig. 2.6.

As a matter of fact, since the off-diagonal blocks of K change at each relative displacement of Ω_M with respect to Ω_F, it is much more convenient to try to compute it on the fly instead of reassembling and storing a matrix that will become useless in a while. In fact, the system can be seen as

$$\begin{bmatrix} \mathbf{K}^F & 0 \\ 0 & \mathbf{K}^M \end{bmatrix} \begin{bmatrix} \mathbf{T}^F \\ \mathbf{T}^M \end{bmatrix} + \\ + \begin{bmatrix} 0 & j\omega \mathbf{K}_M^{FM} \\ j\omega \mathbf{K}_M^{MF} & 0 \end{bmatrix} \begin{bmatrix} \mathbf{T}^F \\ \mathbf{T}^M \end{bmatrix} = \begin{bmatrix} \mathbf{b}_s^F \\ \mathbf{b}_s^M \end{bmatrix}, \tag{2.52}$$

where the off-diagonal terms can be computed on the fly and brought in the right hand side. This announced choice has equally important implications both into the possibility of speeding up the computation by resorting to the FMM and into a more cautious memory use.

2.4.2 Fast Multipole Method and Gauss–Seidel iterative scheme

Let $S = \{M, F\}$ be the set of the conductors and $i \in S$ an element so that $S \setminus i$ consists in all the conductors excluded the i-th one. In the hypotheses that the distance between the two conductors is sufficiently large, the following approximation of the volume integral expression in (2.53) holds

$$\boldsymbol{a}_i\left(\boldsymbol{r}_g^{\tilde{e}}\right) = \frac{\mu_0}{4\pi} \int_{V_{S\setminus i}} \frac{\boldsymbol{j}_{S\setminus i}(\boldsymbol{r}')}{\left|\boldsymbol{r}_g^{\tilde{e}} - \boldsymbol{r}'\right|} dv\left(\boldsymbol{r}'\right) \approx \sum_{k=1}^{N_{S\setminus i}} \frac{\mu_0}{4\pi} \boldsymbol{j}_k \frac{|v_k|}{\left|\boldsymbol{r}_g^{\tilde{e}} - \boldsymbol{r}_g^k\right|}, \tag{2.53}$$

where $\boldsymbol{a}_i\left(\boldsymbol{r}_g^{\tilde{e}}\right)$ is the vector potential computed at midpoint of the dual edge $\boldsymbol{r}_g^{\tilde{e}} \in \Omega_i$. $V_{S\setminus i}$ is the overall volume of $\Omega_{S\setminus i}$ where $\boldsymbol{j}_k$ is constant inside the discrete element with volume $|v_k|$ at the barycentre $\boldsymbol{r}_g^k \in \Omega_{S\setminus i}$.

The approximation in (2.53) enables FMM to be applied in order to rapidly and efficiently compute the Laplace-kernel $1/\left|\boldsymbol{r}_g^{\tilde{e}} - \boldsymbol{r}_g^k\right|$ on a staggered grid of points. Secondly, since FMM is effective in only providing the results of the application of $\mathbf{K}_M^{FM}$ and $\mathbf{K}_M^{MF}$ to the problem DoFs, the solution of (2.52) has to be achieved by means of an iterative scheme that successively computes the effects of the flowing of a given current in a subdomain Ω_i.

The system (2.52) has been solved by applying the (GS) method [62]. It consists in finding iteratively $\mathbf{T}^i \in \Omega_i$ by using the most recent $\mathbf{T}^j$, $j \in$

$S \setminus i$ to compute the contribution $\tilde{\mathbf{\Phi}}^i$ on Ω_i, i.e.

$$\mathbf{K}^i \mathbf{T}^i_{n+1} = \mathbf{b}^i_s - j\omega \tilde{\mathbf{\Phi}}^i_n.$$

The solution $\mathbf{T}^i$ is then updated to be used to find $\mathbf{T}^{S\setminus i}_{n+1}$ in the other conductor $\Omega_{S\setminus i}$.

2.4.3 Numerical Results

As for numerical results, we report an example of eddy currents computed in two conducting plate, one in motion and one fixed, at a frequency of 50 Hz. All simulations are performed on an AMD Ryzen Threadripper PRO 3975WX processor. Each conductor has a length of 200 mm, a width of 120 mm and a thickness of 5 mm, and it is meshed with 936 hexahedra.

The test consists in solving the system (2.52) for different positions of the moving domain by performing consecutive displacement over the z-axis. The distance between the conductors goes from 1 mm to 155 mm as depicted in Fig. 2.7. Table 2.2 shows a comparison between the computation of the magnetic vector potential with the approximated solution (2.53) using FMM with respect to the method proposed in [42]. The latter provide an analytic solution of $\boldsymbol{a}(\boldsymbol{r})$ produced by a uniform current density $\boldsymbol{j}(\boldsymbol{r}')$ in an arbitrary polyhedra with volume $v(\boldsymbol{r}')$.

As far as the power loss inside the conductors is concerned the two methods are in agreement in all the proposed conditions, even in the worst case where the two conductors are close to each other.

Secondly, table 2.2 highlights another aspect, namely the computational time required for finding the solution of the eddy current problem which clearly goes in advantage of the FMM due to the parallelization of the computation of the Laplace-kernel. In fact, the results show a speed up of more than 20 times if compared to the method where the vector potential is computed in closed-form.

Finally, the number of iteration increases when the moving conductor approaches the fixed one. In fact, 4 iterations are sufficient to solve

Table 2.2: *Comparison between the computation time and the power loss when the magnetic vector potential is evaluated as in [42] and by applying the FMM*

Distance between Ω_F and Ω_M [mm]	1	2	5	55	105	155
Power loss ([42]) [W]	23.26	22.36	19.76	6.02	4.94	4.77
Power loss (FMM) [W]	23.29	22.39	19.79	6.02	4.94	4.77
Total computation time ([42]) [s]	600	535	428.4	136.4	98.5	78.4
Total computation time (FMM) [s]	28.4	22.2	17.6	5.8	4	3.3

the problem when the conductors are distant 155 mm whereas the number of iterations increases to 31 when the distance decreases to 1 mm. Since for each movement the solution at the first iteration starts from zero, a possible improvement is to recycle the solution obtained at the old position as starting point for the newer one. Applying this technique to the test case the number of iteration decreased by 5 when the solution at 2 mm become the starting guess for the system at 1 mm. However, the solution of the system at 2 mm showed an improvement of only 3 steps because of a greater distance from the starting guess (i.e. the solution at 5 mm).

2.4.4 Fast simulation of the sensor IPS

For the simulation of the IPS we use a boundary integral method in the hypothesis that the target is a good conductor, i.e. the skin effect is neglected. The target is discretized in 696 triangles (see Fig. 2.8), thus obtaining the primal cell complex $\mathcal{K}$. Starting from $\mathcal{K}$ the dual cell complex $\tilde{\mathcal{K}}$ can be obtained from the barycentric subdivision of $\mathcal{K}$. To each chain of $\mathcal{K}$ or $\tilde{\mathcal{K}}$ a corresponding discrete forms is associated.

The incidence matrices **G** and **C**, which represent the discrete counterpart of the differential operators ***grad*** and ***curl***, maps p-forms to $p+1$-forms $\mathcal{K}$, with $p = 0, 1, 2$ respectively. The relative maps on the dual complex are obtained by transponding this matrices. The eddy current problem for this 2D problem and simply connected domains, writes

$$\mathbf{G}^T \left(\mathbf{R} + j\omega\mathbf{M}\right) \mathbf{G}\Psi = -j\omega\mathbf{G}^T\tilde{\mathbf{A}}_s, \tag{2.54}$$

where Ψ are called stream functions associated to the primal nodes. The matrix $\mathbf{R} + j\omega\mathbf{M}$ is the mass matrix already introduced previously. They map, respectively, currents on the primal edges to voltages $\tilde{\mathbf{U}}$ and magnetic vector potential $\tilde{\mathbf{A}}$ on the dual edges. Finally, the application of the incidence matrix $\mathbf{G}^T$ to these quantities provides the Faraday-Neumann law written in this formulation. Once the solution is found the local current density vector inside a given cell s is computed projecting the global variable current $\mathbf{I}_k$ onto the bases functions.

Now, a first version is to adopt the Raviart-Thomas basis functions on the edges of the triangles building the mesh. The drawback is that the assembling of the mass matrices requires to compute numerically the integrals of equations 2.44 and 2.45 since the basis functions depend on the position. If, on the other hand, uniform basis functions are adopted the mass matrices assembling time, in the case of triangles, has a speed up of x9.

$$\boldsymbol{w}_{e_k} = \frac{\tilde{\boldsymbol{e}}_k}{|s|}, \tag{2.55}$$

where the $\tilde{\boldsymbol{e}}_k$ is the dual edge vector connecting the barycentre of the cell (see Fig. 2.9) with the primal edge $\boldsymbol{e}_k$ and now instead of the volume we have to divide by the surface $|s|$.

Finally, provided $\boldsymbol{j}\left(\boldsymbol{r}\right)$ on the target, the induced voltage on the RXs is computed as

$$V_{RX} = -i\omega \int_{\gamma_{RX}} \boldsymbol{a}_{RX}(\boldsymbol{P}, \boldsymbol{j}_s, \boldsymbol{j}) d\boldsymbol{l}(\boldsymbol{P}), \tag{2.56}$$

where the vector potential $\boldsymbol{a}_{RX}$ on the receivers depends on the evaluation point $\boldsymbol{P}$ the source current $\boldsymbol{j}_s$ and the eddy currents on the target $\boldsymbol{j}$ already computed by solving the MQS problem. The total simulation time for 100 position of the target above the sensor is approximately 40 s. This is huge improvement in terms of speed if compared to FEM solvers which for this type of problems would take several hours in order to reproduce an entire period of the induce voltages.

Fig. 2.10 depict a comparison between the simulated rotary IPS and the measurements. A set of motorized mechanical stages are used to accurately centre the target and rotate it above the sensor. For each position of the target the envelope of the received signal is extracted, thus obtaining the induced voltages V_{rxsin} and V_{rxcos}. The induced voltages have been normalized with respect to the maximum induced voltage on the sine receivers. This is because the current used in the simulator is not compatible with the current used in the measurements where an alternate voltage of 3.5 Vpp at the operating frequency of 2.083 MHz was used. Although the difficulties in centering the target the results show that the values and the shape of the measured error are comparable to the simulated ones thus validating the method.

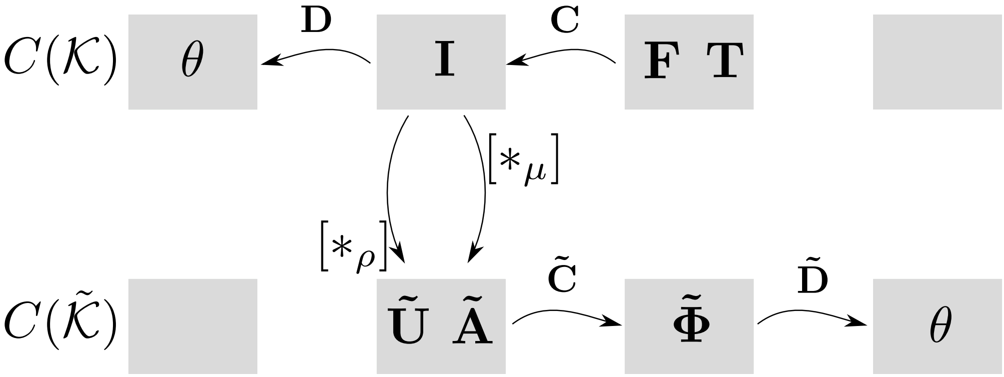

Figure 2.4: *Tonti diagram for the eddy current computation. Not shown in the figure but we have to recall here that* $\tilde{\mathbf{U}} \in C^1\left(\tilde{\mathcal{K}}\right)$, $\mathbf{F} \in C^1\left(\mathcal{K}\right)$, $\tilde{\mathbf{A}} \in B^1\left(\tilde{\mathcal{K}}\right)$ *and finally* $\mathbf{T} \in B^1\left(\mathcal{K}\right)$.

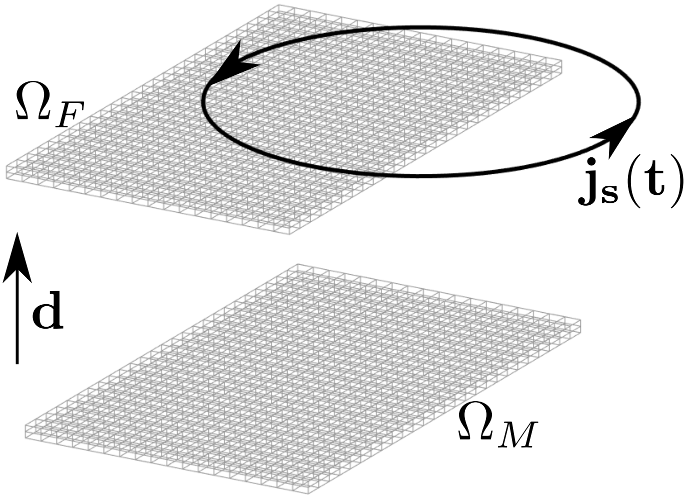

Figure 2.5: *The source* $\boldsymbol{j_s}\left(t\right)$ *acting on the two discretized conductors, one fixed* (Ω_F) *and one movable* (Ω_M) *where* $\boldsymbol{d}$ *is the relative displacement between the conductors.*

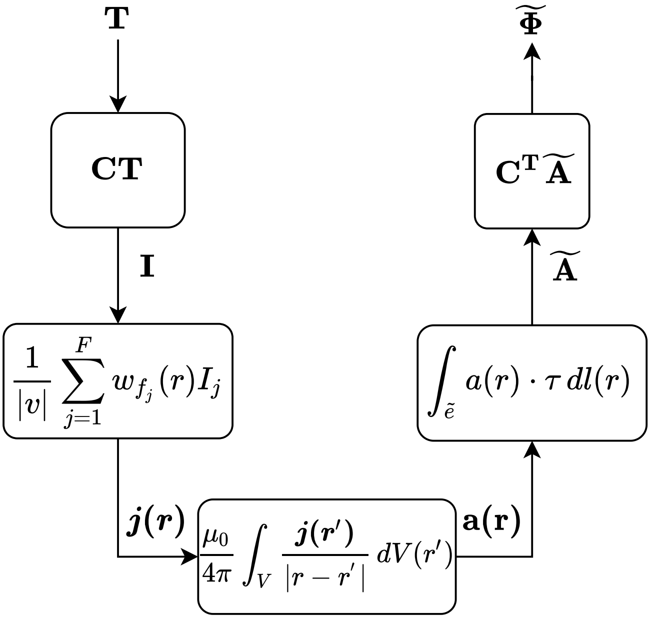

Figure 2.6: *Flow chart from DoFs array to fluxes. The relation between the integral of the electric potential with the fluxes enables the computation on the fly of the off-diagonal term.*

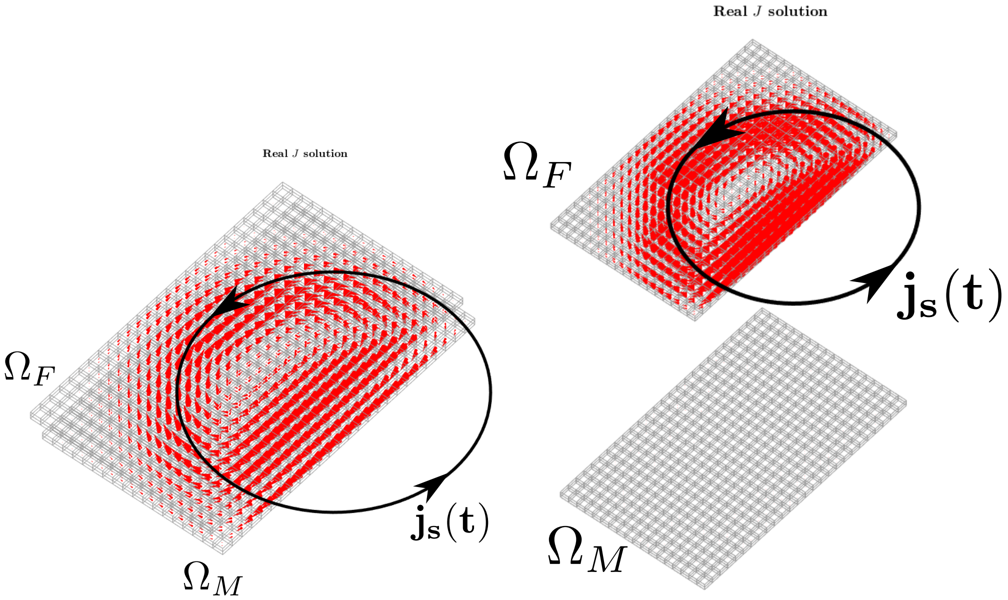

(a) *1 mm gap between* Ω_F *and* Ω_M

(b) *155 mm gap between* Ω_F *and* Ω_M

Figure 2.7: *The problem setting with 2.7a)* $\Re(\boldsymbol{j})$ *when the gap between the conductors is 1 mm and 2.7b)* $\Re(\boldsymbol{j})$ *when the gap between the conductors is 155 mm. The source circular coil in black is powered with a uniform* $\boldsymbol{j_s}(t)$ *current*

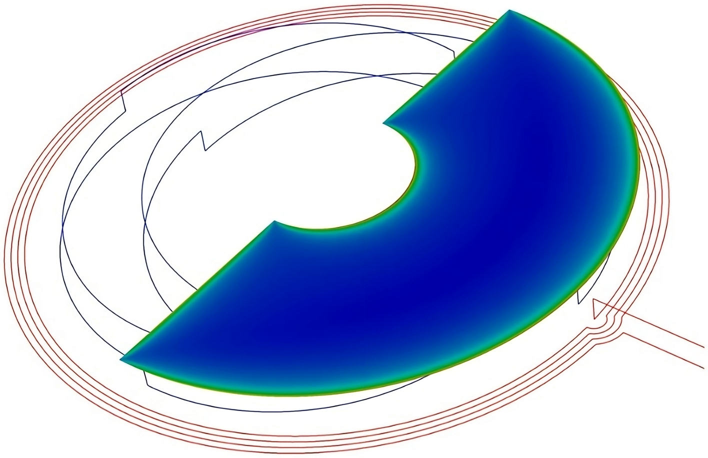

Figure 2.8: *Example of the simulated geometry with the surface integral method. The eddy currents generated inside the conductive body under rotation perturb the received signals.*

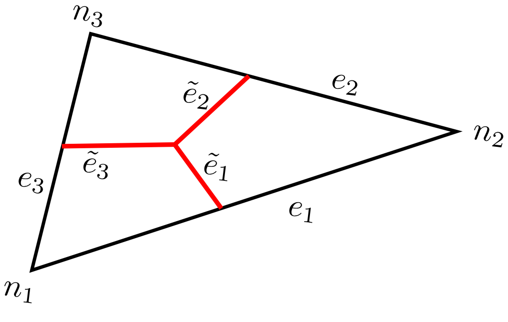

Figure 2.9: *In black the primal cell and in red the dual cell using the dual barycentric subdivision.*

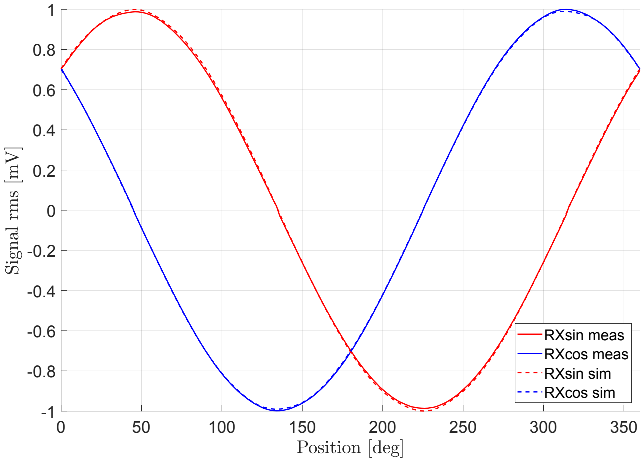

(a)

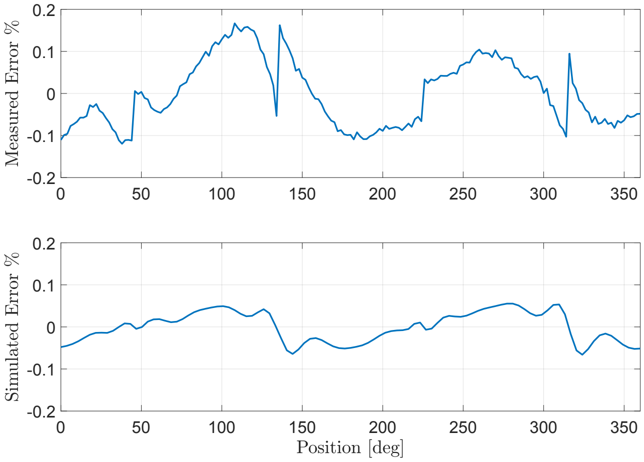

(b)

Figure 2.10: *(a) comparison between the simulated induced voltages and the measured one. (b) comparison between the linearity errors obtained with the best linear fitting line.*

CHAPTER 3

Performance improvement of the rotary IPS

The aim of this chapter is tow fold: 1) to introduce a novel methodology to optimize the design of a ratiometric rotary IPS fabricated in printed circuit board (PCB) technology and 2) increase the amplitude of the induced voltages on the receivers.

Firstly, the optimization aims at reducing the linearity error of the sensor and amplitude mismatch between the voltages on the two receiving (RX) coils. Distinct from other optimization techniques proposed in the literature, the sensor footprint and the target geometry are considered as a non-modifiable input. This is motivated by the fact that, for sensor replacement purposes, the target has to fit a predefined space. For this reason, the original optimization technique proposed in this work modifies the shape of the RX coils to reproduce theoretical coil voltages as much as possible. The optimized RX shape was obtained by means of a Non-Linear Least-Square (NLLS) solver, whereas the electromagnetic simulation of the sensor is performed with an original surface integral method, which are orders of magnitude faster than commercial software based on FEM. Comparisons between simulations and measurements performed on different prototypes of an absolute rotary sensor show the effectiveness of the optimization tool. The optimized sensors exhibit a linearity error below 0.1%FS without any signal calibration or post-processing manipulation.

The aim is to describe the working principle by introducing area-of-overlap functions. We show that each target–receiver pair needs the adoption of a different reconstruction formula for the identification of the target position, whereas in the literature the usual inverse tangent function is applied for every possible pair. Then, we seek the target–receiver pair that maximizes the amplitude of the induced voltages on the receivers. The results show that to achieve the maximum value of the induced voltages, the best choice is to have a rectangular target and rectangular receivers. To verify the theory, simulations and optimization method has been applied to the rectangular receiver coils on two rotary IPS. Measurements performed on the prototypes have shown an increment of the induced voltage of more than 57% with respect to the commonly used sinusoidal receivers. However, a linearity error of 1.5%FS is obtained by using the inverse tangent reconstruction formula. When using the correct formula, the linearity error becomes 0.6%FS for the nonoptimized prototype and below 0.15%FS for the optimized one.

3.1 Optimization of the receivers shape

The correct measurement of the angles is of crucial interest in many industrial, automotive and aerospace applications, where the transducers responses are used to implement a proper controlling procedure. Depending on the physics involved in the sensing mechanism, a categorization of these transducers is possible; we can thus recognize four main types of angle sensors: optical, capacitive, magnetic and inductive ones. Each of those has pros and cons and the choice of one type rather than another depends on the application and the performance of the transducer.

Optical encoders are able to perform precise and high resolution position measurements [76]. Indeed, the displacement measurement by means of optical interferometer can reach sub-nanometer or picometer accuracy [61]. On the contrary, they depend on the working environment as the presence of vibrations or dust may induce an incorrect output [16]. Typically, due to their complex design, these sensors are more expensive if compared to the previously mentioned types [44].

On the other hand, capacitive displacement sensors, such as capacitive rotary encoders, are cheaper and they exhibit a simpler design with respect to optical ones. More than the fact that they have a low power consumption, they also provide high precision measurements [14, 45, 57, 120]. However, their capacitance depends on temperature and humidity and, if used in harsh environment where dust and moisture are also present, the measurements are unavoidably affected by these factors [24, 107].

By exploiting the fabrication techniques of the complementary metal oxide semiconductor (CMOS) technologies, Hall effect and magnetoresistive (MR) position sensors are widely used thanks to the small size, low cost and the full integration with the front end system. If coupled with a permanent magnet, the displacements of the MR or Hall sensor with respect to the magnet results in a variation of their electrical properties. Yet, these sensors are sensitive to external magnetic fields and, moreover, as far as the Hall sensor is concerned, being the magnetic field provided by a non-uniformly distributed permanent magnet, a calibration is mandatory [44, 108, 110, 117].

Finally, the IPS have shown very interesting properties that make them suitable for a wide range of applications where the robustness of the sensor is crucial. A pioneering work in this regard can be found in [69]. Being robust, contactless and immune to thermal variations it is particularly adapted for those applications where the environmental conditions are harsh. They are low cost and they have a reduced size with respect to typical resolvers [106]. Indeed, the sensor is designed i PCB technology. The measurement performed from the sensor are absolute and ratiometric.

Yet, when compared to optical and capacitive transducers, this kind of sensors present a higher linearity error. In order to reduce the linearity error, we propose an original optimization procedure which optimizes the RX coil geometry is proposed. Preliminary results in this regard can be found in [46]. Previously, in [112, 114], the main focus has been the optimization of the target geometry, that however is usually fixed in industrial applications, given that the target has to fit some predefined space. An enabling technology for sensor optimization in a reasonable time is a fast virtual prototyping of the sensor. By exploiting a fast and efficient simulation software based on the surface integral method, combined with a NLLS solver, linearity errors lower than 0.1%FS are achieved. Preliminary results about the simulation method can be found in [78]. We emphasize that this linearity error is obtained without applying any calibration or post-processing manipulation such as offset compensation or induced voltages normalization. The important implication is that the front end circuitry which interfaces with the sensor can be very simple or avoided at all.

3.1.1 Non-ideality effects

The description of the sensor working principle drawn before represents an ideal case; yet, actually, non-ideality effects such as non-linearity, skin effect, tilt of the target, presence of other conductors near the sensing region and a non-uniform distribution of the magnetic field, influence the sensor measure. In what follows, a brief description and a strategy to reduce these effects are given.

The linearity error, defined as

$$\theta^{meas} = atan\left(\frac{U_{rxsin}\left(\theta\right)}{U_{rxcos}\left(\theta\right)}\right), \tag{3.1}$$

is of crucial importance since it defines the variation of the response of the sensor from the ideal curve. The ideal case is the one wherein the response of the sensor depends linearly on the position of the target as predicted in (3.1). As far as the IPSs sensors are concerned, the linearity error basically depends on the difference between the ideal induced voltage and the actual signal picked up by the RXs. This behaviour is very difficult to be predicted, because many geometric factors have a role in this respect, such as the lack of symmetry in the transmitter coil, the non-uniform distribution of the induced magnetic field, the target and the fact that different portions of the RX coils are placed in different PCB layers connected by means of vias.

Second, having a finite conductivity, the shielding capability of a real target is reduced. This factor is expressed in terms of penetration or skin depth, a parameter that depends on the frequency. Table 3.1 shows penetration depths for different conductors in a frequency band that ranges from 2.2 MHz to 5.6 MHz, the values typically used for automotive applications. The skin depth is given by

$$\delta = \sqrt{\frac{1}{\pi f \sigma \mu}}, \tag{3.2}$$

where σ is the target conductivity, μ the magnetic permeability, and f the working frequency of the sensor. If the thickness of the target is relatively small when compared to the penetration depth, the eddy currents generated on the target cannot totally oppose to the external magnetic field that is only partially shielded by the target. Hence, the target thickness has to be at least greater than the penetration depth at the lowest operation frequency. For our purposes, a copper target with a thickness of 35 μm is used, which provides a good shielding efficiency.

Furthermore, the measure is sensitive to the air gap between the sensor and the target, because of the variations on the mutual coupling. In

Table 3.1: *Conductivities and relative skin depth, at automotive application frequencies, for different conductors.*

Material	σ [S/m] at 20°C	δ [μm] at 2.2MHz	δ [μm] at 5.6MHz
copper	5.95×10^7	44	28
aluminium	3.77×10^7	55	35

fact, many proximity sensors exploit this principle in order to measure the distance from a transmitting coil to a target [47]. But, for our purposes, where the focus is on the angle measurements, this distance must be fixed. If the target is not parallel to the sensor surface, then the reaction magnetic field generated by the eddy currents on the target will not oppose uniformly to the magnetic field generated by the TX coil. This implies that the induced voltages on the receivers will present different amplitudes depending on the tilt during the revolution of the target.

Another aspect regarding the non-idealities is the possible presence of metallic parts in the neighbourhood of the operating region of the sensor. This can be considered as an additional source of eddy currents, different from the target, that might perturb the measurements thus increasing the linearity error [49]. Nevertheless, in most applications the environment is controlled, and compensation techniques or simulations, for instance with the method proposed in [59], may be performed in order to take into account or predict this non-ideality effect.

Fig. 3.1 show the presence of two dummy exits as far as the receivers are concerned. They have the important role of making the whole sensor symmetric. Given that the output of the receiver concatenate a certain amount of flux, an *offset* is always present on the received signals. The dummy exits reduce this effect since they contribute with the same amount of concatenated flux as the real output of the receivers.

Finally, the RX coils traces are split between the top and the bottom of the PCB and the electrical connection is maintained through vias. On the other hand, the target is present only on one side of the sensor thus making the shielding effect different from one side to the other of the PCB. The optimization of the receiver coils takes implicitly into account all these effects and it tries to correct the RX coils shape to compensated and reduce them.

3.1.2 Novel sensor optimization

Theoretically, the induced voltages should have a sine and cosine response with the same amplitude during the revolution of the target.

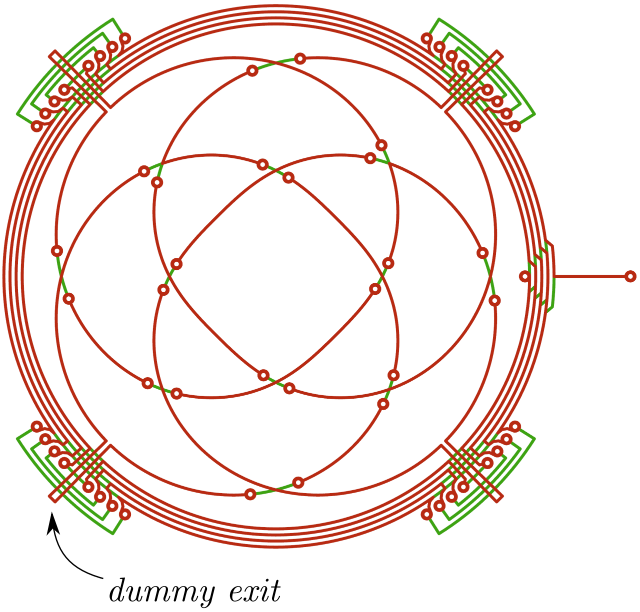

Figure 3.1: *Dummy exits on the rotary IPS.*

Unfortunately, this is not the case in a real device since the non-ideality effects, described in the section 3.2.1, come out. The deviation from the ideal voltages leads to linearity errors higher than other types of sensors.

Attempts in improving the linearity error can be found in [112, 114], where a rotary IPS has been simulated with FEM and optimization algorithms, such as Response Surface Method (RSM) and Particle Swarm Optimization (PSO), are used for searching the optimal geometrical parameter of the device that minimize the linearity error defined as

$$\epsilon_{\%} = 100 \cdot \frac{\|\boldsymbol{\theta}^{meas} - \boldsymbol{\theta}^{id}\|_{\infty}}{\theta_{FS}}, \tag{3.3}$$

where $\boldsymbol{\theta}^{meas}$ and $\boldsymbol{\theta}^{id}$ are, respectively, the measured and the ideal angles for each position of the target.

In [112] the RSM is used to extract an approximated model of the linearity where the model parameters are those that mostly affect the linearity error. The model is obtained by means of a set of 20 experiments and approximated with a second order polynomial where the independent variables are the radian, the thickness of the rotor and the gap of the rotor from the stator. However, no optimization is performed on the stator side.

Unlike the RSM algorithm, the PSO has the advantage of providing a global optimal solution. To identify the relevant parameters which mainly affect the sensor linearity, in [114] a screening procedure is performed consisting of a complete simulated target sweep for each geometrical parameter under investigation such as: excitation coil turn number, coil width, rotor thickness, etc. After the screening phase, only a subset of the parameters to be optimized is selected.

Both these methodologies are time consuming since the screening phase is performed with FEM. Moreover, since only the rotor parameters are optimized, the geometry of the sensor is less flexible. If any geometric parameter changes, for instance the stator dimension, the screening procedure has to be repeated.

Differently, we consider the geometry of the rotor as a fixed input. This is something that happens in most practical cases, where the target has to fit some predefined space or the gap for some reasons is set to a specific value. In this setting, the optimization techniques proposed so far cannot be used. The main novelty of this work is to propose a new methodology for the sensor optimization, that can optimize any sensor with a fixed footprint and a fixed target geometry. The very idea is to automatically modify the shape of the RX coils in such a way that the linearity error is reduced. An enabling technology for the optimization of the RX coil geometry is the fast virtual prototyping of the sensor.

Different optimization algorithms have been tested in order to determine which of them provides the best trade-off between the linearity error and time consumption. Among them the PSO was tested by describing the RX geometry by means of few control points. After the optimization the non-linearity error was below 0.2%FS, but the time required for the optimization was prohibitive. If one would like to better describe the geometry by adding the necessary flexibility to reduce the error toward zero, the number of variables to optimize would increase to the number of points representing the geometry of the receivers. In this case the optimization is not feasible with PSO or any other global optimization technique, because hundreds or thousands of variables needs to be optimized. The best results were obtained by applying a NLLS solver. This approach, available as an off-the-shelf Intel Math Kernel Library routine, gave the best performance in terms of time consumption and non-linearity error if compared to the other algorithms. The non-linear optimizer with trust region iteratively searches the geometric shape of the RX coils, expressed as the radius vector $\boldsymbol{h}$, which minimizes the sensor non-linearity. The problem can be formulated as

$$\min_{\mathbf{h}\in\mathbb{R}^n} \|\boldsymbol{\theta}\left(\boldsymbol{h}\right) - \boldsymbol{\theta}^{id}\|_2^2, \tag{3.4}$$

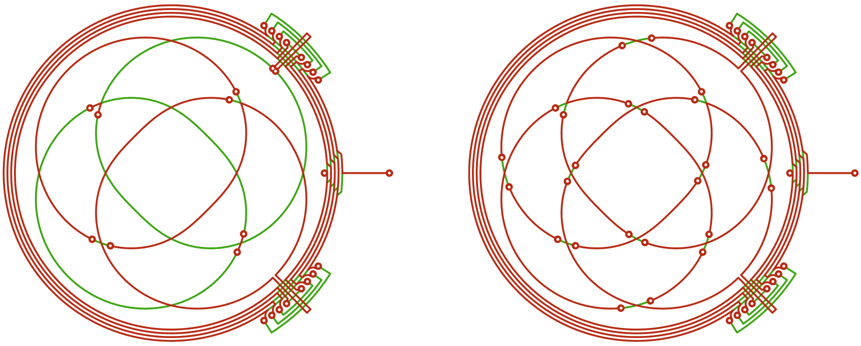

(a) *Design#1* **(b)** *Design#2*

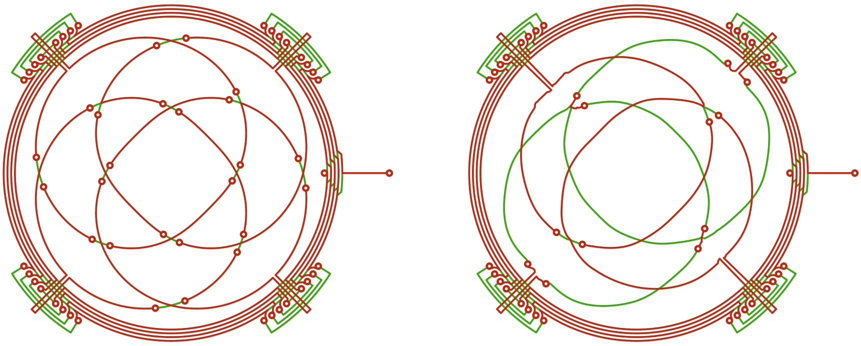

(c) *Design#3* **(d)** *Design#4*

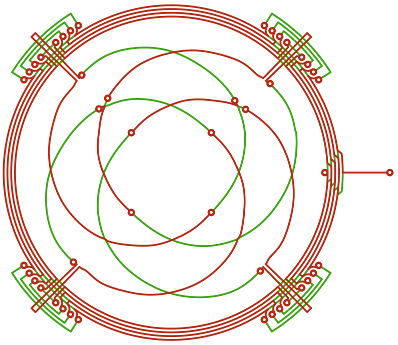

(e) *Design#5*

Figure 3.2: *The set of geometries simulated and measured. (3.2a) receivers placed into separated layers, one on the top and one on the bottom, without optimization; (3.2b) receivers sharing the top PCB layers, without optimization; (3.2c) receivers as in (3.2b) but with the presence of dummy exits which provide symmetry to the sensor that lacks in the previous designs; (3.2d) receivers as in (3.2a) with dummy exits optimized with NLLS; (3.2e) receivers connected with interleaved topology optimized with NLLS.*

where $\boldsymbol{\theta}\left(\boldsymbol{h}\right) \in \mathbb{R}^p$ is the measured vector of the p angles for each position of the target and n is the number of points that define the geometry of the receivers, whereas $\boldsymbol{\theta^{id}} \in \mathbb{R}^p$ are the ideal angles of (3.1).

However, the optimization problem (3.4) has a drawback since the minima reached doesn't assure the same amplitude for both induced voltages. For this reason, the problem is reformulated and the optimizer follows the ideal induced voltages instead of the ideal linearity since the first condition implies the second. Referring to only one receiver, although the optimization is performed in parallel for both of them, the RX shape is determined by

$$\min_{\mathbf{h}\in\mathbb{R}^n} \|\boldsymbol{U_{rx}}\left(\boldsymbol{h}\right) - \boldsymbol{U_{rx}^{id}}\|_2^2, \tag{3.5}$$

where $\boldsymbol{U_{rx}}\left(\boldsymbol{h}\right) \in \mathbb{R}^p$ is the vector of p induced voltages for each p position of the target, $\boldsymbol{U_{rx}^{id}}$ are the ideal voltages and n are the coordinates that define the geometry of the receivers. A Taylor expansion of the function $\boldsymbol{U_{rx}}\left(\boldsymbol{h_{k+1}}\right)$, at the step $\boldsymbol{k+1}$, can be written as

$$\boldsymbol{U_{rx}}\left(\boldsymbol{h_{k+1}}\right) \approxeq \boldsymbol{U_{rx}}\left(\boldsymbol{h_k}\right) + \boldsymbol{J_k s}, \tag{3.6}$$

where $\boldsymbol{J_k}$ denotes the jacobian matrix of $\boldsymbol{U_{rx}}\left(\boldsymbol{h_k}\right)$ and the vector $\boldsymbol{s}$ is the difference between $\boldsymbol{h_{k+1}}$ and $\boldsymbol{h_k}$. By plugging (3.6) into (3.5), the problem can be written as

$$\min_{\mathbf{s}\in\mathbb{R}^n} \|\boldsymbol{J_k s} + \boldsymbol{F}\left(\boldsymbol{h_k}\right)\|_2^2, \tag{3.7}$$

where $\boldsymbol{F}\left(\boldsymbol{h_k}\right) = \boldsymbol{U_{rx}}\left(\boldsymbol{h_k}\right) - \boldsymbol{U_{rx}^{id}}$. Now it is possible to determine the next step by finding the optimal $\boldsymbol{s}$. A possible solution may be obtained by solving the normal equation

$$\boldsymbol{J_k^T J_k s^*} = -\boldsymbol{J_k^T F}\left(\boldsymbol{h_k}\right), \tag{3.8}$$

although other methods can be applied for solving the sub-problem (3.7) within the trust region, as extendedly discussed in [73]. The algorithm ends when the minima or the maximum number of iterations is reached.

3.1.3 Measurements and discussion

A set of measurements have been performed on various geometries of the sensor and a comparison between the physical prototypes and their virtual counterpart is given below. The considered designs are reported in Fig. 3.2. For each design, a Gerber file has been produced and a

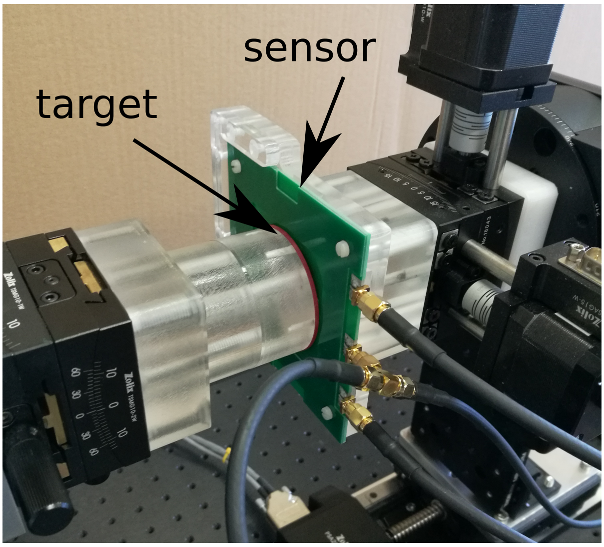

Figure 3.3: *Setup of the measurement for the rotary IPS. After the centering of the conductive target the air gap is set to 1 mm.*

Table 3.2: *Features and relative simulated and measured linearity error for each tested design*

Design	#1	#2	#3	#4	#5
RX on top and bottom	✓	✗	✗	✓	✓
RX only on top	✗	✓	✓	✗	✗
RX with dummy exit	✗	✗	✓	✓	✓
RX optimized with NLS	✗	✗	✗	✓	✓
RX interleaved	✗	✗	✗	✗	✓
Simulated error [%FS]	3.62	0.19	0.25	0.07	0.01
Measured error [%FS]	3.74	0.63	0.44	0.17	0.11

prototype fabricated. In these prototypes the traces have a thickness of 35 μm and a width of 200 μm while the thickness of the PCB is 1.6 mm. An in-house measurement system consisting of a set of motorized and manual precision mechanical stages with 11 degrees of freedom has been built in order to center the target and set the air gap to 1 mm (Fig. 3.3). A signal generator (Siglent SDG6022X) is used in order to feed the TX coil at a frequency of 2.083 MHz and amplitude 3.5 Vpp. A data acquisition board (Picoscope 5000 Series) acquires the received signals from the RX coils and from the TX one. The post-processing consists of extracting the envelope of the received signals.

Table 3.2 provides, for each considered design, a summary of the features and the relative simulated and measured errors, that are described in detail below. The linearity error is computed with respect to the least squares straight line curve which is not required to pass through any specific data point of the sensor output characteristic [74, 87]. It is important to remark that the discrepancy between the virtual and the real prototype is due to the fact that it is very difficult to align the latter with the target into its nominal position, even by using precision mechanical stages. Indeed, a misalignment of some tens of microns can be enough to change the behaviour of the sensor, especially when the linearity error is very small.

The first design (Fig. 3.2a) that has been considered places the two RX coils one in the top of the PCB and the other in the bottom. The reason behind this choice is to avoid as much as possible the presence of vias, that are otherwise necessary when the two coils are placed on the same PCB layer. The shape of the RX coils is ideal, i.e. without optimization. As it can be seen from the measurements performed on this prototype (Fig. 3.4b), the linearity error is higher than 3.5%FS. This error is mainly due to the fact that the amplitudes of the induced voltages are very different between each other because the receiver placed on the bottom of the PCB exhibits a lower signal than the other one (the red line in Fig. 3.4a), because it is further away with respect to the target.

A way to compensate the mismatch between the induced voltages in the two RX coils is to design the receivers on the same layer in order to reduce as much as possible the part of the coil that is located in the bottom layer. The second design (Fig. 3.2b) is implemented in this way and the effect of this adjustment is a general improvement in the simulated and measured linearity, if compared to the Design#1. The measured linearity error is below 0.63%FS (Fig. 3.4d), whereas amplitude of RX coil voltages (Fig. 3.4c), tend to reach the ideal shapes.

Although the improvement in the linearity error between Design#1 and Design#2 is evident, the Design#3 is an attempt to further reduce this error by adding the *dummy exits* (Fig. 3.2c). Indeed, the linearity should improve by making the sensor more symmetric, since the flux linkage should be theoretically balanced. However, Fig. 3.4f shows that there is not a substantial improvement in the linearity even though the physical measurement is slightly more tolerant to misalignments, and it is easier to center the target within an acceptable tolerance.

To achieve a better performance in terms of linearity error the design optimization procedure described in the former sections is adopted. Design#4 and Design#5 (Fig. 3.2d and Fig. 3.2e, respectively) are results of the NLS optimization algorithm. Design#4 is optimized starting from the Design#1 and adding the dummy exit, whereas Design#5 has a different arrangement of the RX coils which is called *interleaved*. The

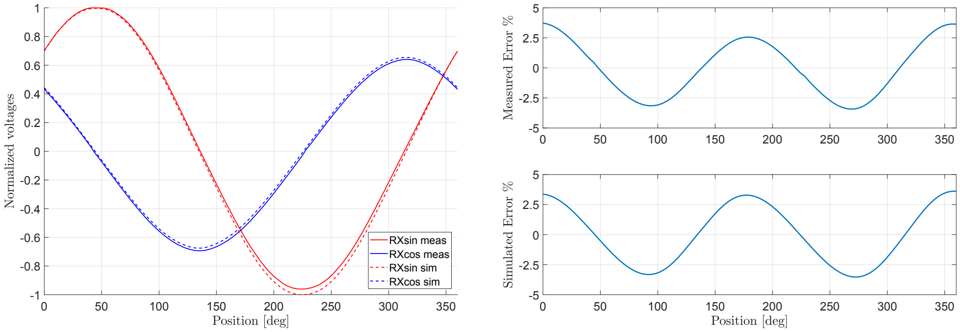

(a) *Induced Voltages Design#1* **(b)** *Linearity Error Design#1*

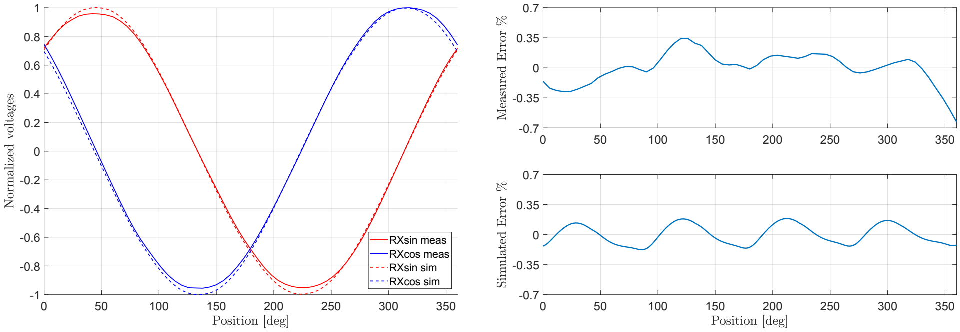

(c) *Induced Voltages Design#2* **(d)** *Linearity Error Design#2*

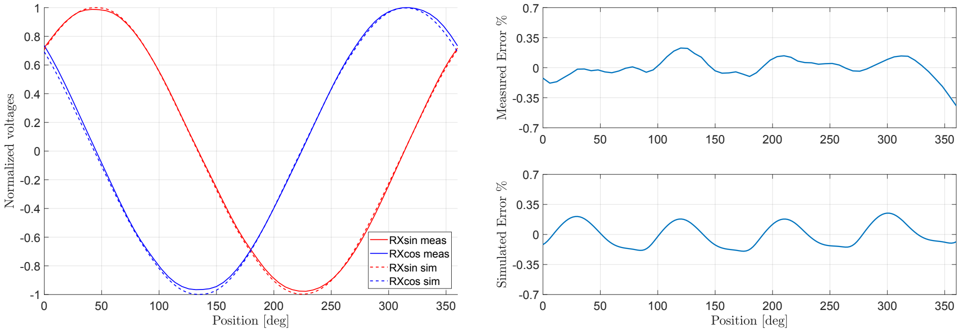

(e) *Induced Voltages Design#3* **(f)** *Linearity Error Design#3*

Figure 3.4: *Comparison between the simulation and the measurements for the non-optimized designs. (3.4a), (3.4c), (3.4e) show the simulated and measured induced voltages. The displayed values are normalized with respect to the amplitudes of the simulated and measured* $\mathbf{U_{rxsin}}$*, respectively; (3.4b), (3.4d), (3.4f) show the linearity errors. The position, which is expressed in degree, refers to electrical angles.*

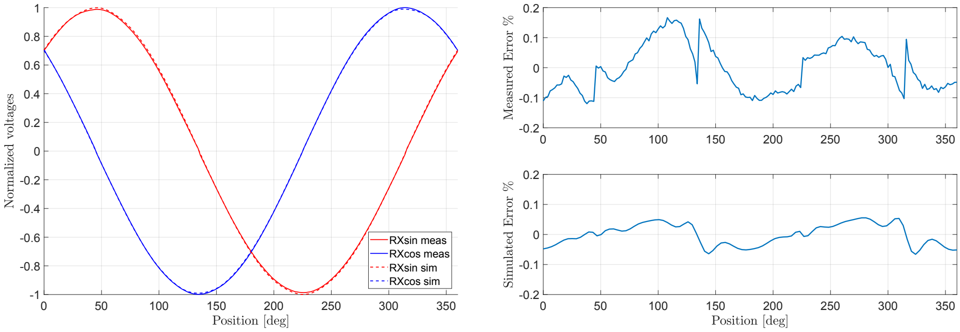

(a) *Induced Voltages Design#4* **(b)** *Linearity Error Design#4*

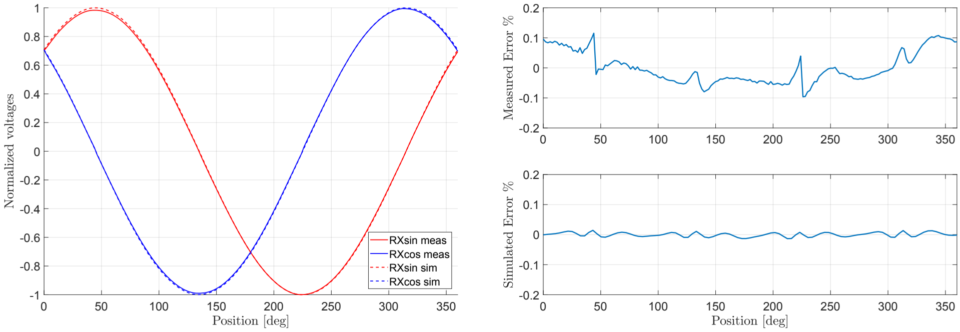

(c) *Induced Voltages Design#5* **(d)** *Linearity Error Design#5*

Figure 3.5: *Comparison between the simulation and the measurements for the optimized designs with NLS. (3.5a), (3.5c) show the simulated and measured induced voltages. The displayed values are normalized with respect to the amplitudes of the simulated and measured $\mathbf{U}_{rxsin}$, respectively; (3.5b), (3.5d) show the linearity errors. The position, which is expressed in degree, refers to electrical angles.*

advantage of interleaving is that the RX coils have the same distribution between the top and the bottom of the PCB. The symmetry offered by interleaving together with the dummy exits provides to the sensor a robust performance with respect to tilt and centering of the target, if compared to all the other designs.

Fig. 3.5b and Fig. 3.5d shows that the simulated error improves noticeably if the NLS algorithm is used. Indeed, simulated errors below the 0.1%FS are achieved for the Design#5 and below 0.01%FS for the interleaved design. The whole optimization of the sensor requires less than half an hour. Nevertheless, the measurements show errors that are higher than the simulated ones. This is due to the measurement setup where the misalignment of the target and the noise of the ADC are responsible for the deviation from the simulated design. Furthermore, this effect becomes more evident when the linearity error is reduced, as the results of the Design#4 and Design#5 show. However, the pattern of the virtual prototype is maintained, and this can be noticed at the zero crossing where the linearity error is zero.

3.2 Optimization of the induced voltages

Our aim in this the following is to investigate whether improvement in the received signal can be performed by modifying the shape of the receivers.

Indeed, the literature [64, 86, 113, 116, 118, 119] shows other types of receiver shapes and this gives us the possibility to seek among different receiver shapes those who maximize the area. The consequence of this choice can be read in two ways: increasing the area of the receiver shape ought to increase also the induced voltages or, equivalently, we can obtain the same value of the induced voltage by reducing the area of the sensor.

A second aspect is to reduce the linearity error maintaining the advantages of the first aspect. To reduce the linearity error means that the distance between the reconstructed position and the theoretical one should be as small as possible. A typical approach to reconstruct the position of the target exploits the fact that the induced voltages are trigonometric functions when a rectangular target moves above sinusoidal receivers. The position of the target is retrieved by using the inverse tangent of the ratio between the sine and cosine induced voltages. We remark that, in the aforementioned works the position is retrieved with the inverse tangent although the shape of the receivers are not sinusoidal functions.

On the contrary, we stress that there is a strict connection between the geometry of the target and the geometry of the receivers such that the reconstruction of the position must take into account this aspect in order to reduce the linearity error. We also provide a simple and useful theoretical tool in order to predict the shape of the induced voltages whenever the geometry of the receivers and target is different from the sinusoidal case. This allows us to model the receivers shape. The result is that there is a specific reconstruction formula for each target–receiver pair and that the maximum value of the induced voltage is achieved when rectangular target and rectangular receiver coil are adopted.

In order to verify the theory, a rotary IPS with rectangular receiver coils has been designed and simulated with the surface integral method [19]. Furthermore, the methodology for the optimization of the linear-

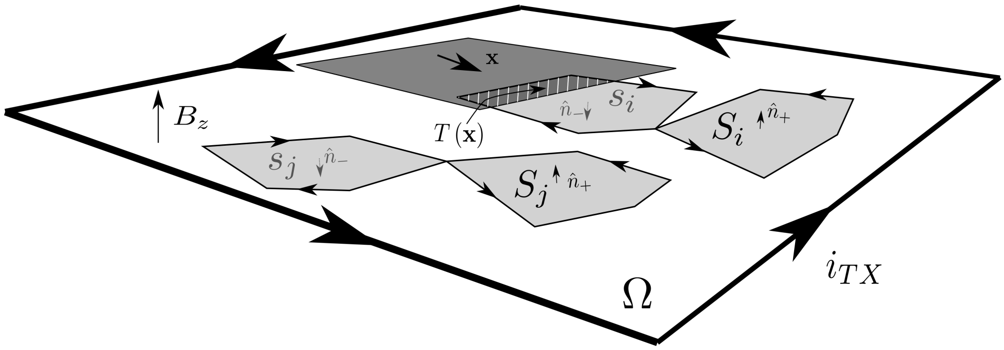

Figure 3.6: *A general representation of geometry of the sensor constituted by a set of receivers, a transmitter and a target. In the figure the target is covering a portion of the i-th receiver of area $T(x)$.*

ity error, previously proposed in [58], has been applied to the aforementioned design. The measurements have shown that the maximum induced voltage is 64% higher than sinusoidal receiver shape whereas the linearity error (computed adopting the correct formula) without optimization is 0.6% and after the optimization is 0.15%FS.

3.2.1 General working principle

In a very general setting, Fig. 3.6 depicts the IPS where the target is moving above the receivers following a certain trajectory **x**. The transmitter coil is driven by a known alternate current i_{TX}, thus generating a variable magnetic field within the region Ω. The twisted receivers collect an amount of flux proportional to the area. Since the number of the receivers might be more than one, we index the areas representing the i-th receiver with the proper oriented surfaces S_i and s_i.

For the description of the ideal working principle of the sensor we assume the magnetic field generated from the transmitting coil to be uniform and orthogonal to the plane where the receivers lie. We assume also that the reactive field, due to the eddy currents generated inside the target, perfectly shields the external magnetic field.

Considering the receiver uncovered from the target (in Fig. 3.6 the j-th receiver), the measure of the induced voltage performed with such a geometry depends on the net flux Φ_j, which can be written as

$$\Phi_j(t) = \int_{S_j} \mathbf{b}(t) \cdot \mathbf{n}^+ dS + \int_{s_j} \mathbf{b}(t) \cdot \mathbf{n}^- dS, \tag{3.9}$$

where $\mathbf{n}^+$ and $\mathbf{n}^-$ are the external orientation of the surfaces S_j and s_j, respectively. Being the induced magnetic field purely sinusoidal we apply the Steinmetz representation to (3.9). In the aforementioned assumptions the imaginary part of the induced voltage at the j-th receiver depends only from the area as follows

$$V_j\left(\omega\right) = -\omega B_z \left[\int_{S_j} dS - \int_{s_j} dS\right], \tag{3.10}$$

where B_z is the amplitude of the induced magnetic field.

From now on we would assume to work at the fixed frequency f_0 and will normalize the induced voltage with the value $-\omega_0 B_z$. Let $\mathcal{V}_i$ be the normalized voltage of the i-th receiver.

When the conductive target covers a portion of the receiver, such as the i-th receiver in Fig. 3.6, due to the eddy currents generated inside the conductor, the induced voltage depends on the portion of area covered by the target and also from the trajectory as

$$\mathcal{V}_i\left(\mathbf{x}\right) = \int_{S_i/T(\mathbf{x})} dS - \int_{s_i/T(\mathbf{x})} dS, \tag{3.11}$$

where $S_i/T\left(\mathbf{x}\right)$ consist in the area of S_i uncovered from the target. The same considerations can be done for the negative part.

The equation (3.11) can be generalized to N domains, for instance whenever multiperiod sensors are considered, composing the i-th receivers by defining the functions

$$\Psi_k\left(\mathbf{x}\right) = \left(S_k - s_k\right) + \int_{T(\mathbf{x})} dS; \quad \psi_k\left(\mathbf{x}\right) = \left(s_k - S_k\right) + \int_{T(\mathbf{x})} dS, \tag{3.12}$$

and compute the total induced voltage for the i-th receiver as the sum

$$\mathcal{V}_i\left(\mathbf{x}\right) = \sum_{k=1}^{N} \Psi_k\left(\mathbf{x}\right) - \psi_k\left(\mathbf{x}\right), \tag{3.13}$$

where $\Psi_k\left(\mathbf{x}\right)$ and $\psi_k\left(\mathbf{x}\right)$ are the positive and negative contributions to the induced voltage, respectively. We will call these functions area-of-overlap functions, as defined in [71].

Till now we haven't considered any constraint about the geometry of the receivers and the target. All we can say is that $\mathcal{V}_i\left(\mathbf{x}\right)$ is a bounded function. Indeed,

$$\min_{1\le k\le N} -s_k \le \mathcal{V}_i\left(\mathbf{x}\right) \le \max_{1\le k\le N} S_k. \tag{3.14}$$

In order to achieve the maximum (minimum) value, the target has to cover the area of the maximum (minimum) surface when it moves along the trajectory $\mathbf{x}$. Actually, $\mathcal{V}_i(\mathbf{x})$ is in general very complex to define since it depends on the trajectory of the target, on the target and receiver geometries. Similar problems, where the geometry of two convex bodies have to be matched, arise when dealing with motion planning applications and their complexity is pointed out in many works, [1,15,28]. Here, the shape of the target and of the receivers are free parameters. Furthermore, since we don't have constrains on the target geometry, a trivial one which covers the surface of the receiver is that who coincides with the receiver itself. However, we have to take into account also the trajectory followed by the target, given that it determines the dimension of the sensor. Indeed, we consider only translation of the target on a fixed straight line. In particular, those lines such that the receiver is completely covered by the target.

Let w denotes the width of the receiver, that is, the minimum distance between two parallel lines enclosing the receiver, [1]. Thanks to the mean value theorem we can find a rectangular representant for the receiver which has the same width but minimum length, hence minimum size. As a consequence, we will consider only rectangular target moving above the surface S_k or s_k with a constant velocity $\dot{\mathbf{x}}$ and has the capability to cover all the surface.

The term velocity is introduced on purpose since

$$\frac{d}{dt}\mathcal{V}_i(\mathbf{x}) = \nabla\mathcal{V}_i(\mathbf{x}) \cdot \dot{\mathbf{x}} \tag{3.15}$$

highlights the fact that there is an energetic interpretation of (3.15) being $\nabla\mathcal{V}_i(\mathbf{x})$ a force and $\dot{\mathbf{x}}$ a velocity, [7]. Hence, a more general framework can be applied to this functionals, thus giving the possibility to analyze, model and adapt novel receivers shapes. We limit ourselves, instead, in showing how the area-of-overlap functions look like in simple cases, in particular for a linear geometry of the IPS. The rotary and arc sensors can be obtained from a change of coordinates from cartesian to polar.

Fig. 3.8 shows the graph of the function $\Psi(\mathbf{x})$ when the target is moving above the receivers represented in Fig. 3.7. The request of the differential measurement means to require S_k to be equal to s_k. Hence, the area-of-overlap functions depend only on the area covered by the target. As expected, these functions reach the maximum value when the target covers completely the surface.

In general, we can choose among different trajectories in order to reach the maximum values of $\Psi_k(\mathbf{x})$ (equivalently $\psi_k(\mathbf{x})$) but, if we are able to endow the receivers geometry with a characteristic shape such that at the trajectory $\mathbf{x}^*$ the area-of-overlap functions results in closed form then we can exploit this fact to retrieve the position of the target.

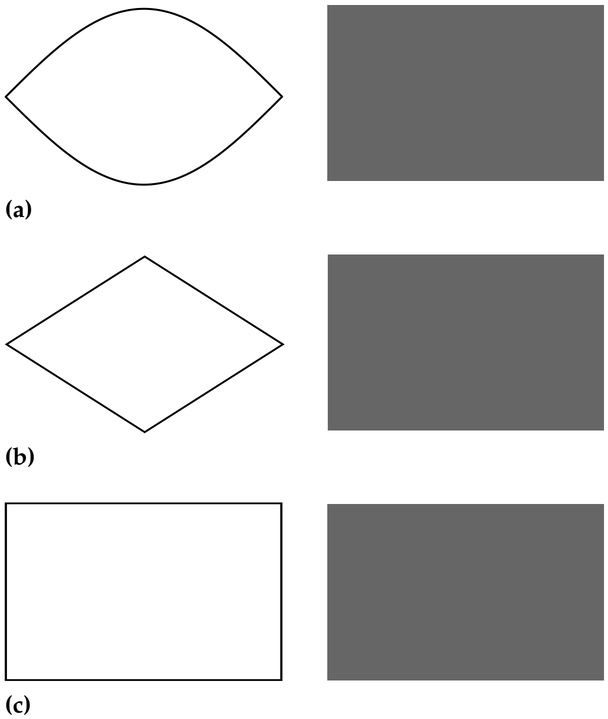

Figure 3.7: *Different receivers geometry (left) with rectangular target (right): (a) sinusoidal receiver; (b) rhombic receiver; (c) rectangular receiver*

Let us consider a sinusoidal receiver shape (see Fig. 3.7a) coupled with the rectangular target. If the x-axis is chosen as path $\mathbf{x}^*$, then the function $\Psi_{sin}\left(x^*\right)$ ($\psi_{sin}\left(x^*\right)$) is a cosine function of the position. Fig. 3.8a depicts the graph of the area-of-overlap function and the red dots its values when the target is moving along the trajectory x^*. The position of the target is easily achieved by considering the inverse function of the cosine. On the other hand, if we endow the receivers with the cosine shape, the primitive is the sine. This gives the possibility to design two receivers, in phase and in quadrature with respect to the x^*, such that the ratio between $\mathcal{V}_{sin}\left(x^*\right)$ and $\mathcal{V}_{cos}\left(x^*\right)$ is invertible with the inverse tangent function as

$$\hat{x} = atan\left(\frac{\mathcal{V}_{sin}\left(x\right)}{\mathcal{V}_{cos}\left(x\right)}\right). \tag{3.16}$$

This is the standard method to reconstruct the position of the target.

If we adopt the rectangular receiver, on the one hand, comparing the geometry depicted in Fig. 3.7c with that of Fig. 3.7a, it is easy to observe that the maximum value of $\Psi\left(x^*\right)$ is subject to an increment

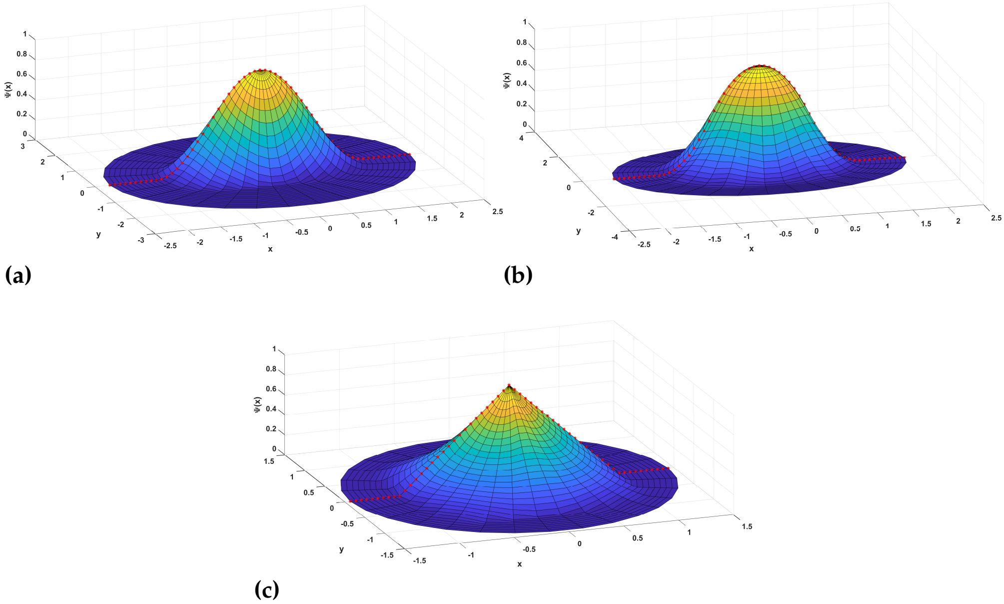

Figure 3.8: $\Psi(\mathbf{x})$ *on the preselected geometries (a) sinusoidal receiver; (b) rhombic receiver; (c) rectangular receiver. The red dots indicate the predefined path followed by the rectangular target.*

of $\frac{\pi-2}{2}$, which correspond to 57% of signal increment. On the other hand, we cannot apply the usual reconstruction formula as done for the sine and cosine shape of the receivers. Fig. 3.8b shows that the induced voltage of a rectangular receiver and rectangular target has a triangular shape (red dots). With the same considerations about the sine and cosine shape we can consider a second rectangular receiver which is shifted in quadrature with respect to the in phase receiver and try to perform a ratiometric measurement.

Let $\mathcal{V}_I(x^*)$ and $\mathcal{V}_Q(x^*)$ be the induced voltages on the in-phase and in-quadrature receivers, respectively. Being this functions affine we have that the correct formula to be used in order to reconstruct the position of the target is

$$\hat{x} = \begin{cases} \frac{L}{4}\frac{m(x)}{m(x)+1} & \text{if } \mathcal{V}_I(x)\,\mathcal{V}_Q(x) > 0, \\ -\frac{L}{4}\frac{1}{m(x)-1} & \textit{otherwise}. \end{cases} \tag{3.17}$$

where $m(x)$ corresponds to $\mathcal{V}_I(x)/\mathcal{V}_Q(x)$ whereas L is the length of the sensor. For instance, L is equal to 2π for an absolute rotary sensor or $2\pi/n$ if an incremental IPS with n periods is used. Other types of reconstruction formulas will lead to a wrong measure, thus affecting

Table 3.3: *Design parameters of the simulated IPS*

Input Feature	Values
Receiver minimum radius	6 mm
Receiver maximum radius	14 mm
Target min radius	5 mm
Target max radius	16 mm
Air gap	1 mm
PCB thickness	1.6 mm
Transmitter number of turn	4
Modulation amplitude	0.65 mm

directly the linearity error.

Finally, Fig. 3.7b shows the rhombic receiver as proposed in [64]. For this receiver the area can be computed given the maximum diagonal $[-T, T]$ and the minimum diagonal $[-t, t]$. The target is rectangular with width $2t$ and length $2T$. We identify his position with his barycentre. Depending on the position of the target the in-phase area-of-overlap function writes

$$\Psi_I(x) = \begin{cases} t(x+T) + \frac{t}{2T}\left(x^2 - T^2\right) & \text{if } \frac{-3T}{2} \leq x < -T, \\ t(x+T) + \frac{t}{2T}\left(x^2 - T^2\right) + \frac{tT}{2} & \text{if } -T \leq x < 0, \\ t(-x+T) + \frac{t}{2T}\left(x^2 - T^2\right) + \frac{tT}{2} & \text{if } 0 \leq x < T, \\ t(-x+T) + \frac{t}{2T}\left(x^2 - T^2\right) & \text{if } T \leq x \leq \frac{3T}{2}. \end{cases} \tag{3.18}$$

As we can see, the function $\Psi_I(x)$ is a second order polynomial. The reconstruction position can be obtained inverting the Ψ_I at the proper interval in order to obtain $\hat{x} = \Psi_I^{-1}(x)$.

We conclude this section with the linearity error formula. This parameter is computed as

$$\epsilon_{\%} = 100 \cdot \frac{\|\hat{x} - x_{ref}\|_\infty}{FS}, \tag{3.19}$$

where x_{ref} is the reference line and FS is the full scale. For instance, FS is 2π for an absolute rotary IPS.

3.2.2 Simulation and optimization for the rotary IPS with rectangular receivers

Lets now apply the rectangular receiver shape coupled with a rectangular target to an absolute rotary IPS. In order to predict the induced voltages on the receivers, the sensor has been simulated with the *surface integral method* proposed in [19]. In particular, the method is applied to the conductive target that has been discretized with 424 nodes, 696 triangles and 1119 edges. Preliminary results about the simulation method applied on IPSs with sinusoidal receivers can be found in [79] and [58], where the simulation method has been extensively discussed and here we briefly recall the main advantages.

On the one hand, the integral method, when compared to the FEM, does not require to re-mesh the domain during the motion of the target above the sensor because only the conductors are meshed. This provides a speed-up in the simulation of the sensor passing from hours to seconds for a full simulation. On the other hand, it provides a fully populated matrix, which reduces the size of the problems that are possible to solve.

Table 3.3 represents the geometric parameters of the sensor with the rectangular receivers. Some preliminary considerations which deviates from the theory has to be made before simulating the design.

First, in order to achieve a physically feasible design, the copper traces of the receivers should pass on the top and on the bottom of the PCB. The electrical connection is maintained through vias, but in order to avoid via–trace collisions we had to assure a certain gap between the traces and the vias. Hence the radius of the receivers has been modulated with an amplitude such that this problem is solved (see Fig. 3.9a).

Secondly, having a greater area due to the modulation, we expect that the induced voltages has to be greater than the theoretical results, i.e. signals 57% higher with respect to the sinusoidal receivers.

Thirdly, the receivers are placed on the top and on the bottom of the PCB, whereas the target lies only on one side. This implies that the eddy currents generated on the target influence more the receiver traces on the layer near the target. Moreover, this introduces a subtle and more general effect which is the non-uniform distribution of the magnetic field above the sensor.

Finally, the air gap is also not considered on the proposed theory. Actually, the reactive magnetic field of the target cannot completely oppose the external induced magnetic field. Indeed, as the air gap between the target and the receivers increases, it doesn't shield totally the covered surface.

Although the assumptions of the theory proposed in the Section 3.2.1 might seem too restrictive, however all these effect are well explainable. Indeed, a change of trajectory from the ideal x^* to another trajectory results in a the deviation of $\Psi(x)$ from $\Psi(x^*)$. Furthermore,

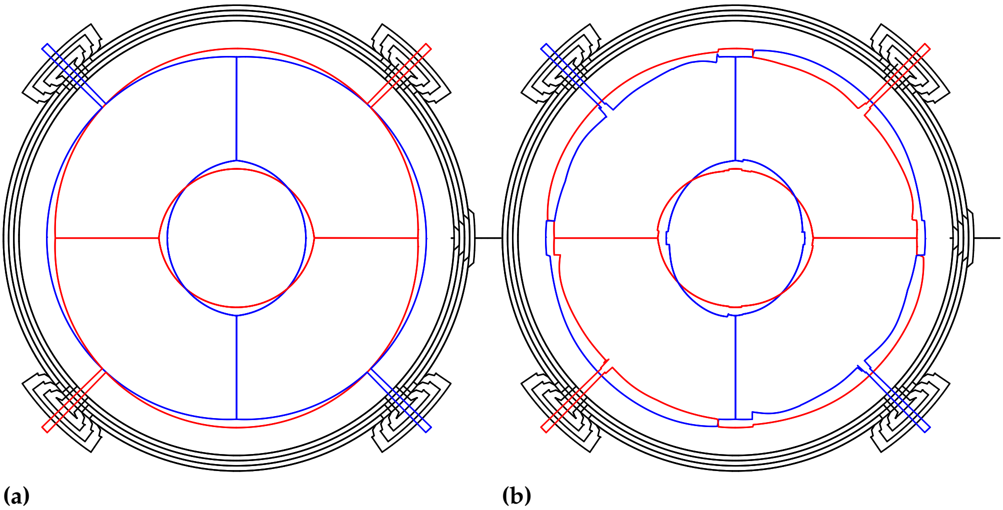

Figure 3.9: *Geometry of the receivers for an absolute rotary IPS: (a) non-optimized; (b) optimized with NLLS. In phase receiver (red), In quadrature receiver (blue), transmission coil (black).*

the air gap results in the fact that $graph\left(\Psi_{ag}\left(x^{*}\right)\right)$ is interior to the optimal $graph\left(\Psi\left(x^{*}\right)\right)$. We recall that a graph of a function f defined on a domain D represents all those couples $\left(x,f\left(x\right)\right)$ such that $x\in D$. A combination of this two effects affects negatively the reconstruction of the position of the target.

To show the effect of the variable air gap, two simulations have been performed on the previous designs. If we focus the attention at the peaks of the induced voltages for the non-optimized designs (Fig. 3.11 and Fig. 3.12), we can observe that they become smoother as the distance of the target from the sensor increases. However, the induced voltage slope is far from being linear. The linearity error is poor even if we approach the target to the sensor because we are not acting on the second non ideality (i.e. the non uniform distribution of the magnetic field).

To improve the linearity error of an absolute rotary IPS with sinusoidal receivers, an optimization method has been presented in [58]. Indeed, it was shown that it is possible to exploit the speed of the simulator in order to optimize the receivers shape with the NLLS optimizer. We apply this method also to the rectangular receiver shape taking care to apply the correct formula for the reconstruction of the position. Fig. 3.13 and Fig. 3.14 show that the optimization positively impact on the induced voltages and consequently on the linearity error. Aside the

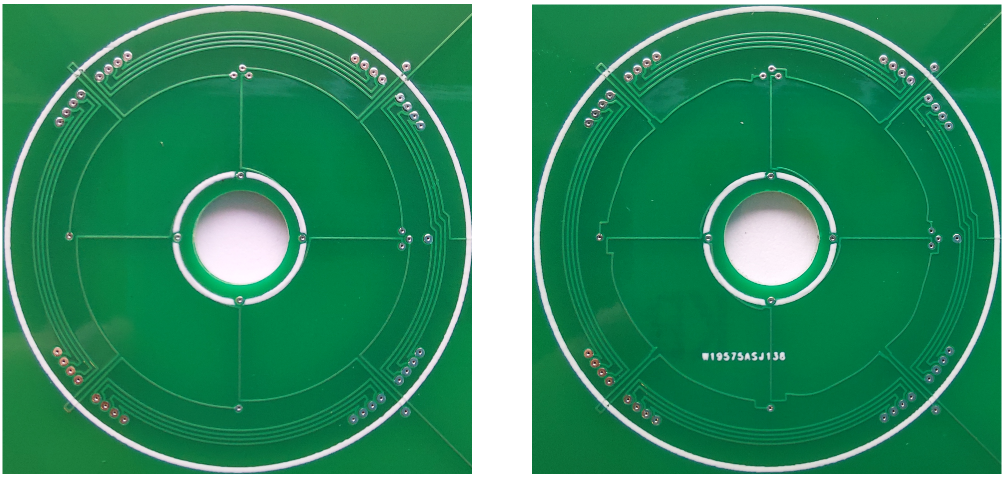

(a)

(b)

Figure 3.10: *Geometry of the prototypes: (a) non-optimized; (b) optimized with NLLS.*

peaks, the slope of the induced voltages become linear. With an air gap of 0.5 mm it is possible to observe that the induced voltage tend to approach the reference line also at the peaks. This is observable in Fig. 3.14a and Fig. 3.14b, where the linearity error decreases as the induced voltage is more similar to the reference. However, for fabrication constraint, we have to exclude from the optimization the points where the vias lies. Thus, at the zero crossing, the linearity error shows peaks of similar amplitude as for the 1 mm gap.

3.2.3 Measurements and discussion

Two PCB-based prototypes, based on the designs previously described, have been tested with an in-house measurement system consisting of a set of motorized and manual precision mechanical stages with 11 degrees of freedom. It is needed in order to centre the target. We adopt an air gap of 1 mm, which is a typical value used in automotive or industrial applications.

The signal generator (Siglent SDG6022X) feeds the transmitting coil at a frequency of 2.083 MHz with an amplitude of 3.5 Vpp. The frequency adopted for the measurements is within the automotive standards frequency. The data acquisition board (Picoscope 5000) acquires the received signals from the receivers coils and from the transmitting one. All these samples are collected and the post-processing consists of extracting the envelope of the received signals.

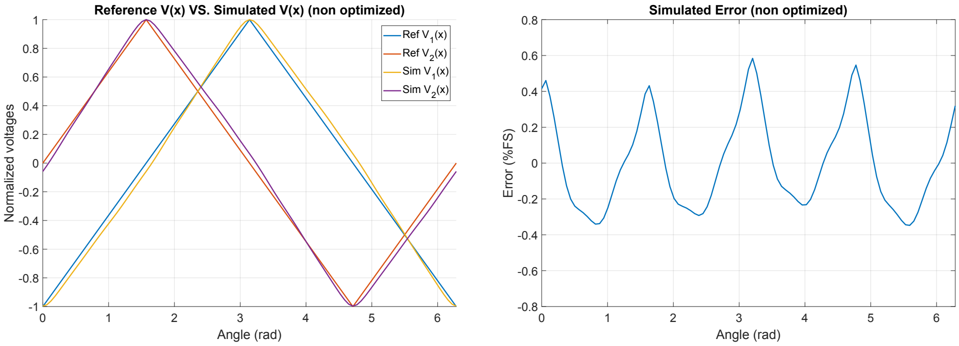

(a) **(b)**

Figure 3.11: *Simulation of the non-optimized sensor with an air gap of 1 mm: (a) induced voltage; (b) linearity error.*

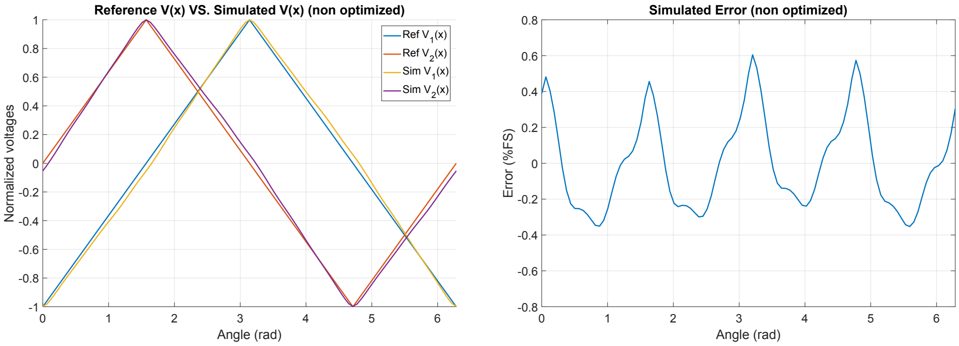

(a) **(b)**

Figure 3.12: *Simulation of the non-optimized sensor with an air gap of 0.5 mm: (a) induced voltage; (b) linearity error.*

The linearity error is computed with the formula (3.19), where x_{ref} is the least squares straight line curve. It is important to note that this curve is not required to pass through any specific data point of the sensor output characteristics [75]. For the reconstruction of the position of the target the formula (3.17) is used.

Fig. 3.15 and Fig. 3.16 depict the results of the measurements. The values of the induced voltages are normalized with respect to the infinity norm of one receiver. The measurements show very good agreement with the simulations although the difficulties of centering the target. Indeed, very little variations are sufficient to bring the induced voltage away from the ideality, thus leading to an error in the measurement.

The induced voltages of the non-optimized sensor show the same

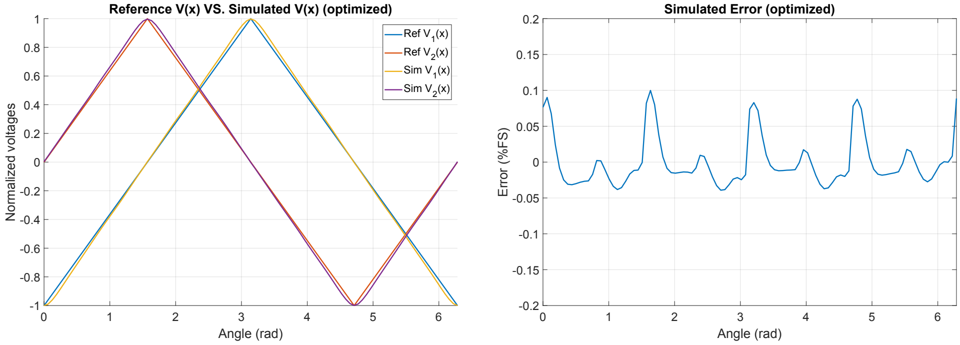

(a) **(b)**

Figure 3.13: *Simulation of the optimized sensor with an air gap of 1 mm: (a) induced voltage; (b) linearity error.*

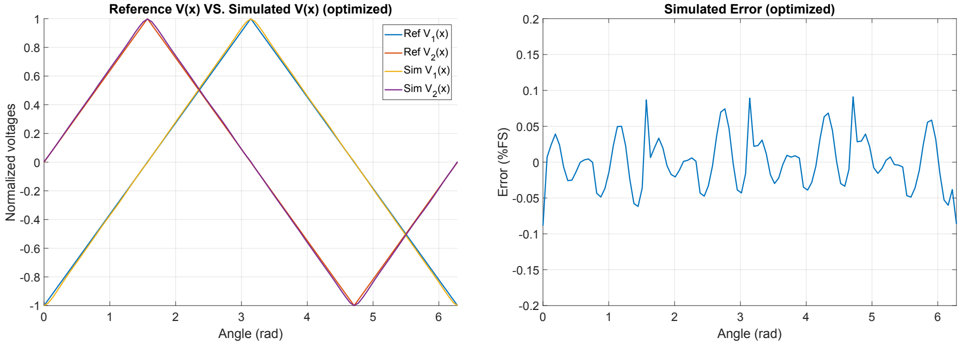

(a) **(b)**

Figure 3.14: *Simulation of the optimized sensor with an air gap of 0.5 mm: (a) induced voltage; (b) linearity error.*

behaviour if compared to the simulations. It can be noticed how 1.6 mm between the top and the bottom of the PCB can affect the induced voltage. To explain why, lets suppose the target covers the area S_1 of the first receiver. Thus, the induced voltage is maximum in that receiver and is proportional to s_1. On the other hand, the induced voltage on the second receiver ought to be zero, but this value will never be achieved since $S_2/2$ of the receiver is on the top and the other one $s_2/2$ is on the bottom. Having the same area but different magnetic fields acting on those areas the error becomes evident. Indeed, in those positions the error reaches the maximum value of 0.6%FS.

As far as the optimized sensor concerns shows a important decrement of the error passing from 0.6%FS to approximately 0.15%FS. The

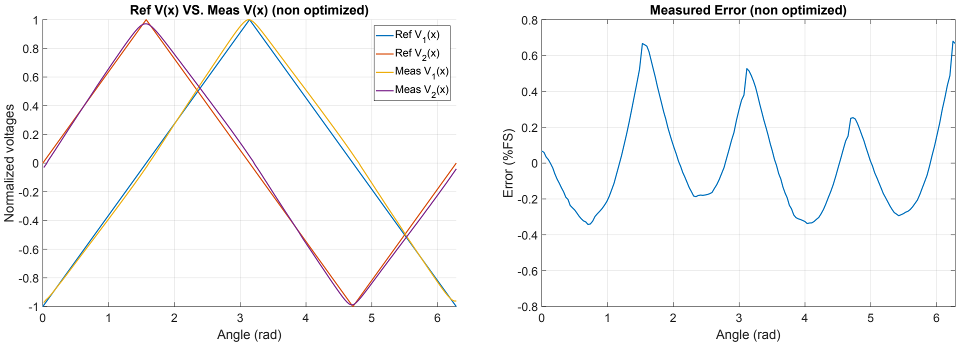

(a) **(b)**

Figure 3.15: *Measurements for the non-optimized sensor with an air gap of 1 mm: (a) induced voltage; (b) linearity error.*

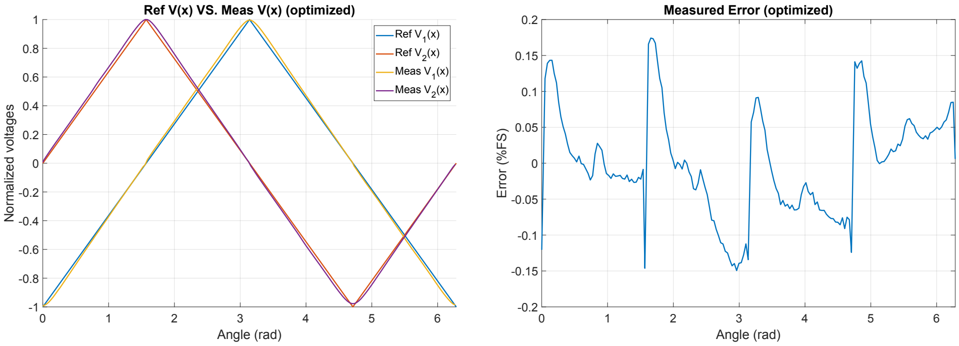

(a) **(b)**

Figure 3.16: *Measurements for the optimized sensor with an air gap of 1 mm: (a) induced voltage; (b) linearity error.*

first thing to notice is how the areas in the bottom of the receiver are enlarged by the optimizer in order to compensate the lack of flux.

Secondly, the errors are comparable with the simulations but generally higher. From the figures, it is possible to observe a discontinuous behaviour at the zero crossing, which are the points where the optimizer cannot act due to geometrical constraints given by the presence of vias. Although this effect was already present in the simulation, it becomes even more evident in the measurements.

It is important to note that, for the position reconstruction, the proper formula has to be adopted. If we instead use the inverse tangent formula linearity errors greater than 1.5%FS affects the measure.

Finally, Fig. 3.18 shows a comparison of the induced voltage obtained with the rectangular coil versus the induced voltages obtained with sinusoidal coils having the same size and the same geometrical parameter as presented in the Table 3.3. It is evident that there is a gain of approximately 64% on the induced voltages. As we expected the value is higher than theoretical value of 57% due to the fact that we modulate on purpose the radius of the receivers in order to respect the via to trace distance.

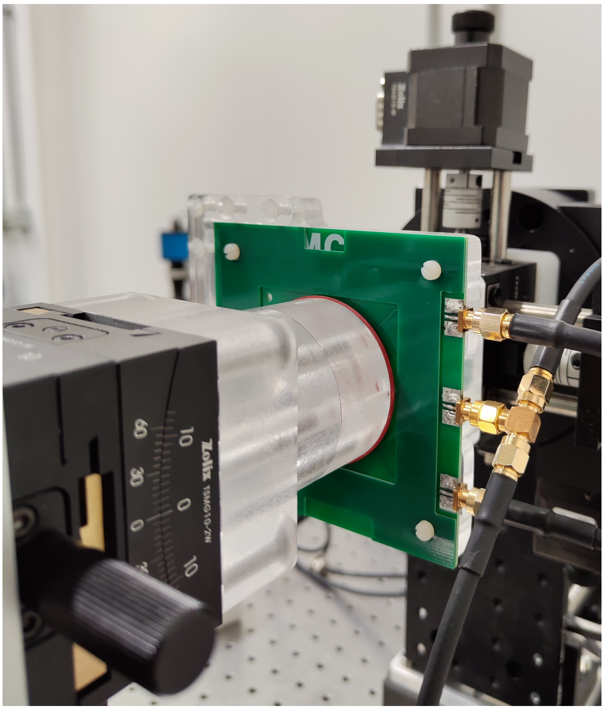

Figure 3.17: *Measurement setup for an absolute rotary IPS with rectangular coils.*

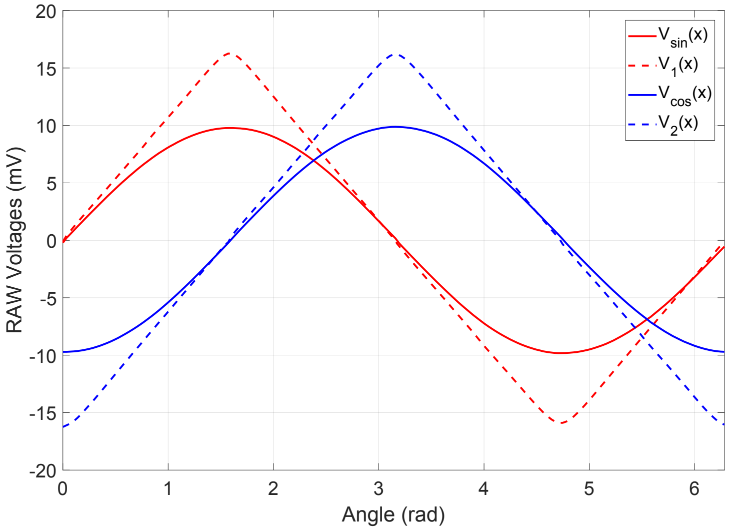

Figure 3.18: *Comparison between the induced voltages for the sinusoidal and rectangular receivers shape coupled with a rectangular target.*

CHAPTER 4

Towards digital twin

Often, users wish to determine if, within a predefined space, there exist sensor configurations with varying characteristics in terms of linearity errors. It can be very useful to have a tool that provides insights into which sensor type to consider even before conducting a full simulation. To address this need, we have developed a straightforward surrogate model for a rotary IPS that mimics the behaviour of the simulator.

Moreover, this manuscript introduces for the first time its capability to detect deviations from the standard operational range. Notably, the signals acquired from the IPS receivers exhibit sensitivity to shaft misalignment issues, including off-axis and tilt.

In this chapter, we present a machine learning tool based on the random forest algorithm to detect these misalignments.

4.1 Space exploration for Decision Support

In the engineering practice, it frequently occurs that designers, final or intermediate users have to roughly estimate some basic performance or specification data on the basis of input data available at the moment. The common practice in many companies relies in the knowledge of experts which has the capability to identify the performance of a product give certain specifics. Another approach to do this is to investigate by means of simulation tools directly the performances. There is nothing wrong with these approaches but they are time consuming. Recently effort has been put in the investigation of the performances based on the input parameters by means of software which can support the users during the choice of a product. An effective tool which can facilitate decision making is the DSS.

The DSS provides a data-driven approach to engineering design processes, which can save time. By using machine learning algorithms, the DSS can quickly estimate performance or specification data, and it can be extended to other fields where the current design practice needs improvements. The DSS also allows for the preservation of a company's knowledge over time and the possibility to have the models on request at any time [89].

The first step toward the DSS is the building of a surrogate model or also know as metamodel. A surrogate model is a simplified model that is used to approximate the behaviour of a more complex model. In the context of engineering design, surrogate models are often used to replace computationally expensive simulations with faster and simpler models that can be used for optimization or other tasks. Surrogate models are typically created using machine learning algorithms, which learn to map inputs to outputs based on a set of training data. Once the surrogate model is trained, it can be used to predict the output of the more complex model for new inputs. Surrogate models can be used to speed up the design process, reduce the cost of simulations, and enable more efficient optimization. Through the years it has become clear that metamodeling provides a decision support role for design engineers. To make an example of the importance of having a metamodel, it is reported that it takes Ford Motor Company about 36-160 hrs to run one crash simulation [54].

A list of areas where the metamodeling can play a role was provided in [105]. Among different areas the Design space exploration was particularly interesting for our purposes. The design space is explored to enhance the engineers' understanding of the design problem by working on a cheap-to-run metamodel.

4.1.1 Application to Inductive position sensors

As far as the IPSs is concerned, users wish to determine if, within a predefined space, there exist sensor configurations with low linearity errors. Here low linearity error means w.r.t. the necessity of the user. It should be noted here that not always the users have the possibility to optimize the receivers coils. It can be very useful to have a tool that provides insights into which sensor type to consider even before conducting a full simulation. To address this need, we have developed a straightforward surrogate model for a rotary IPS that mimics the behaviour of the simulator.

The input parameters for this model are geometric variables, such as TX radius (min and max), RX radius (min and max), Target radius (min and max), while the output parameter is the maximum linearity error. By defining the level set of the linearity error as

$$S_\epsilon = \{\mathbf{x} \in \mathbb{R}^n | f(\mathbf{x}) \leq \epsilon\},$$

we can determine the bounding box of these parameters which can be useful to for the operator in the decisional state of the sensor to consider for future application.

4.1.2 Data Description

To build a surrogate model we have to create a dataset so that a map input (feature space)-output(labels) is created. In general we don't know the relations that exists between these quantities. The model will do that for us. The approach of training a model with label is called *supervised learning*.

Supervised learning can be divided into regression and classification problems. Whereas the outputs for classification are discrete class labels, regression is concerned with the prediction of continuous quantities.

The training data comes in pairs of inputs (x, y), where $x \in \mathbb{R}^d$ is the input instance, and y is its label. The entire training data is denoted as:

$$D = \{(x_1, y_1), \ldots, (x_n, y_n)\} \subseteq \mathbb{R}^d \times \mathcal{C}$$

where:

$\mathbb{R}^d$ is the d-dimensional feature space, x_i is the input vector of the i-th sample, y_i is the label of the i-th sample, and $\mathcal{C}$ is the label space.

The dataset used in this study, comprise 18,382 samples in the training set and 4,596 samples in the test set, all obtained through simulations performed solving the eddy current problem described in the first chapter. The input features and their corresponding intervals are summarized in Table 4.1. The choice of the intervals depends on the user needs whereas the output variable which set the performance is the linearity error. Obviously, the model we would build is a regression model being the output a real variable.

For the dataset sampling the Sobol strategy was used. It provides a sequence of points that very uniformly fill the multi-dimensional cube

Table 4.1: *Input Features and Intervals*

Input Feature	Min Value (mm)	Max Value (mm)
Maximum radius TX	32	36
Minimum radius Target	24	28
Maximum radius Target	30	36
Minimum radius RX	26	28
Maximum radius RX	29	34.5

where the distribution of the sampling points tends to concentrates in specific regions due to the curse of dimensionality [95].

4.1.3 Building the model using Gaussian Processes

Gaussian Processs (GPs) [1] represent a category of statistical models enabling the formulation of a probability distribution over stochastic functions. Rather than explicitly specifying a mathematical function governing the generation of observed data, GPs capture the covariance relationships between pairs of data points within the process. This modelling approach incorporates our domain expertise and available data, which might seem abstract but finds diverse applications, including the modelling of stochastic physical phenomena, as well as high-dimensional interpolation and smoothing. Indeed they have several advantages:

1) their prediction interpolates the observations. Useful when the model should generalize well the input data.
2) the prediction is probabilistic, typically following a Gaussian distribution. This allows for the computation of empirical confidence intervals, enabling decisions regarding whether to refit the model (online fitting or adaptive fitting) in specific regions of interest.
3) the method allows the specification of different kernels.

We start from considering the Gaussian distribution. A Gaussian random variable $X \sim \mathcal{N}(\mu, \Sigma)$, where μ represents the mean and Σ is the covariance matrix, follows the probability density function given by:

$$P(x; \mu, \Sigma) = \frac{1}{(2\pi)^{d/2}|\Sigma|} \exp\left(-\frac{1}{2}(x-\mu)^\top \Sigma^{-1}(x-\mu)\right)$$

where $|\Sigma|$ denotes the determinant of the covariance matrix Σ. The Gaussian distribution has some nice properties. Considering $y = [y_A, y_B]$

---

[1] Also referred to Kriging method

a Gaussian random variable, with mean $\mu = [\mu_A, \mu_B]$, and covariance matrix $\Sigma = \begin{bmatrix} \Sigma_{AA} & \Sigma_{AB} \\ \Sigma_{BA} & \Sigma_{BB} \end{bmatrix}$.

- Normalization: $\int p(y;\mu,\Sigma)\,dy = 1$
- Marginalization: The marginal distributions $p(y_A) = \int p(y_A, y_B; \mu, \Sigma)\,dy_B$ and $p(y_B) = \int p(y_A, y_B; \mu, \Sigma)\,dy_A$ are Gaussian:

$$y_A \sim \mathcal{N}(\mu_A, \Sigma_{AA})$$
$$y_B \sim \mathcal{N}(\mu_B, \Sigma_{BB})$$

- Summation: If $y \sim \mathcal{N}(\mu, \Sigma)$ and $y' \sim \mathcal{N}(\mu', \Sigma')$, then $y + y' \sim \mathcal{N}(\mu + \mu', \Sigma + \Sigma')$.
- Conditioning: The conditional distribution of y_A on y_B:

$$p(y_A|y_B) = \frac{p(y_A, y_B; \mu, \Sigma)}{\int p(y_A, y_B; \mu, \Sigma)\,dy_A},$$

  is also Gaussian:

$$y_A|y_B = y_B \sim \mathcal{N}\left(\mu_A + \Sigma_{AB}\Sigma_{BB}^{-1}(y_B - \mu_B), \Sigma_{AA} - \Sigma_{AB}\Sigma_{BB}^{-1}\Sigma_{BA}\right).$$

Now the idea is to use these properties to build a model such that the complicated function which represent the map between the data and the output is a multivariate Gaussian distribution

$$f \sim G(\mu(\boldsymbol{x}), k(\boldsymbol{x}, \boldsymbol{x}')).$$

It can be thought about the function as a random variable with a mean and a variance but in the case the mean is not a number but instead a functions. Sometimes is also called trend.

In practice, the labels $f(\boldsymbol{x})$ determine the heights of the functions whereas the most difficult task is finding the relations between the $\boldsymbol{x}$ and his neighbours. This is the task of the covariance function $k(\boldsymbol{x}, \boldsymbol{x}')$ and this is the heart of the GPs. One popular and powerful covariance function is theRadial Basis Function (RBF) with different length scales for each feature dimension. Fig. 4.1 shows an example of the functions living in GP (a priori) and the functions constrain from the dataset (a posteriori) [85]. In this case the function we want to model, given the data (black dots in the figure), is $f(x) = \sin(x) + \sin(2x)$ when the samples are computed in $x = [-4, -3, -2.5, -1.5, -1, -0.5, 1.2, 1.3, 2, 3.4, 4$. The dashed black line is the mean function $\mu(x)$ whereas the dashed red line is the real function.

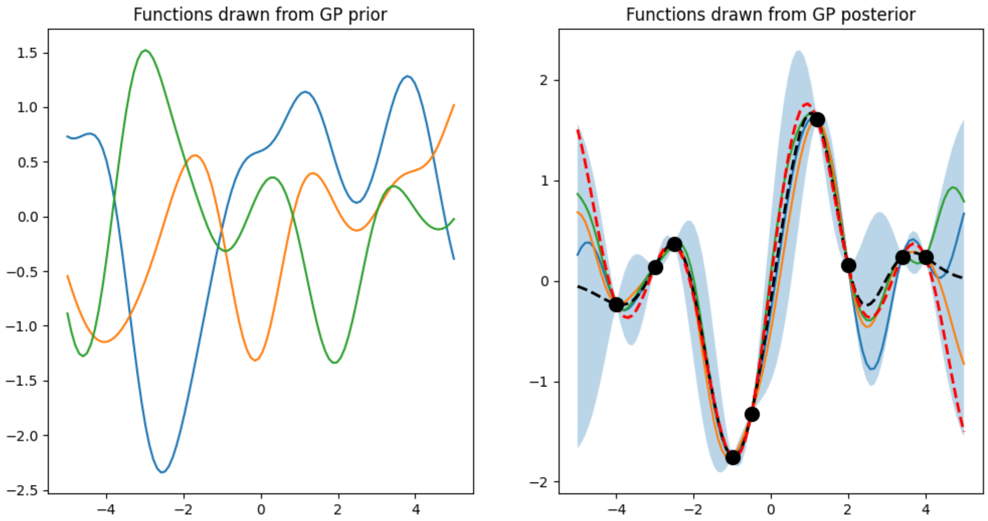

Figure 4.1: *A priori (on the left) functions picked from the GP and a posteriori (on the right) functions picked from the GP modelling a function* $f(x) = \sin(x) + \sin(2x)$.

4.1.4 Methodology

The training of our model is made easier with the use of the versatile machine learning library such as `scikit-learn`. Within the package, build in functions are already available and also several numbers of kernels.

By taking advantage of the library's extensive features, we've made the training process more efficient and carefully fine-tuned the model's settings to ensure it works well with our dataset.

We outline the training setup in Table 4.2.

Table 4.2: *Parameters of Gaussian Process Regressor*

Parameter	**Value**
Kernel	RBF
Length Scale	1.0
Length Scale Bounds	$(1 \times 10^{-2}, 1 \times 10^{2})$
n_restarts_optimizer	9

4.1.5 Results

The maximum linearity error ranges from 0 to 4%. The primary metric used for evaluation was the Root Mean Square Error (RMSE), calculated

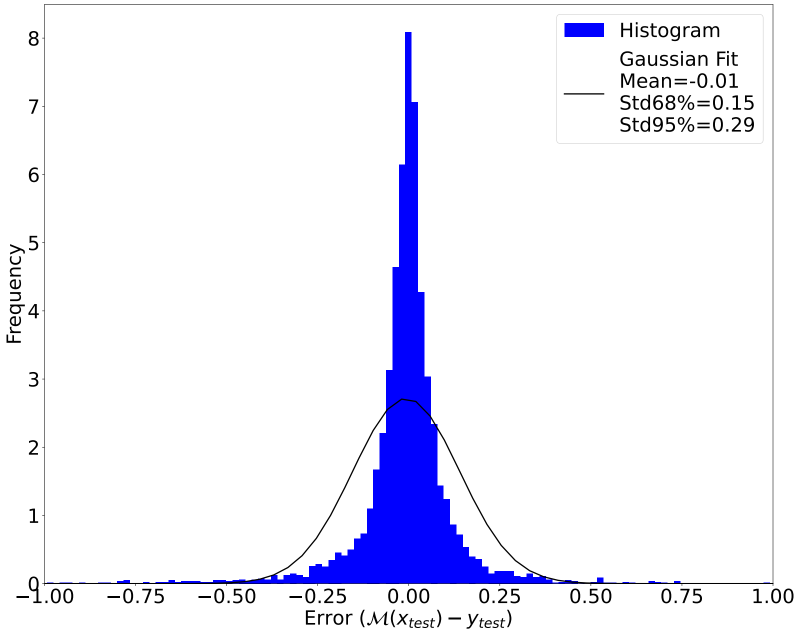

Figure 4.2: *Gaussian Process Performance*

as

$$RMSE = \sqrt{\frac{\sum_{i=1}^{N}(\mathcal{M}(x_i) - \hat{y}(x_i))^2}{N}}. \tag{4.1}$$

This metric showed a value of approximately 0.15 which is the error of the predicted linearity error from the actual one. Fig. 4.2 illustrates the error distribution on the test set. The distribution indicates that the error clusters around the true values. In the majority of cases, the error remains within 10% of the actual values. Specifically, with a 95% confidence level, the error does not exceed 7.5% in most instances.

These results establish the reliability of our model's predictions, making it a valuable tool for applications like quality assurance and optimizing sensor design and placement. Furthermore the model also allows users to have a tool which can predict a large dataset in very short time. A simulation takes approximately 40 seconds whereas with the model the values of 10000 samples are obtained in seconds. Once a user have the performance parameters can easily choose to select the level set of the sensors which has linearity error below a certain threshold and finally decide the right geometry to adopt for further development.

4.2 Misalignments detection

The utilization of non-invasive techniques for data acquisition in automatic timely scheduling of the maintenance and predicting failure aspects of dynamic machines holds a great scope in future [32]. To this end, different works provide solutions based on vibrations (or acoustic) analysis performed using accelerometers or inductive proximity sensors [67, 94]. In particular, in [94] a comparison between the vibration sensors and the proximity sensors has shown that the later tends to provide better diagnosis informations. Moreover, they claim that high frequency components are difficult to detect accurately as far as the proximity sensors are adopted. This is inherently related to the operation principle of the sensor which measures displacements. Hence, even shaft surface movements affect negatively the measurement. In order to improve the accuracy of the model using these sensors, information fusion algorithms are used [99].

What we want to show in this manuscript is that it is possible to achieve predictive maintenance by using as a key component IPSs. Till now this sensors has been used for the measurement of the position rotation. Yet, in many works is claimed that the measurements on the linearity error, which is a key performance parameter of the sensor, are affected by the misalignments between the rotor part and the stator part. If in the one hand this is a problem in the context of the position sensing, on the other hand it suggests that the sensor can be used for novel purposes such the detection of anomalies within the system. A theoretical motivation was previously given in [60], where emphasis was given to the relation between the trajectory and the area-of-overlap functions. These functions are directly related to the output response of the sensor. Whenever the trajectory followed by the rotor deviates from the ideal one the area-of-overlap functions will also deviate from the ideal one.

In this work we exploit this feature to develop a digital model representing the shaft of a rotating machine. First we perform a set of simulations with several anomalies which might affect the operating region of the shaft. Then, we build an inverse regression model which has as input the observations obtained from the simulations and as output the anomalies that has generated those observations. To build the digital twin we use the Random Forest (RF) regressor. Finally, we show the potential of the method by means of measurements performed on a rotary IPS.

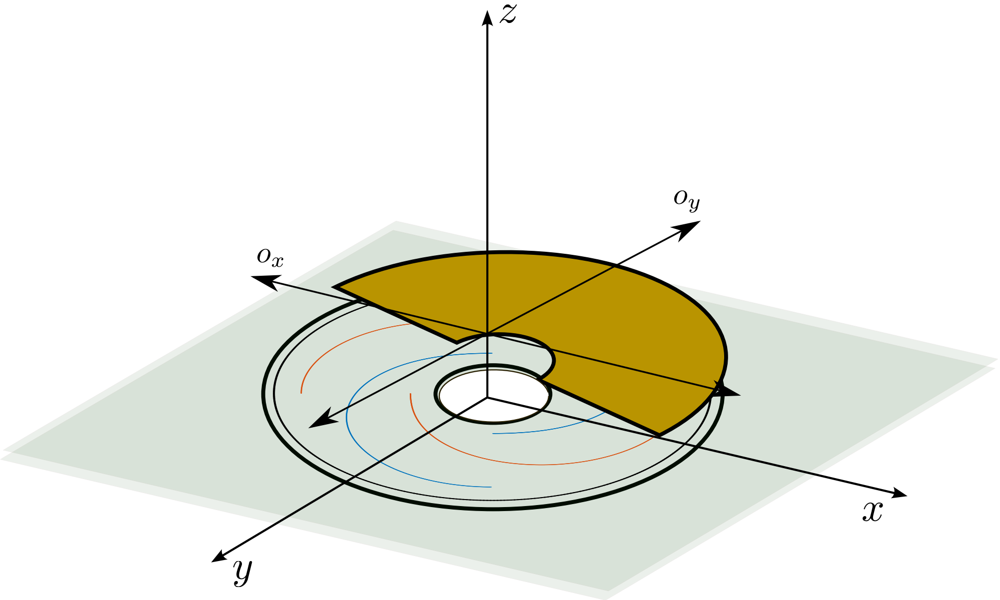

Figure 4.3: *Definition of the off-axis along x-axis and y-axis.*

4.2.1 Misalignments types

In the following we will refer to the target as rotor, which will be attached to the shaft, whereas as far as the the sensing part is concerned, containing the receivers and the transmitter, as stator.

Several types of mechanical misalignments has been identified as far as the IPSs is concerned. When using the IPS as a position sensor the investigation of these non-idealities is important because compensation techniques are applied in order to improve the linearity of the sensor. A list of these non-idealities is provided in the following.

1) A rigid rotation of the system rotor-shaft w.r.t. the stator defines the *tilt*

2) A rigid translation of the system rotor-shaft w.r.t. the stator defines the *off axis*

3) A rigid translation of the rotor w.r.t. the stator along the z axis defines the *air gap*.

To understand how the aforementioned non-idealities act on the induced voltages, a set of simulations has been performed considering one effect at time. Instead of showing the induced voltages of the sensor with and without misalignments, Fig. 4.5 depict the pointwise difference between these signals. This is a compact representation of the discrepancies and furthermore it provides useful insights about the effect

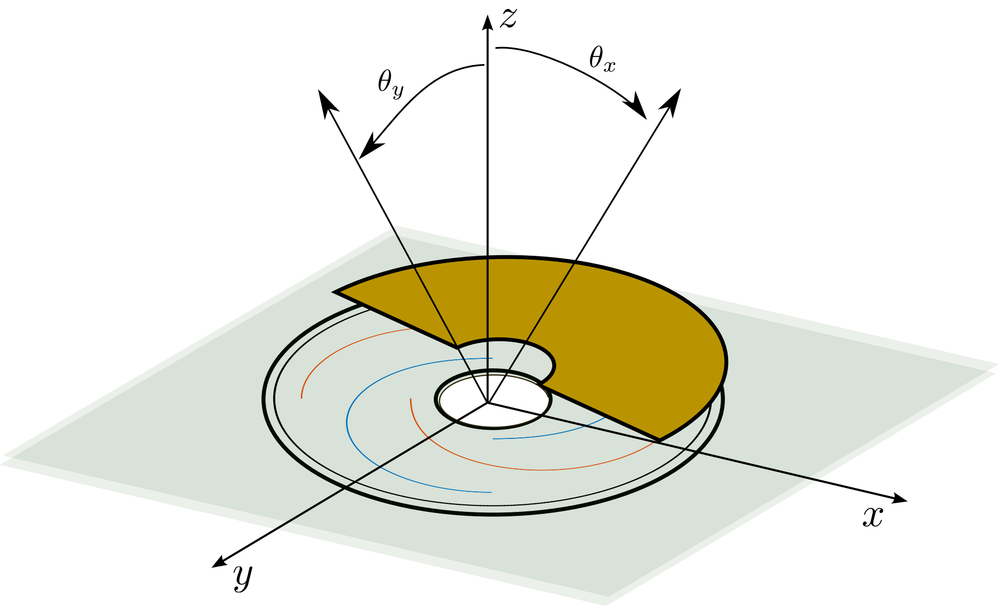

Figure 4.4: *Definition of the tilt along x-axis and y-axis.*

of each misalignment. The figure shows also the geometry of the sensor with the transformations discussed above which cause that particular error. These quantities are projected on the plane as a parametrization of the θ angle i.e. $[\Delta V_{cos}(\theta), \Delta V_{sin}(\theta)]$. Observing the graphics of these discrepancies some interesting rule of thumb can be extracted.

First, the air gap has always the effect of reducing the amplitude of the received signal as far as the distance between the target PCB increases. Indeed, the intensity of the eddy current generated inside the target decreases as the distance from the transmitter increases.

Second, the off-axis and the tilt results in an asymmetric distortion of the received signal. As far as the off-axis is concerned, being the rotor parallel to the stator the induced voltages cannot increase more than the maximum value allowed for that specific air gap. When an off-axis is applied, it can only be reduced since a portion of the receiver remains uncovered. Regarding the tilt, having the rotor an angular misalignment it will cover more a portion of the stator but less the other one during the revolution of the shaft. The signals increased in one region will decrease on the other one as a compensation effect. They can be associated in literature with the static eccentricity since the minimum radius of the rotor above the stator is fixed.

These misalignments can be associated in literature with the dynamic eccentricity since the minimum radius of the rotor above the stator rotates with the rotor during the revolution. Based on the [3,29] we

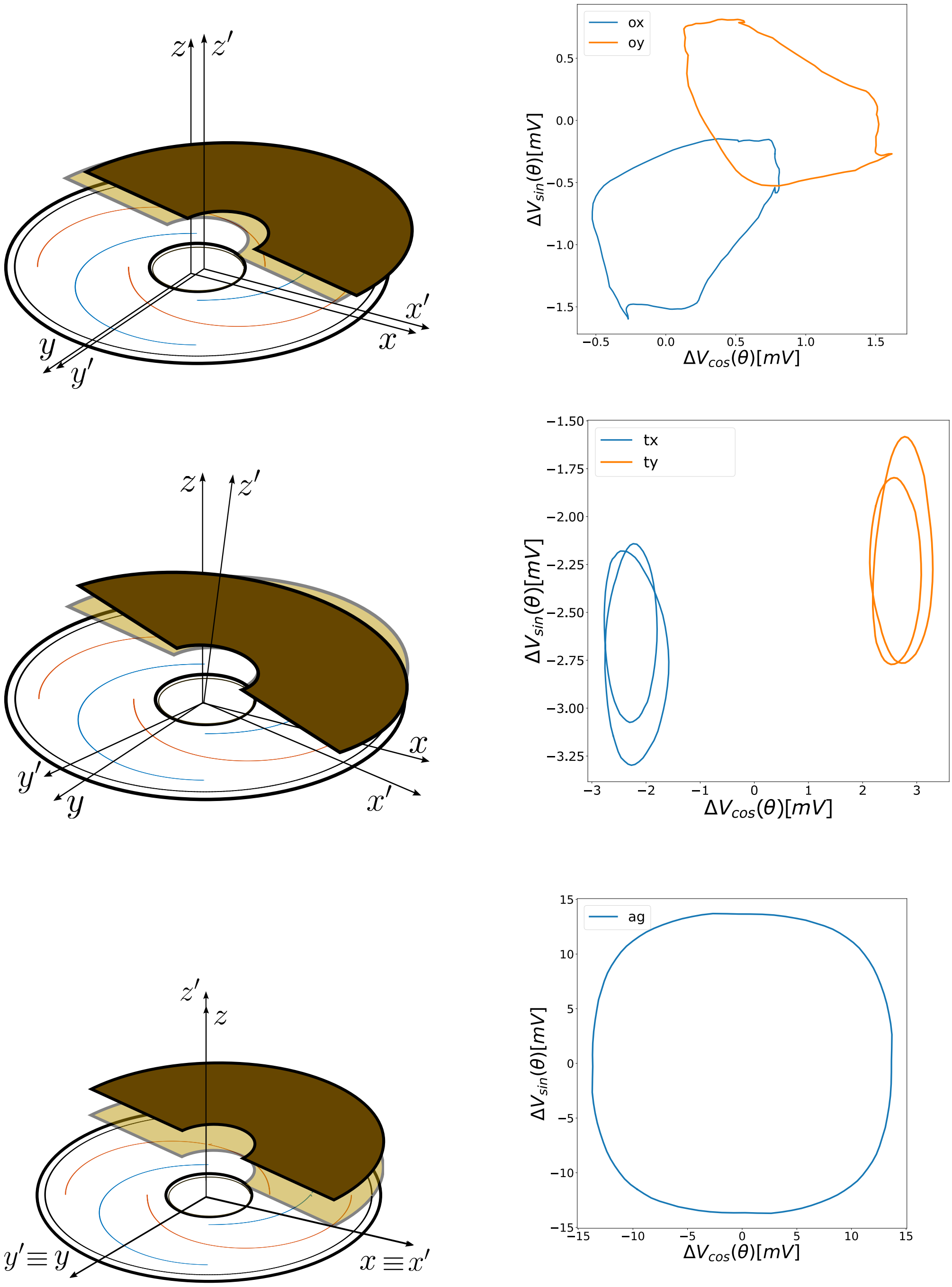

Figure 4.5: *The misalignment on the left and the 2D error plot of the induced voltages w.r.t. an ideal reference. From top to bottom; off-axis, tilt, air-gap.*

can identify the aforementioned anomalies acting on our sensor as:

- multivariate: since we are considering five different mixed anomalies
- collective: since they can act on the overall system at the same time
- temporal: since the observations are only time dependent

The normal operation condition is when the rotor follows the ideal trajectory which generates on the receivers the desired responses. In our case the ideal responses of the rotary IPS must be sinusoidal functions.

Given these information we want to develop a method to identify the misalignment of the shaft where the sensor is mounted. To achieve this we develop a machine learning tool based on RF for regression purposes which given in input the induced voltages signals on both receivers is able to identify the anomaly and give insight in the position of the rotor shaft.

In our view this work represent a first step towards the concept of digital twin of the shaft using the IPS.

4.2.2 Decision Tree

There exist several straightforward yet effective models that partition the input space into cuboidal regions, with edges aligned to the axes. Each region is then assigned a simple model, such as a constant. These models can be seen as a method of combining models where only one model is responsible for making predictions at any given point in the input space. The selection of a specific model for a new input x can be described as a sequential decision-making process that corresponds to traversing a binary tree (a tree that splits into two branches at each node).

Fig. 4.6 illustrates a recursive binary partitioning of the input space and its corresponding tree structure. In this example, the first step divides the entire input space into two regions based on whether $x_1 < \theta_1$ or $x_1 > \theta_1$, where θ_1 is a model parameter. This creates two subregions, each of which can be further subdivided independently. For instance, the region $x_1 < \theta_1$ is further divided based on whether $x_2 < \theta_2$ or $x_2 > \theta_2$, resulting in regions A and B.

The recursive subdivision can be described by traversing the binary tree depicted always in Fig. 4.6 . For any new input x, we determine its region by starting at the root node of the tree and following a path down to a specific leaf node based on the decision criteria at each node. It's

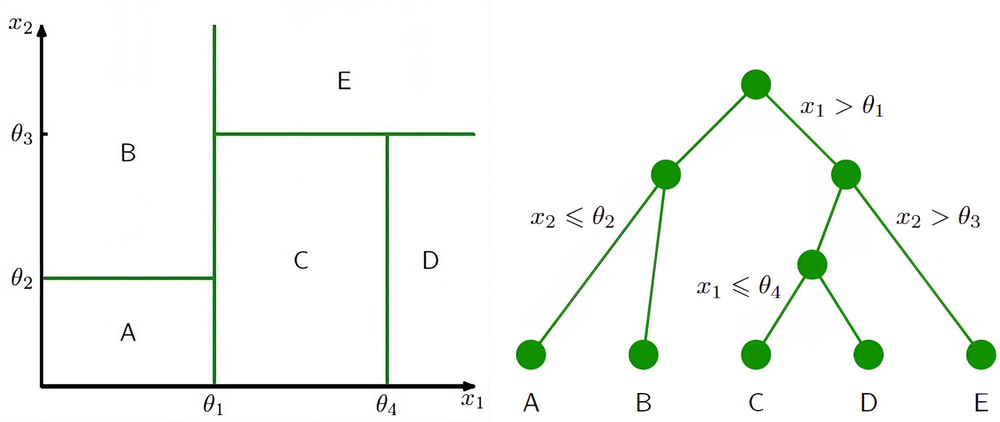

Figure 4.6: *Partition of the domain and the related decision tree [21].*

important to note that these decision trees are not probabilistic graphical models.

A key feature of tree-based models, which makes them popular in fields like medical diagnosis, is their interpretability. They correspond to a sequence of binary decisions applied to individual input variables, making them easily understandable by humans. For example, to predict a patient's disease, we might first ask if their temperature is above a certain threshold. If yes, we might then ask if their blood pressure is below another threshold. Each leaf of the tree corresponds to a specific diagnosis.

To learn such a model from training data, we need to determine the tree's structure, including which input variable forms the split criterion at each node and the value of the threshold parameter θ_i for the split. We also need to determine the values of the predictive variable within each region. This process is called *tree growing* and is a crucial part of decision tree algorithms in machine learning. It involves selecting questions or conditions to split the data. This process continues recursively until a stopping criterion is met, such as reaching a maximum depth or a minimum number of samples per leaf. The goal is to create branches that lead to terminal nodes (leaves) that are as pure as possible, meaning they contain predominantly samples from one class.

Considering a classification problem where we aim to predict a single target variable t from a D-dimensional vector $x = (x_1, ..., x_D)^T$ of input variables. The training data consists of input vectors $\{x_1, ..., x_N\}$ and corresponding continuous labels $\{t_1, ..., t_N\}$. Even with a fixed number of nodes in the tree, finding the optimal structure (including the choice of input variable for each split and the corresponding thresholds) to minimize the RMSE is usually computationally infeasible due to the large number of possible solutions. Instead, a greedy optimization is typically used, starting with a single root node that corresponds to the entire input space and then growing the tree by adding nodes one at a time.

At each step, there will be several candidate regions in the input space that can be split, corresponding to adding a pair of leaf nodes to the existing tree. For each of these, there is a choice of which of the D input variables to split, as well as the value of the threshold. The joint optimization of the choice of region to split and the choice of input variable and threshold can be done efficiently by exhaustive search. Notably, for a given choice of split variable and threshold, the optimal choice of predictive variable is given by the local average of the data, as noted earlier. This process is repeated for all possible choices of variable to be split, and the one that results in the smallest residual sum-of-squares error is retained.

However, there are some problems with tree-based methods like classification and regression trees (CART). While their interpretability is often seen as a major strength, in practice they are good but not great predictors very sensitive to the details of the dataset [26].

There are other issues with tree-based methods considered in this section. One is that splits are aligned with the axes of the feature space, which may be suboptimal. For example, separating two classes whose optimal decision boundary runs at 45 degrees to the axes would require many axis-parallel splits compared to a single non-axis-aligned split.

Furthermore, decision tree splits are hard, meaning each region of input space is associated with one and only one leaf node model. This issue becomes particularly problematic in regression where we typically aim to model smooth functions, but tree models produce piecewise-constant predictions with discontinuities at split boundaries.

4.2.3 Random Forest

We have seen that standard decision trees are restricted to axis-aligned splits of the input space. These constraints can be relaxed, at the expense of interpretability, by allowing soft, probabilistic splits that can be functions of all of the input variables, not just one of them at a time. If we also give the leaf models a probabilistic interpretation, we arrive at a fully probabilistic tree-based model called the hierarchical mixture of experts

RFs are a combination of tree predictors such that each tree depends on the values of a random vector sampled independently and with the same distribution for all trees in the forest [25].

A new data point is classified by passing it through each of the trees, averaging over the resulting terminal distributions, and taking the mode of this aggregate distribution. Due to averaging and weak dependence, significant errors in these estimates can be tolerated.

Furthermore, since the processes of tree-growing and parameter estimation can be separated, these estimates can be refined indefinitely without the need to reconstruct the trees. This refinement is achieved simply by updating a counter in each tree for each new data point.

The separation between tree construction and parameter estimation, along with the possibility of using different training samples for each phase, opens up opportunities for tree-growing based on either unlabeled samples (i.e., unsupervised learning) or samples from only some of the shape classes. Both of these methods perform surprisingly well compared to traditional supervised learning [8].

To see why an ensamble of trees work better than a single tree we start from considering the bias-variance decomposition computed on an entire dataset A. Let the model $\mathcal{M}$ be a random variable with distribution $\mathcal{P}$. The variance bias decomposition writes:

$$\begin{aligned} E\left[(\mathcal{M}_A(x) - y(x))^2\right] = {} & E\left[(\mathcal{M}_A(x) - \bar{\mathcal{M}}(x))^2\right] \text{ Variance} \\ & + E\left[(\bar{\mathcal{M}}(x) - \bar{y}(x))^2\right] \text{ Bias} \\ & + E\left[(\bar{y}(x) - y(x))^2\right] \text{ Noise} \end{aligned}$$

where $y(x)$ is the real label, the $\mathcal{M}_A(x)$ the estimate label, $\bar{\mathcal{M}}(x))$ is the mean classifier and $y(x)$ the mean label.

Our primary aim remains reducing the variance component:

$$E\left[(\mathcal{M}_A(x) - \bar{\mathcal{M}}(x))^2\right]$$

To achieve this, we aspire to converge individual functions $\mathcal{M}_A$ toward a common function $\bar{\mathcal{M}}$. One way to address this challenge is through ensemble learning techniques. The *weak law of large numbers*, which applies to i.i.d. random variables, suggests that when we have N independent classifiers $\mathcal{M}_{A_i}$, the average of their predictions tends to converge to a common prediction:

$$\hat{\mathcal{M}} = \frac{1}{N} \sum_{i=1}^{N} \mathcal{M}_{A_i} \rightarrow \bar{\mathcal{M}} \text{ as } m \rightarrow \infty$$

This ensemble of classifiers is often referred to as an *ensemble*. So the idea to build N models associated to the datasets A_i ($i = 1, \ldots, N$)

should provide benefits in reducing the variance. However, a practical challenge arises: we often do not have access to multiple datasets $A_1, \dots, A_N$, but we only have the single dataset A. To address this challenge the concept of *Bagging (Bootstrap Aggregating)* is introduced.

The bagging consist in simulating selections from the distribution $\mathcal{P}$, by performing sampling with replacement from the same dataset A. We define a probability distribution over the dataset A as $Q(X, Y|A)$ that selects a training sample (x_i, y_i) from A uniformly at random:

$$Q((x_i, y_i)|A) = \frac{1}{n} \quad \text{for all } (x_i, y_i) \in A \text{ with } n = |A|$$

which means that all the samples has the same probability to be picked.

Then multiple datasets A_i are created by sampling from the new defined probability density Q, where $|A_i|$ has the same size of A and each A_i is selected with replacement from A. The bagged classifier is defined as follows:

$$\mathcal{M}_A = \frac{1}{N} \sum_{i=1}^{N} \mathcal{M}_{A_i}$$

It's important to note that $\mathcal{M}_A$ does not necessarily converge to $\bar{\mathcal{M}}$ because we are under the assumption that $\mathcal{M}(A_i)$ and $\mathcal{M}(A_j)$ are independent. Nevertheless, in practice, bagging effectively reduces variance.

Although is not possible to prove that the new samples are i.i.d., it is possible to show that they are selected from the original distribution $\mathcal{P}$ with the assumption that the dataset is large.

In summary, Bagging involves the following steps:

- Sample N datasets $A_1, \dots, A_N$ from A with replacement.
- Train a classifier $\mathcal{M}_i(x)$ on each A_i.
- The final classifier is defined as $\mathcal{M}(x) = \frac{1}{N} \sum_{j=1}^{N} \mathcal{M}_j(x)$.

In practice, a larger value of N generally leads to a more effective ensemble, but there are diminishing returns. Setting N excessively high may result in slower computation without significant improvements in function performance.

4.2.4 Random forest for misalignment identification

For the development of our model, we employed the VSCode environment and the scikit-learn Machine Learning package in Python. Specifically, we utilized the *sklearn.ensemble module*, which includes averaging

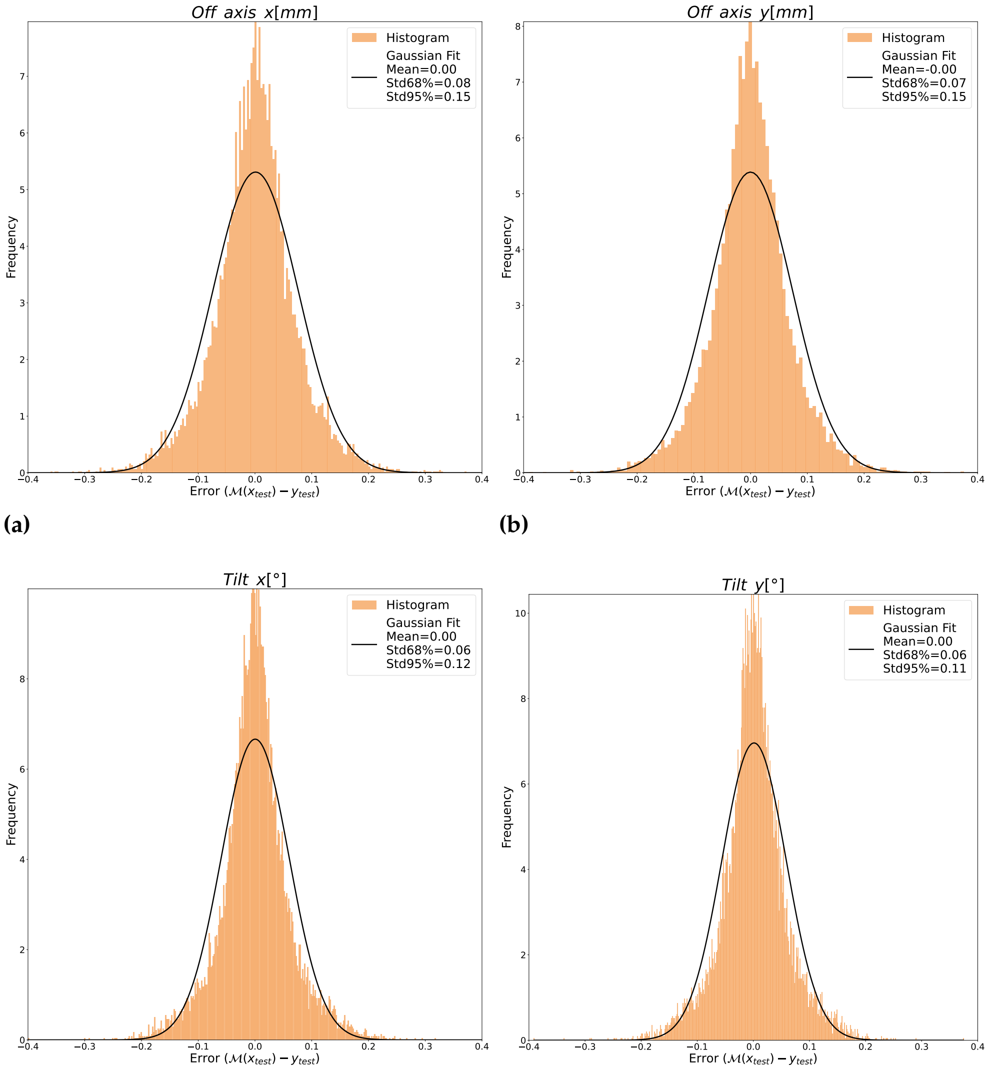

(a) **(b)**

(c) **(d)**

Figure 4.7

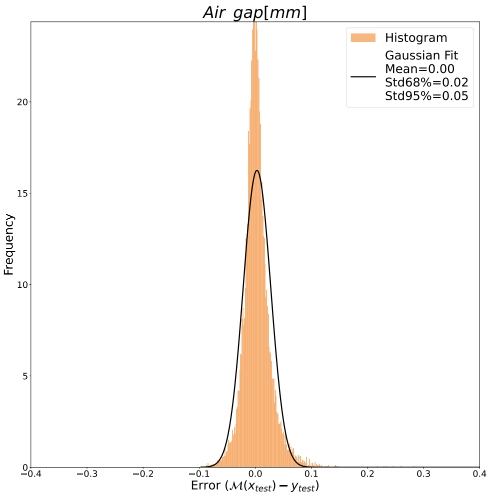

(e)

Figure 4.7: *Distribution of the predicted error from the RF model and the gaussian fitting curve with the relative standard deviation. (4.7a) air gap error; (4.7b) error of off-axis along x direction; (4.7c) error of off-axis along y direction (4.7d) error of tilt along x direction; (4.7e) error of tilt along y direction.*

algorithms based on randomized decision trees, such as the RF algorithm.

Given that we have the ability to provide synthetic data obtained from our solver we want to use a supervised learning model to predict the misalignments. Exploiting the speed of the in-house solver, 20000 data can be obtained in less than 24 hours. 10 cores are used in parallel for the simulations executed on a workstation with 32GB of RAM equipped with Intel Core i7 with base clock frequency of 3.6GHz per core.

The learning process for the RF model was carried out on a high-performance computing system equipped with an AMD Ryzen Threadripper PRO 3975WX CPU. This CPU boasts 32 cores, 256 GB of RAM, and operates at a base frequency of 3.49 GHz, providing significant computational power for machine learning tasks.

The misalignments are uniformly sampled from a predefined 5 dimensional hyper-rectangle which feeds the simulator. Table 4.3 shows the ranges of the hyper-rectangle. For each simulation we obtain the outputs which are the samples of the induced voltages, 101 for the sine receiver and 101 for the cosine receiver. The Fast Fast Fourier Transform (FFT) is then applied to the received signals, where we take only the first 100 points. The reason why we adopt this representation is that the

Table 4.3: *Simulated misalignments*

Misalignent type	Range
off-axis x	[-2, 2] mm
off-axis y	[-2, 2] mm
tilt x	[-1°, 1°]
tilt y	[-1°, 1°]
air gap	[0, 3] mm

low frequency signals are responsible for the misalignments, whereas the high frequency signals shows the typical behaviour of bearing fault The real and the imaginary part of the FFT for each receiver becomes the input of the machine learning model, where the output are the corresponding misalignments that we want to predict.

It is important to note that the data collected for this model was obtained through a simulator, which provides clean and accurate data. Actually, the measured data are noisy which can make the prediction of the model difficult. We first apply a preprocessing step when the data is cleaned with moving average filter. The purpose of this preprocessing step is to make the measured data more representative of the actual data with which the model was trained.

For the validation of the model 20% of the dataset is left out from the training set and the root mean square error (RMSE) of the model is computed. Table 4.4 and Fig. 4.7 shows the predictive performance of the model.

Table 4.4: *RMSE Errors for RF model.*

Variable	RMSE Error
Airgap	0.027 [mm]
Off-axis x	0.076 [mm]
Off-axis y	0.075 [mm]
Tilt-x	0.067 [°]
Tilt-y	0.065 [°]

In particular Fig. 4.7 shows that, in 95% of the cases, the distribution of the error for each non-ideality provides the following relative errors

- below 4%FS for the Off-axis,
- below 6%FS for the Tilt,
- below 2%FS for the Air Gap.

The next section will provide some measurements in order to test this model and whether his performance can provide insights about the misalignments.

4.3 Data Collection and Measurement Setup

To assess the model's performance, we conducted a series of measurements adopting a measurement setup similar to those shown in the previous chapters. During this measurement session, we adopted the Renesas/IDT Inductive Position Sensor Integrated Circuit (IPS2550), which offers a high-speed analog interface, providing positional information in the form of demodulated analog sine/cosine raw data obtained from the receiver coils. The IPS2550 incorporates a local oscillator (LO) that excites the transmitting coil at the user's specified frequency using an external capacitor; in our case, this frequency was set to 3.4 MHz. The input stage of the system involves a mixer, which multiplies the LO signal with the received signal, followed by a low-pass filter to extract the envelope of the received signal, which is then used as input data for our model. Having trained the model with only one period per anomaly, from each received signal, a preprocessing stage takes care in collecting properly each measured period.

Before starting the test, we first identify the maximum induced voltages on the receivers. It consists in placing the metallic target above the receivers, touching the PCB resist. Subsequently, rotating it at 90° covering each of the 4 areas of the receivers. The maximum induced voltage was saved and used to correctly normalize the measured induced voltages, as described in (4.3).

The test consist in centring the target as accurately as possible and subsequently induce different displacement that emulate different shaft misalignment such as off-axis along the x and y axis and a tilt in the x and y axes. Table 4.5 shows the sequence of the displacements we perform on the target. Since we don't have knowledge a priori of the anomalies affecting the "centered" target the table shows displacement w.r.t. an unknown value. Subsequently, we apply the delta displacements.

For each movement we collect approximately 15 periods of the sine and cosine receivers. Periods which contains wrong or incomplete values, for instance the first and the last period corresponding to the phases when the stepper motor accelerate and decelerate, are removed from the dataset. Fig. 4.8 depicts an example of the received signals while the stepper motor, which simulates a shaft, performs multiple rotations around its axis.

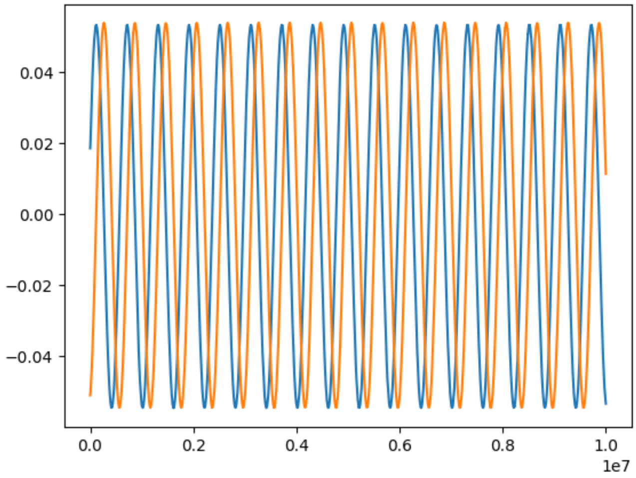

Figure 4.8: *Example of the output signal obtained from the oscilloscope. The x-axis is the numbers of samples whereas the y-axis is the induced voltage on* RX_{cos} *(Blu) and* RX_{sin}*(Orange)*

Similar to the model training phase, we compute the FFT of each single period, separately, extracting the real and imaginary parts of the first 100 samples which becomes the input of the previously trained RF model.

4.3.1 Calibration of the model

In Chapter 3, we gained valuable insights into the non-ideality of the rotary IPS. Interestingly, it also offers a straightforward solution to make the model work effectively.

The issue at hand is this: we train the model with a variable air gap, but in practice, we place the sensor at a unknown distance that might also be outside the training range. How can the model accurately identify the air gap when the real sensor operates with a current different from the simulated one?

The problem arises from the fact that the model can't identify the air gap unless the training dataset contains the maximum value of the induced voltage. This maximum value corresponds to the position of the target at $z = 0$. Even in this case, automatic identification of the air-gap from the model in practice is very challenging. Eventually one should manually try to identify the correct working region of the model which is not our purpose. Our aim is to automatically identify the operation region without involving the intervention of an operator.

Revisiting Chapter 2, we discussed the distribution of induced volt-

Table 4.5: *Measurement sequence using the stepper motor for the off-axis and a goniometer manually moved.*

Measurement	Air Gap[mm]	Off-Axis X[mm]	Off-Axis Y[mm]	Tilt X[°]	Tilt Y[°]
meas #1	$x_1 + 0.7$	x_2	x_3	x_4	x_5
meas #2	$x_1 + 0.7$	$x_2 + 0.4$	x_3	x_4	x_5
meas #3	$x_1 + 0.7$	$x_2 + 0.8$	x_3	x_4	x_5
meas #4	$x_1 + 0.7$	x_2	x_3	x_4	x_5
meas #5	$x_1 + 0.7$	$x_2 - 0.4$	x_3	x_4	x_5
meas #6	$x_1 + 0.7$	$x_2 - 0.8$	x_3	x_4	x_5
meas #7	$x_1 + 0.7$	x_2	x_3	x_4	x_5
meas #8	$x_1 + 0.7$	x_2	$x_3 + 0.4$	x_4	x_5
meas #9	$x_1 + 0.7$	x_2	$x_3 + 0.8$	x_4	x_5
meas #10	$x_1 + 0.7$	x_2	x_3	x_4	x_5
meas #11	$x_1 + 0.7$	x_2	$x_3 - 0.4$	x_4	x_5
meas #12	$x_1 + 0.7$	x_2	$x_3 - 0.8$	x_4	x_5
meas #13	$x_1 + 0.7$	x_2	x_3	$x_4 + 0.5$	x_5
meas #14	$x_1 + 0.7$	x_2	x_3	$x_4 + 0.5$	$x_5 + 0.5$
meas #15	$x_1 + 0.7$	x_2	x_3	$x_4 - 0.5$	$x_5 - 0.5$
meas #16	$x_1 + 0.7$	x_2	x_3	x_4	$x_5 - 0.5$

ages during the motion of the target above the sensor. We mentioned that the area-of-overlap functions are bounded functions, as indicated by (3.14). In order to achieve the maximum (minimum) value, the target has to cover the area of the maximum (minimum) surface when it moves along the trajectory **x**.

$$-1 \leq \frac{V_{sim}}{V_{sim}^{M}} \leq 1 \tag{4.2}$$

$$-1 \leq \frac{V_{meas}}{V_{meas}^{M}} \leq 1 \tag{4.3}$$

This is crucial for the calibration of the model. We first need to compute the maximum induced voltage in the simulations, V_{sim}^{M}. After that, we have to place the real target above the PCB and find the maximum measured induced voltage, V_{M}^{meas}. This calibration procedure is very easy to perform and as the measurements will show it is robust even though we manually and without the use of precision instruments placed the target above the sensor. Finally, we just have to scale all the induced voltages w.r.t. these quantities so that condition (4.2) and (4.3) are met during the simulation and the measurements.

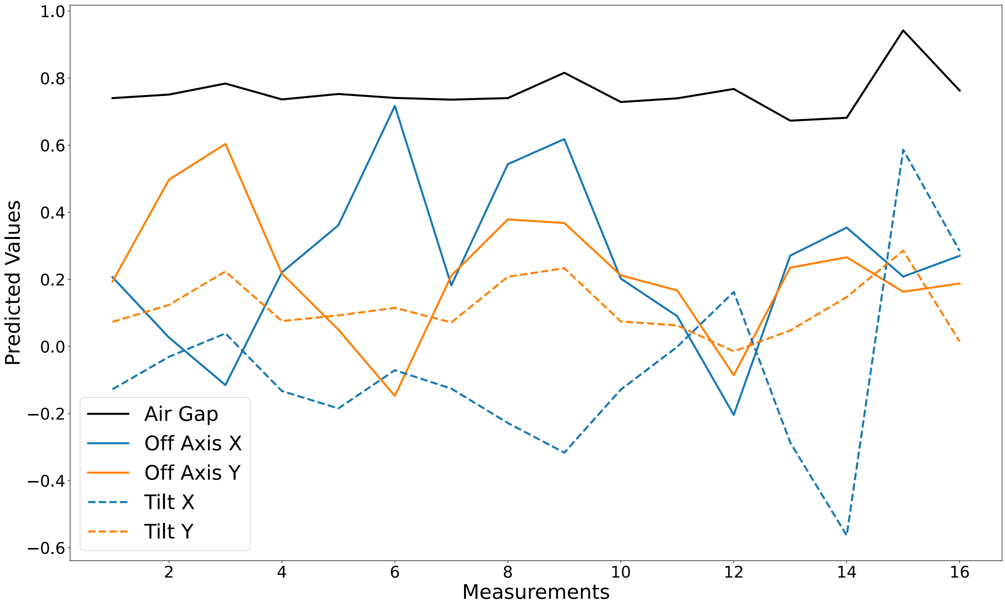

Figure 4.9: *Predicted values of the model for each measurement.*

4.3.2 Discussion

Fig. 4.9 is 1D representation of the displacement predicted from our model.

Firstly, it is possible to observe that the first measure, as expected, presents anomalies such as off-axis and tilt which are not zero in both x and y axis. This is a consequence of the fact that the system isn't centered properly. However, we will consider this measure as a reference for the subsequent measures.

Secondly, we observe a periodic pattern corresponding to the displacement induced in the off-axis. In particular, it is possible to note that from measure 1 to measure 7 the off-axis x and off-axis y both change in opposite directions (the first increase whereas the second decrease) when a displacement along off-axis x is applied. On the other hand, when a displacement along off-axis y is applied, from measure 7 to measure 13 the pattern changes and the both of them tend to increase or decrease simultaneously. During this phase the tilt shows a behaviour which is not constant. Moreover, in the measurement 13 where all the values should correspond to the first measure the tilt along x is almost doubled. The air gap tends to remain almost constant during this phase with limited variation in correspondence of the measurement 3 and 9. As far as the other measurements is concerned (13-16), the off-axis moves slightly with respect to the measurement 1 whereas the tilt along x and y increase or decrease in correspondence to manually rotations of the goniometer. During this phase the air gap shows evident variation in measurement 13, 14 (decrease) and 15 (increase).

Thirdly, the predicted off-axis directions are apparently different from the one induced but actually they predict correctly since the receivers are rotated of 45° during the measurement phase.

Table 4.6 shows the predicted values and the linearity error computed for each measurement with the least square fitting curve. We can observe that the measurements start with a linearity error which is 0.21%FS and oscillates as the displacements are induced. We also observe that when negative displacement of off-axis y are induced the linearity error improves. The minimum of this performance value is (approximately 0.5° of error) is achieved in correspondence of the measurement 11, when an off-axis y displacement of -0.4 mm is induced. Indeed, the anomaly values are very close to the ideal one with the exception of off-axis y which is predicted 0.17 mm. The higher linearity error are achieved in correspondence of the measurement 14 and 15 (approximately 28° of error).

Table 4.6: *Predicted values with the RF model and the linearity error for each measurement.*

Measurement	Air Gap[mm]	Off-Axis X[mm]	Off-Axis Y[mm]	Tilt X[°]	Tilt Y[°]	Linearity Error [%]
meas #1	0.74	0.21	0.21	-0.13	0.10	0.211
meas #2	0.76	0.02	0.51	-0.05	0.12	0.245
meas #3	0.79	-0.11	0.61	0.02	0.23	0.346
meas #4	0.74	0.23	0.25	-0.14	0.11	0.233
meas #5	0.75	0.36	0.06	-0.19	0.10	0.371
meas #6	0.72	0.83	-0.25	-0.12	0.12	0.591
meas #7	0.74	0.19	0.23	-0.13	0.10	0.223
meas #8	0.74	0.57	0.45	-0.23	0.22	0.409
meas #9	0.80	0.64	0.38	-0.33	0.23	0.553
meas #10	0.73	0.20	0.23	-0.13	0.10	0.223
meas #11	0.74	0.09	0.17	0.00	0.08	0.134
meas #12	0.77	-0.25	-0.05	0.18	-0.01	0.182
meas #13	0.67	0.26	0.23	-0.30	0.06	0.452
meas #14	0.67	0.35	0.29	-0.58	0.15	0.775
meas #15	0.94	0.21	0.18	0.58	0.29	0.782
meas #16	0.76	0.30	0.17	0.28	0.04	0.478

Finally, it is possible to observe that for each induced displacement the amplitude is not the same as those expected. Table 4.7 shows the module of the vectors depicted in Fig. 4.10. We can see the increasing or decreasing trend as the target is subject to off axis misalignment. The same happens for the tilt where it starts to have a significant change w.r.t. the previous trend. It is interesting to observe that the difference between measure 13 and measure 12 is of 0.5° meaning that the displacement w.r.t. the previous measurement is aligned with the expectations. We have to note here that for the computation of the angles we have used the usual eucledian distance but actually this is an approximation that holds for small angles. In general, one has to adopt computations such as law of cosine on a sphere.

However, although the predictions are not always aligned with the expected values the direction of the displacement is preserved. Indeed, Fig. 4.10 shows the direction of the off-axis and of the tilt as the variations are applied.

Measure	Predicted module of Off-Axis [mm]	Expected module of Off-Axis [mm]	Predicted module of Tilt [°]	Expected module of Tilt [°]
meas #1	-	-	-	-
meas #2	0.358	0.4	0.091	0
meas #3	0.516	0.8	0.198	0
meas #4	0.039	0	0.014	0
meas #5	0.203	0.4	0.059	0
meas #6	0.761	0.8	0.022	0
meas #7	0.034	0	0.002	0
meas #8	0.432	0.4	0.158	0
meas #9	0.463	0.8	0.237	0
meas #10	0.028	0	0.001	0
meas #11	0.134	0.4	0.137	0
meas #12	0.534	0.8	0.329	0
meas #13	0.053	0	0.168	0.5
meas #14	0.156	0	0.446	0.5
meas #15	0.030	0	0.736	$\sqrt{2}$*0.5
meas #16	0.089	0	0.419	0.5

Table 4.7: *Module of Off-Axis Misalignment and Tilt Misalignment with Reference to Measure 1*

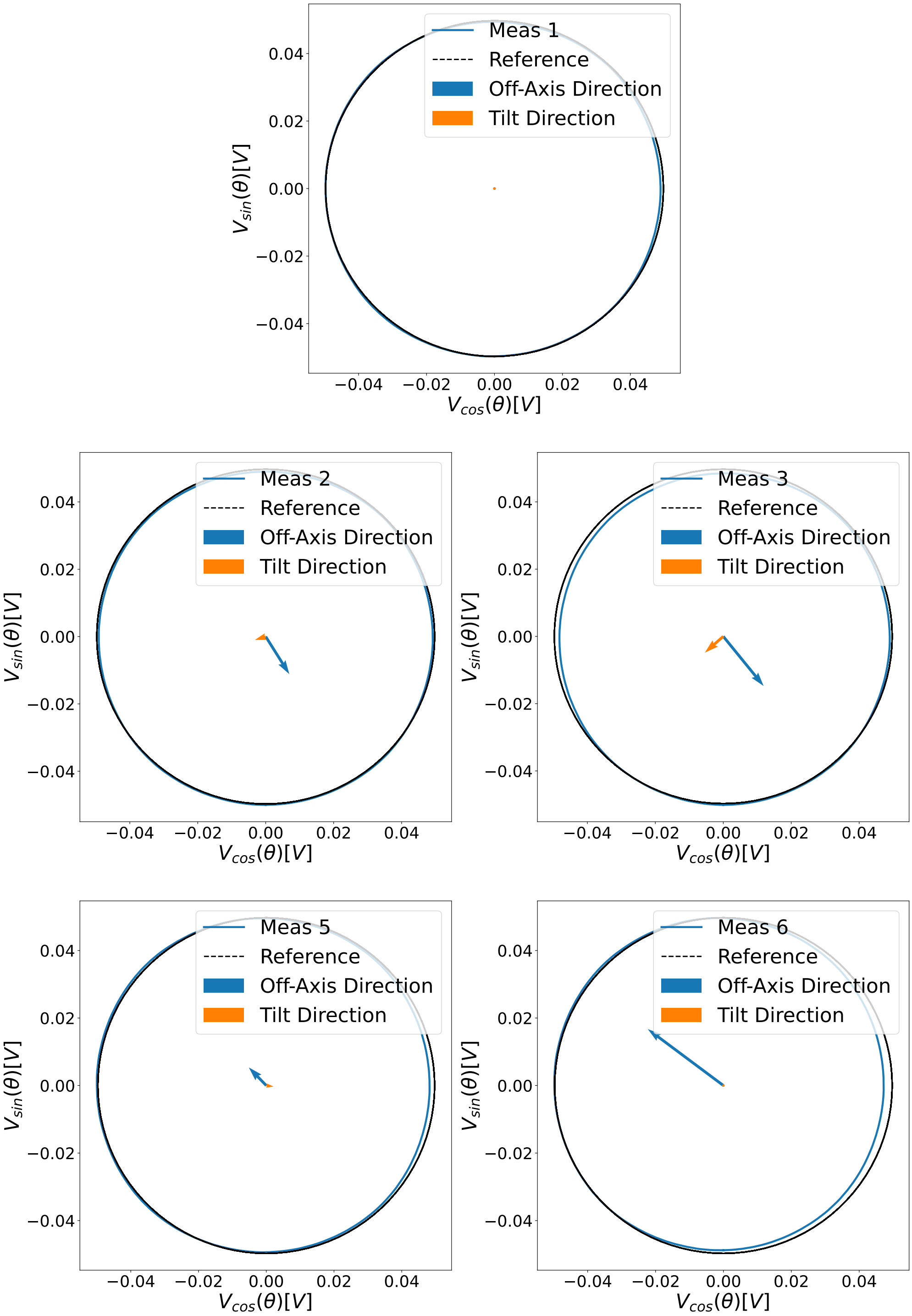
Meas 1
Reference
Off-Axis Direction
Tilt Direction
Meas 2
Meas 3
Meas 5
Meas 6
0.04
0.02
0.00
−0.02
−0.04
$V_{sin}(\theta)[V]$
$V_{cos}(\theta)[V]$

Figure 4.10

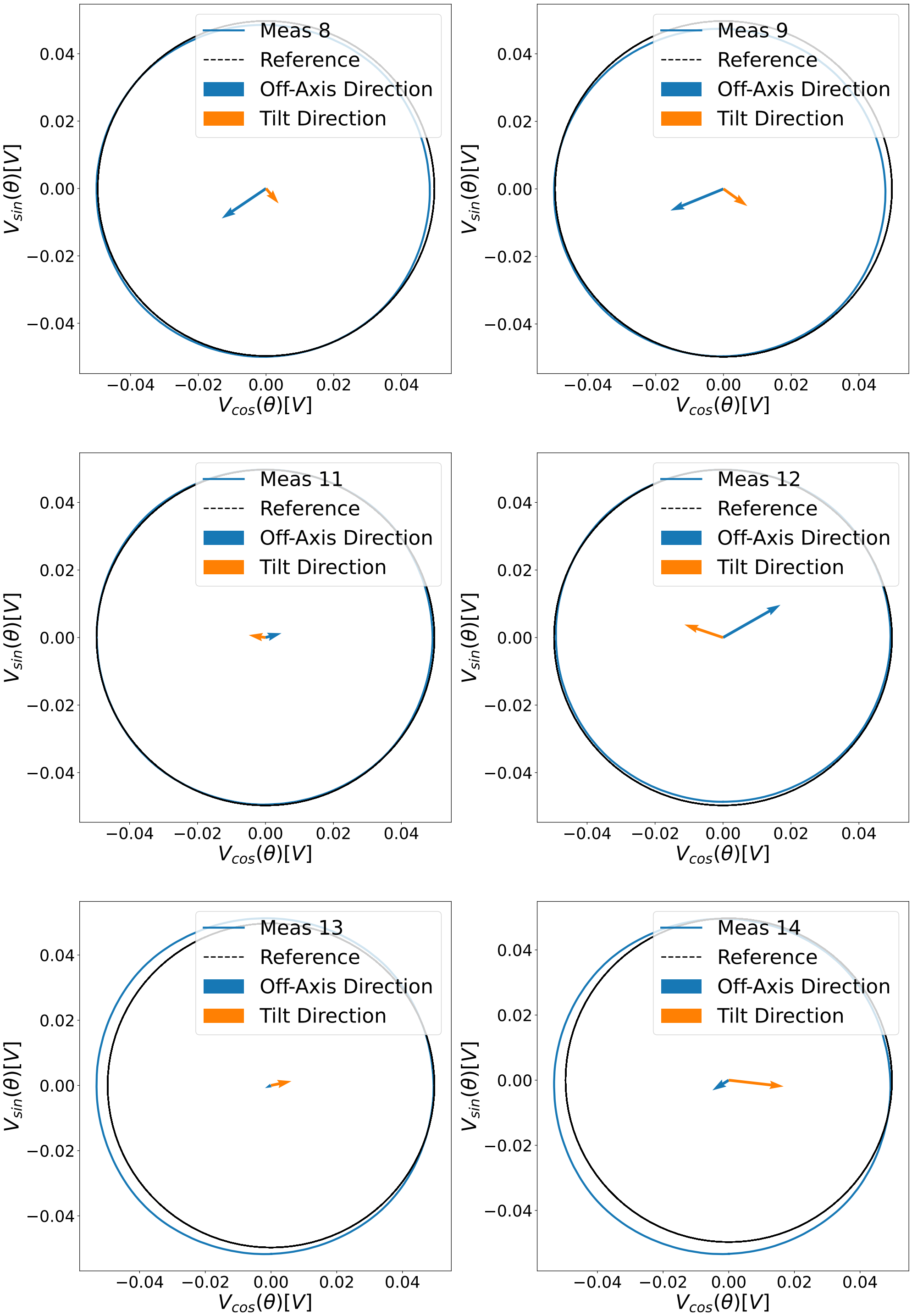
Meas 8
Reference
Off-Axis Direction
Tilt Direction
Meas 9
Reference
Off-Axis Direction
Tilt Direction
Meas 11
Reference
Off-Axis Direction
Tilt Direction
Meas 12
Reference
Off-Axis Direction
Tilt Direction
Meas 13
Reference
Off-Axis Direction
Tilt Direction
Meas 14
Reference
Off-Axis Direction
Tilt Direction
$V_{sin}(\theta)[V]$
0.04
0.02
0.00
−0.02
−0.04
$V_{cos}(\theta)[V]$
−0.04
−0.02
0.00
0.02
0.04

Figure 4.10

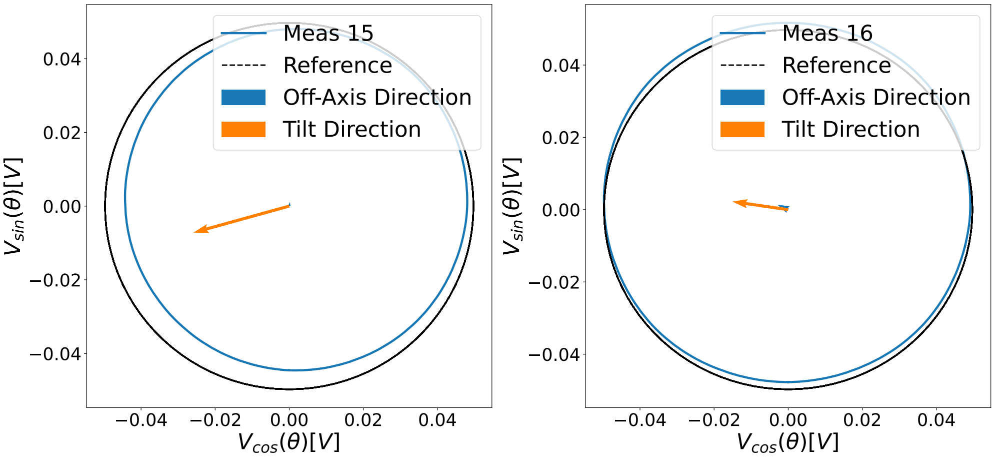

Figure 4.10: *The vectors of off-axis and tilt depicted in the 2D plane for each measurement w.r.t. the first measurement.*

CHAPTER 5

Conclusions

In conclusion, this research has presented innovative methods for investigating non-idealities on inductive position sensors using a numerical method casted in the Discrete Geometric Approach (DGA). The sensors, which operate based on eddy currents generated on a metallic moving object, have been studied from various aspects.

Firstly, a simulation tool based on the boundary integral method for the solution of MQS problems was provided to predict the performance of the sensor in terms of linearity error. The results validated the methodology, showing that measured linearity errors match simulated values.

Secondly, to overcome the limitation of the fully populated stiffness matrix, a method was described to compute the mutual coupling part of the system with two conductors on the fly. This allows for solving problems with a higher number of unknowns. The Gauss–Seidel (GS) iterative techniques and the fast multipole method (FMM) were applied to speed up the solution of the system and take into account the mutual effects between the conductors.

Thirdly, a novel methodology was proposed to optimize the design of a ratiometric rotary inductive position sensor (IPS) fabricated in printed circuit board (PCB) technology. The optimization aimed at reducing both the linearity error of the sensor and amplitude mismatch between the voltages on the two receiving (RX) coils. The optimized sensors exhibited a linearity error below 0.1% of the full scale (FS) without any signal calibration or post-processing manipulation.

Furthermore, it was shown that each target–receiver pair needs the adoption of a different reconstruction formula for the identification of the target position. A simulation and optimization method was applied to rectangular receiver coils on two rotary IPS realized with PCB technology. Measurements performed on these prototypes showed an increment of more than 57% in induced voltage amplitude compared to commonly used sinusoidal receivers, with linearity errors below 0.15%FS for the optimized prototype.

Moreover, a surrogate model for a rotary IPS was developed that mimics simulator behaviour and serves as a decision support tool. This model takes geometric parameters as input and outputs the maximum linearity error of the sensor, providing valuable insights to users in deciding which sensor to adopt for their purposes.

Finally, we developed a digital twin of a rotating shaft motor using a rotary IPS as a key component. For the first time, it was shown that this type of sensor has potential to provide information not only about position but also deviations from normal operating region. Supervised learning techniques such as Random Forest (RF) regressor were used to predict rotor shaft misalignments based on induced voltages on receivers. Experiments performed on a rotating motor in different operating conditions confirmed the effectiveness of this method in detecting misalignments and validating model accuracy.

As future development our aim is to publish in a journal the research on the misalignment identification and to continue the research in this topic. Indeed, other types of anomalies not considered in this work, such as wobble and skew, must be investigated in order to improve the performances of the model.

Bibliography

[1] H.-K. Ahn, O. Cheong, and C.-D. Park. Maximizing the overlap of two planar convex sets under rigid motions. In *Proceedings of the twenty-first annual symposium on Computational geometry*, pages 356–363, June 2005.

[2] L. Erhan al. Smart anomaly detection in sensor systems: A multi-perspective review. *Information Fusion*, 67:64–79, March 2021.

[3] L. Erhan al. Smart anomaly detection in sensor systems: A multi-perspective review. *Information Fusion*, 67:64–79, March 2021.

[4] R. Albanese and G. Rubinacci. Integral formulation for 3d eddy-current computation using edge elements. *IEE Proceedings A*, 135(7):457–462, 1988.

[5] P. Alotto, R. Specogna, and F. Trevisan. A θ-method for eddy currents in time-domain with a discrete geometric approach. *IEEE Trans. Magn.*, 42(4):779–782, April 2006.

[6] Piergiorgio Alotto and I Perugia. Matrix properties of a vector potential cell method for magnetostatics. *IEEE Transactions on magnetics*, 40(2):1045–1048, 2004.

[7] L. Ambrosio, N. Gigli, and G. Savaré. *Gradient flows: in metric spaces and in the space of probability measures*. Birkhäuser, Boston, 2005.

[8] Yali Amit and Donald Geman. Shape quantization and recognition with randomized trees. *Neural computation*, 9(7):1545–1588, 1997.

[9] Oxford Analytica. Sensors as drivers of industry 4.0–a study on germany, switzerland and austria, 2019.

[10] K. Ara. A differential transformer with temperature-and excitation-independent output. *IEEE Trans. Instrum. Meas*, 21(3):249–255, 1972.

[11] I. Bakir, M. Yildirim, and E. Ursavas. An integrated optimization framework for multi-component predictive analytics in wind farm operations & maintenance. *Renewable and Sustainable Energy Reviews*, 138, March 2021.

[12] Constantine A Balanis. *Antenna theory: analysis and design*. John wiley & sons, 2016.

[13] P. Bauer, P. D. Dueben, T. Hoefler, T. Quintino, T. C. Schulthess, and N. P. Wedi. The digital revolution of earth-system science. *Nat Comput Sci*, 1:2, February 2021.

[14] L. K. Baxter. *Capacitive sensors: design and applications*. Design and Applications, 1997.

[15] M. D. Berg, O. Devillers, M. V. Kreveld, O. Schwarzkopf, and M. Teillaud. Computing the maximum overlap of two convex polygons under translations. *Theory of Computing Systems*, pages 613–628.

[16] G. Berkovic and E. Shafir. Optical methods for distance and displacement measurements. *Adv. Opt. Photonics*, 4(4):441–471, 2012.

[17] P. Bettini, M. Passarotto, and R. Specogna. A volume integral formulation for solving eddy current problems on polyhedral meshes. *IEEE Trans. Magn.,vol.*, 53:5, June 2017.

[18] P. Bettini and R. Specogna. A bounary integral method for computing eddy currents in thin conductors of arbitrary topology. *IEEE Trans. Magn.*, 51(3):1–4, 2015.

[19] P. Bettini and R. Specogna. A boundary integral method for computing eddy currents in thin conductors of arbitrary topology. *IEEE Transactions on Magnetics*, 51:3, March 2015.

[20] O. Bíró and M. P. Gyimesi. Finite element implementation of the iterative scalar potential method for the computation of eddy currents. *IEEE Transactions on Magnetics*, 57(6):1–4, 2021.

[21] Christopher M Bishop and Nasser M Nasrabadi. *Pattern recognition and machine learning*, volume 4. Springer, 2006.

[22] Jerome Bonelle, Daniele A Di Pietro, and Alexandre Ern. Low-order reconstruction operators on polyhedral meshes: application to compatible discrete operator schemes. *Computer Aided Geometric Design*, 35:27–41, 2015.

[23] A. Bossavit. How weak is the weak solution in finite element methods? *IEEE Trans. Magn.*, 34(5):2429–2432, 1998.

[24] G. Brasseur. A robust capacitive angular position sensor. *IEEE Instrum. Meas. Technol. Conf*, 2:1081–1086, 1996.

[25] Leo Breiman. Random forests. *Machine learning*, 45:5–32, 2001.

[26] Leo Breiman. Statistical modeling: The two cultures (with comments and a rejoinder by the author). *Statistical science*, 16(3):199–231, 2001.

[27] Axel Buecker, Yana Ageeva, Veronique Blanchard, Jeremy Bloom, Mehmet F Candas, Joao Chaves, Guang Feng, Abhishek Raman, Hans Schlenker, et al. *Optimization and Decision Support Design Guide: Using IBM ILOG Optimization Decision Manager*. IBM Redbooks, 2012.

[28] S. Cabello, M. D. Berg, P. Giannopoulos, C. Knauer, R. V. Oostrum, and R. C. Veltkamp. Maximizing the area of overlap of two unions of disks under rigid motion. 24, 2009.

[29] V. Chandola, A. Banerjee, and V. Kumar. Anomaly detection: A survey. *ACM Comput. Surv.*, 41(3):1–58, July 2009.

[30] C Chen and D Cheng. Optimum element lengths for yagi-uda arrays. *IEEE Transactions on Antennas and Propagation*, 23(1):8–15, 1975.

[31] D Cheng and C Chen. Optimum element spacings for yagi-uda arrays. *IEEE Transactions on Antennas and Propagation*, 21(5):615–623, 1973.

[32] A. Choudhary, D. Goyal, S. L. Shimi, and A. Akula. Condition monitoring and fault diagnosis of induction motors: A review. *Arch Computat Methods Eng*, 26(4):1221–1238, September 2019.

[33] Markus Clemens and Thomas Weiland. Discrete electromagnetism with the finite integration technique. *Progress In Electromagnetics Research*, 32(32):65–87, 2001.

[34] Lorenzo Codecasa, Ruben Specogna, and Francesco Trevisan. A new set of basis functions for the discrete geometric approach. *Journal of Computational Physics*, 229(19):7401–7410, 2010.

[35] A. Danisi. Ironless inductive position sensor for harsh magnetic environments. 2013.

[36] C. Datlinger and M. Hirz. Benchmark of rotor position sensor technologies for application in automotive electric drive trains. *Electronics*, 9:7, 2020.

[37] William de Paula Ferreira, Fabiano Armellini, and Luis Antonio De Santa-Eulalia. Simulation in industry 4.0: A state-of-the-art review. *Computers & Industrial Engineering*, 149:106868, 2020.

[38] Paweł Dłotko and Ruben Specogna. Cohomology in 3d magneto-quasistatics modeling. *Communications in Computational Physics*, 14(1):48–76, 2013.

[39] Paweł Dłotko and Ruben Specogna. Lazy cohomology generators: A breakthrough in (co) homology computations for cem. *IEEE transactions on magnetics*, 50(2):577–580, 2014.

[40] Jozef Dodziuk. Finite-difference approach to the hodge theory of harmonic forms. *American Journal of Mathematics*, 98(1):79–104, 1976.

[41] Herbert Edelsbrunner and John L Harer. *Computational topology: an introduction*. American Mathematical Society, 2022.

[42] M. Fabbri. Magnetic flux density and vector potential of uniform poly- hedral sources. *IEEE Trans. Magn.*, 44(1):32–36, January 2008.

[43] Elena Ferretti. The cell method: An overview on the main features. *Curved and Layered Structures*, 2(1), 2015.

[44] J. Fraden. *Handbook of Modern Sensors: Physics, Designs, and Applications*. Springerca, New York, NY, 2010.

[45] M. Gasulla, X. Li, G. Meijer, L. van der Ham, and J. W. Spronck. A contactless capacitive angular-position sensor. *IEEE Sensors J.*, 2:880–884, 2002.

[46] Q. Gentjan, M. Passarotto, and R. Specogna. Sensor coil optimization. 2019, 2019.

[47] B. George, Z. Tan, and S. Nihtianov. Advances in capacitive, eddy current, and magnetic displacement sensors and corresponding interfaces. *IEEE Trans. Ind. Electron*, 64(12):9595–9607, 2017.

[48] Christophe Geuzaine and Jean-François Remacle. Gmsh: A 3-d finite element mesh generator with built-in pre-and post-processing facilities. *International journal for numerical methods in engineering*, 79(11):1309–1331, 2009.

[49] J. Golby. *Advances in inductive position sensor technology*. Sensor Review, 2010.

[50] J. N. Golby. *Advances in inductive position sensor technology*. Sensor Review, 2010.

[51] Marvin J Greenberg. *Algebraic topology: a first course*. CRC Press, 2018.

[52] M. Grieves. *Digital twin: Manufacturing excellence through virtual factory replication*. White paper [Online], 2014.

[53] Paul Wolfgang Gross and P Robert Kotiuga. *Electromagnetic theory and computation: a topological approach*, volume 48. Cambridge University Press, 2004.

[54] Lei Gu. A comparison of polynomial based regression models in vehicle safety analysis. In *International Design Engineering Technical Conferences and Computers and Information in Engineering Conference*, volume 80227, pages 509–514. American Society of Mechanical Engineers, 2001.

[55] Houssem Haddar, Ralf Hiptmair, Peter Monk, Rodolfo Rodríguez, and Ralf Hiptmair. Maxwell's equations: Continuous and discrete. *Computational Electromagnetism: Cetraro, Italy 2014*, pages 1–58, 2015.

[56] Ralf Hiptmair. Finite elements in computational electromagnetism. *Acta Numerica*, 11:237–339, 2002.

[57] B. Hou, Z. Tian, C. Li, Q. Wei, B. Zhou, and R. Zhang. A capacitive rotary encoder with a novel sensitive electrode. *2017 IEEE SENSORS*, pages 1–3, 2017.

[58] A. Hoxha, M. Passarotto, G. Qama, and R. Specogna. Design optimization of pcb-based rotary-inductive position sensors. *Sensors*, 22:13, June 2022.

[59] A. Hoxha, M. Passarotto, and R. Specogna. *Fast computation of eddy currents for multiple conductors*. IEEE Trans. Magn, 2022.

[60] A. Hoxha and R. Specogna. Study and design of ratiometric inductive position sensors using area-of- overlap functions. *IEEE Sensors Journal*, 22(23):22487–22494, December 2022.

[61] P. Hu, D. Chang, J. Tan, R. Yang, H. Yang, and H. Fu. Displacement measuring grating interferometer: a review. *Frontiers of Information Technology & Electronic Engineering*, 20(5):631–654, 2019.

[62] M. Kamon, M. J. Tsuk, and J. K. White. Fasthenry: a multipole-accelerated 3-d inductance extraction program. *IEEE Trans. Microw. Theory Techn.*, 42(9):1750–1758, 1994.

[63] H Leurent and ED Boer. Fourth industrial revolution beacons of technology and innovation in manufacturing. In *World Econ. Forum*, 2019.

[64] Z. Li, C. Zhang, S. Shi, X. Meng, and B. Wang. Design and parameter optimization of contactless vertical inductive angle sensor. *Vacuum*, 169, November 2019.

[65] Francesco Longo, Letizia Nicoletti, and Antonio Padovano. Smart operators in industry 4.0: A human-centered approach to enhance operators' capabilities and competencies within the new smart factory context. *Computers & industrial engineering*, 113:144–159, 2017.

[66] Salvatore T March and Gerald F Smith. Design and natural science research on information technology. *Decision support systems*, 15(4):251–266, 1995.

[67] G. S. Maruthi and V. Hegde. Mathematical analysis of unbalanced magnetic pull and detection of mixed air gap eccentricity in induction motor by vibration analysis using mems accelerometer. In *2013 IEEE 1st International Conference on Condition Assessment Techniques in Electrical Systems (CATCON*, pages 207–212, December 2013.

[68] A. Masi, A. Danisi, R. Losito, M. Martino, and G. Spiezia. Study of magnetic interference on an lvdt: Fem modeling and experimental measurements. *J. Sens*, 2011, 2011.

[69] F. McMullin, J. V. Byrne, and A. Murray. *Position and speed sensors*. Google Patents, 1988.

[70] Jeff Morgan, Mark Halton, Yuansong Qiao, and John G Breslin. Industry 4.0 smart reconfigurable manufacturing machines. *Journal of Manufacturing Systems*, 59:481–506, 2021.

[71] D. M. Mount, R. Silverman, and A. Y. Wu. On the area of overlap of translated polygons. *Computer Vision and Image Understanding*, 64:1, July 1996.

[72] Patrick Mullen, Pooran Memari, Fernando de Goes, and Mathieu Desbrun. Hot: Hodge-optimized triangulations. In *ACM SIGGRAPH 2011 papers*, pages 1–12. 2011.

[73] J. Nocedal and S. Wright. *Numerical optimization*. Springer, New York, 2006.

[74] D. S. Nyce. *Position sensors*. John Wiley & Sons, Hoboken, New Jersey, 2016.

[75] D. S. Nyce. *Position Sensors*. John Wiley & Sons, Incorporated, 2016.

[76] F. Paredes, C. Herrojo, and F. Martín. Position sensors for industrial applications based on electromagnetic encoders. *Sensors*, 21:8, 2021.

[77] M. Passarotto, G. Qama, and R. Specogna. *A Fast and Efficient Simulation Method for Inductive Position Sensors Design*. IEEE SENSORS, 2019.

[78] M. Passarotto, G. Qama, and R. Specogna. A fast and efficient simulation method for inductive position sensors design. *in Proc. IEEE SENSORS*, 2019:1–4, 2019.

[79] M. Passarotto, G. Qama, and R. Specogna. A fast and efficient simulation method for inductive position sensors design. *in*, 2019, October 2019.

[80] M. Passarotto, R. Specogna, and C. Geuzaine. Fast iterative schemes for the solution of eddy-current problems featuring multiple conductors by integral formulations. *IEEE Trans. Magn.*, 56:3, March 2020.

[81] Mauro Passarotto, Silvano Pitassi, and Ruben Specogna. Foundations of volume integral methods for eddy current problems. *Computer Methods in Applied Mechanics and Engineering*, 392:114626, 2022.

[82] J. Passlick, S. Dreyer, D. Olivotti, L. Gr"utzner, D. Eilers, and M. H. Breitner. Predictive maintenance as an internet of things enabled business model: A taxonomy. *Electron Markets*, 31(1):67–87, March 2021.

[83] J. Qiu, Q. Wu, G. Ding, Y. Xu, and S. Feng. A survey of machine learning for big data processing. *EURASIP J. Adv*, 2016:1, May 2016.

[84] Francesca Rapetti and Alain Bossavit. Whitney forms of higher degree. *SIAM Journal on Numerical Analysis*, 47(3):2369–2386, 2009.

[85] Carl Edward Rasmussen, Christopher KI Williams, et al. *Gaussian processes for machine learning*, volume 1. Springer, 2006.

[86] B. P. Reddy, A. Murali, and G. Shaga. Low cost planar coil structure for inductive sensors to measure absolute angular position. In *2017 2nd International Conference on Frontiers of Sensors Technologies (ICFST) pp*. 14–18, April 2017.

[87] P. Regtien and E. Dertien. 3 - uncertainty aspects. In *Sensors for Mechatronics (Second Edition)*, pages 39–60. 2018.

[88] P. Ripka, J. Blažek, M. Mirzaei, P. Lipovskŷ, M. Šmelko, and K. Draganová. Inductive position and speed sensors. *Sensors*, 20:1, 2020.

[89] Luca Romeo, Jelena Loncarski, Marina Paolanti, Gianluca Bocchini, Adriano Mancini, and Emanuele Frontoni. Machine learning-based design support system for the prediction of heterogeneous machine parameters in industry 4.0. *Expert Systems with Applications*, 140:112869, 2020.

[90] Y. Saad. Iterative methods for sparse linear systems. *Society for Industrial and Applied Mathematics*, 2:157–193, 2003.

[91] R. V. Sabariego, J. Gyselinck, P. Dular, C. Geuzaine, and W. Legros. Fast multipole acceleration of the hybrid finite-element/boundary-element analysis of 3-d eddy-current problems. *IEEE Trans. Magn.*, 40(2):1278–1281, March 2004.

[92] Manuel Sanchez, Ernesto Exposito, and Jose Aguilar. Industry 4.0: survey from a system integration perspective. *International Journal of Computer Integrated Manufacturing*, 33(10-11):1017–1041, 2020.

[93] Joachim Schöberl. Netgen an advancing front 2d/3d-mesh generator based on abstract rules. *Computing and visualization in science*, 1(1):41–52, 1997.

[94] P. Shakya, A. K. Darpe, and M. S. Kulkarni. Bearing diagnosis using proximity probe and accelerometer. *Measurement*, 80:190–200, February 2016.

[95] IM Sobol′. On the systematic search in a hypercube. *SIAM Journal on Numerical Analysis*, 16(5):790–793, 1979.

[96] Dorota Stadnicka, Jarosław Sęp, Riccardo Amadio, Daniele Mazzei, Marios Tyrovolas, Chrysostomos Stylios, Anna Carreras-Coch, Juan Alfonso Merino, Tomasz Żabiński, and Joan Navarro. Industrial needs in the fields of artificial intelligence, internet of things and edge computing. *Sensors*, 22(12):4501, 2022.

[97] Thorsten Steinmetz, Stefan Kurz, and Markus Clemens. Domains of validity of quasistatic and quasistationary field approximations. *COMPEL-The international journal for computation and mathematics in electrical and electronic engineering*, 30(4):1237–1247, 2011.

[98] F. Tao, H. Zhang, A. Liu, and A. Y. C. Nee. Digital twin in industry: State-of-the-art. *IEEE Transactions on Industrial Informatics*, 15(4):2405–2415, April 2019.

[99] J. Tao, Y. Liu, and D. Yang. Bearing fault diagnosis based on deep belief network and multisensor information fusion. *Shock and Vibration*, 2016, September 2016.

[100] Enzo Tonti. Finite formulation of electromagnetic field. *IEEE Transactions on Magnetics*, 38(2):333–336, 2002.

[101] Enzo Tonti. *The mathematical structure of classical and relativistic physics*, volume 10. Springer, 2013.

[102] Enzo Tonti. Why starting from differential equations for computational physics? *Journal of Computational Physics*, 257:1260–1290, 2014.

[103] R. Torchio, V. Cirimele, P. Alotto, and F. Freschi. Modelling of road–embedded transmitting coils for wireless power transfer. *Computers & Electrical Engineering*, 88, 2020.

[104] E. VanDerHorn and S. Mahadevan. Digital twin: Generalization, characterization and implementation. *Decision Support Systems*, 145, June 2021.

[105] G Gary Wang and Songqing Shan. Review of metamodeling techniques in support of engineering design optimization. In *International Design Engineering Technical Conferences and Computers and Information in Engineering Conference*, volume 4255, pages 415–426, 2006.

[106] K. Wang and Z. Wu. Oversampling synchronous envelope detection for resolver-to-digital conversion. *IEEE Trans. Ind. Electron*, 67(6):4867–4876, 2019.

[107] J. G. Webster and H. Eren. *Measurement, Instrumentation, and Sensors Handbook: Spatial, Mechanical, Thermal, and Radiation Measurement, 2nd ed.* CRC press, Boca Raton, FL, USA, 2014.

[108] J. S. Wilson. *Sensor technology handbook*. Elsevier, 2004.

[109] L. Wright and S. Davidson. How to tell the difference between a model and a digital twin. *Advanced Modeling and Simulation in Engineering Sciences*, 7:1, March 2020.

[110] S.-T. Wu, J.-Y. Chen, and S.-H. Wu. A rotary encoder with an eccentrically mounted ring magnet. *IEEE Trans. Instrum. Meas*, 63(8):1907–1915, 2014.

[111] Z. Yang and Z. Ge. On paradigm of industrial big data analytics: From evolution to revolution. *IEEE Transactions on Industrial Informatics*, 18(12):8373–8388, December 2022.

[112] L. Ye, M. Yang, L. Xu, C. Guo, L. Li, and D. Wang. Optimization of inductive angle sensor using response surface methodology and finite element method. *Measurement*, 48:252–262, 2014.

[113] L. Ye, M. Yang, L. Xu, C. Guo, L. Li, and D. Wang. Optimization of inductive angle sensor using response surface methodology and finite element method. *Measurement*, 48, February 2014.

[114] L. Ye, M. Yang, L. Xu, X. Zhuang, Z. Dong, and S. Li. Nonlinearity analysis and parameters optimization for an inductive angle sensor. *Sensors*, 14(3):4111–4125, 2014.

[115] Nur Hanifa Mohd Zaidin, Muhammad Nurazri Md Diah, and Shahryar Sorooshian. Quality management in industry 4.0 era. *Journal of Management and Science*, 8(2):182–191, 2018.

[116] C. Zhang, Z. Li, J. Chen, F. Qiu, and S. Na. Design and research of a novel non-contact vertical inductive torque sensor. *Measurement*, 177, June 2021.

[117] Z. Zhang, Y. Dong, F. Ni, M. Jin, and H. Liu. A method for measurement of absolute angular position and application in a novel electromagnetic encoder system. *J. Sens*, 2015, 2015.

[118] Z. Zhang, F. Ni, Y. Dong, C. Guo, M. Jin, and H. Liu. A novel absolute magnetic rotary sensor. *IEEE Transactions on Industrial Electronics*, 62:7, July 2015.

[119] Z. Zhang, F. Ni, Y. Dong, M. Jin, and H. Liu. A novel absolute angular position sensor based on electromagnetism. *Sensors and Actuators A: Physical*, 194, May 2013.

[120] D. Zheng, S. Zhang, S. Wang, C. Hu, and X. Zhao. A capacitive rotary encoder based on quadrature modulation and demodulation. *IEEE Trans. Instrum. Meas*, 64(1):143–153, 2014.

[121] Ray Y Zhong, Xun Xu, Eberhard Klotz, and Stephen T Newman. Intelligent manufacturing in the context of industry 4.0: a review. *Engineering*, 3(5):616–630, 2017.

[122] Afra J Zomorodian. *Topology for computing*, volume 16. Cambridge university press, 2005.

[123] T. Zonta, C. A. da Costa, F. A. Zeiser, G. de Oliveira Ramos, R. Kunst, and R. da Rosa Righi. A predictive maintenance model for optimizing production schedule using deep neural networks. *Journal of Manufacturing Systems*, 62:450–462, January 2022.